DETERMINATION OF THE ELECTROCALORIC PROPERTIES OF THE FERROELECTRIC $(1-x)BaTiO_3$-$xBi(Li_{1/3}Ti_{2/3})O_3$ $(0 \leq x \leq 0.2)$ SYSTEM

A Thesis Submitted to
The Graduate School of Engineering and Science of
İzmir Institute of Technology
in Partial Fulfillment of the Requirements for the Degree of

MASTER OF SCIENCE

in Materials Science and Engineering

by
Tuğçe DEMİRTAY

December 2018
İZMİR

We approve the thesis of **Tuğçe DEMİRTAY**

Examining Committee Members:

_____
Dr. Umut ADEM
Department of Materials Science and Engineering, İzmir Institute of Technology

_____
Assoc. Prof. Dr. Çekdar Vakıf AHMETOĞLU
Department of Materials Science and Engineering, İzmir Institute of Technology

_____
Assoc. Prof. Dr. Ümit AKINCI
Department of Physics, Dokuz Eylül University

27 December 2018

_____
Dr. Umut ADEM
Supervisor, Department of Materials Science and Engineering, İzmir Institute of Technology

_____
Prof. Dr. Muhsin ÇİFTÇİOĞLU
Co-Supervisor, Department of Chemical Engineering, İzmir Institute of Technology

_____
Prof. Dr. Mustafa Muammer DEMİR
Head of the Department of Materials Science and Engineering

_____
Prof. Dr. Aysun SOFUOĞLU
Dean of the Graduate School of Engineering and Sciences

ACKNOWLEDGEMENTS

I would like to thank my thesis advisor Dr. Umut Adem for sharing his knowledge and experiences with me. He supported and guidanced me at every stage of the study and whenever I had a problem about my research he made me believe that I could solve the problems myself. Furthermore, I would like to thank to my co-advisor Prof. Dr. Muhsin Çiftçioğlu for his valuable information and support.

I would like to thank Turkish Scientific and Technological Research Council (TÜBİTAK) via the project with the number 315M241 and IZTECH for supporting me during this project.

An important part of this study is carried out at the ICREA Institute at Barcelona and I am very thankful to Dr. Aziz Genç for TEM measurements. I would like to thank Prof. Dr. Ender Suvacı for the strain measurements and his participation and comments for this study.

I would like to express my gratitude to the Işın Özçelik for XRD experiments. I would like to thank specialist of Material Research Center of IKCU for SEM analysis.

My deepest gratitude goes foremost to my dear parents Figen Dönertaş and Atilla Demirtay and my brother Orkun Demirtay and his precious wife Oya Demirtay who always feel behind me and think of my happiness and future in my all life. They made me keep going all the time and they believed I could and this study would not have been possible without them.

I would like to thank my dear friend Keriman Şanlı for providing motivation and valuable friendship during my study. I cannot forget to mention my lovely dog Tina who motivate and made me happy.

Last but not least, I would like to thank my dear friend Gürol İleri for his valuable support and understanding. Furthermore, I would also thank to Burak Bostancıoğlu, Ali Çakal and Birnur Kaya for their valuable friendship.

ABSTRACT

DETERMINATION OF THE ELECTROCALORIC PROPERTIES OF THE FERROELECTRIC (1-x)$BaTiO_3$-x$Bi(Li_{1/3}Ti_{2/3})O_3$ ($0 \leq x \leq 0.2$) SYSTEM

The aim of this study is to develop electrocaloric (EC) materials for alternative eco-friendly cooling technologies.

Considering the dielectric and piezoelectric properties of the (1-x)$BaTiO_3$-x$Bi(Li_{1/3}Ti_{2/3})O_3$ ($0 \leq x \leq 0.2$), this system was selected to study electrocaloric properties due to the presence of morphotropic phase boundary (MBP). The crystal structure of the samples that were synthesized by convential solid state reaction technique were determined by the X-Ray Diffraction experiments. The electrical properties of the ceramics were characterized by temperature-dependent dielectric measurements and the phase transition temperatures of the samples were identified. Temperature-dependent electrical polarization curves were measured for all compositions and electrocaloric temperature change values were calculated with the help of Maxwell equations. Using the dielectric measurements, a phase diagram was obtained. Strain-electric field measurements were done to complement dielectric and polarization measurements.

A new antiferroelectric phase was discovered at high temperatures in the samples. As $Bi(Li_{1/3}Ti_{2/3})O_3$ content is increased, phase transition from the ferroelectric to antiferroelectric phase decreases. Since in the antiferroelectric phase the net polarization is very small, a large polarization change therefore large electrocaloric temperature change is obtained. Highest electrocaloric temperature change (ΔT=0.66 K under 22 kV/cm) is obtained for x=0.03 sample.

ÖZET

FERROELEKTRİK $(1-x)BaTiO_3$-$xBi(Li_{1/3}Ti_{2/3})O_3$ $(0\leq x\leq 0.2)$ SİSTEMİNİN ELEKTROKALORİK ÖZELLİKLERİNİN BELİRLENMESİ

Bu çalışmanın amacı, alternatif çevre dostu soğutma teknolojileri için elektrokalorik (EC) malzemeler geliştirmektir.

$(1-x)BaTiO_3$-$xBi(Li_{1/3}Ti_{2/3})O_3$ $(0\leq x\leq 0.2)$ sisteminde, dielektrik ve piezoelektrik ölçümlere göre morfotropik faz sınırı bulunduğundan bu sistem elektrokalorik özellikleri çalışılmak için seçilmiştir. Geleneksel katı hal reaksiyon tekniği ile sentezlenen numunelerin kristal yapısı, X-Işını Kırınımı deneyleriyle belirlenmiştir. Seramiklerin elektriksel özellikleri sıcaklığa bağlı dielektrik ölçümleri ile karakterize edilmiştir ve örneklerin faz geçiş sıcaklıkları belirlenmiştir. Sıcaklığa bağlı elektriksel kutuplanma eğrileri ölçülmüş ve Maxwell denklemlerinin yardımıyla elektrokalorik sıcaklık değişimi değerleri hesaplanmıştır. Dielektrik ölçümler kullanılarak bir faz diyagramı elde edilmiştir. Dielektrik ve polarizasyon ölçümlerini tamamlamak amacıyla gerinim-elektrik alan ölçümleri yapılmıştır.

Örneklerde yüksek sıcaklıklarda yeni bir antiferroelektrik faz keşfedilmiştir. Artan $Bi(Li_{1/3}Ti_{2/3})O_3$ oranıyla ferroelektrik fazdan antiferroelektrik faza geçiş sıcaklığı düşmektedir. Antiferroelektrik fazdaki net polarizasyonun çok küçük olması nedeniyle ferroelektrik antiferroelektrik geçiş sıcaklığında yüksek bir polarizasyon değişimi dolayısıyla yüksek elektrokalorik sıcaklık değişimi elde edilmiştir. En yüksek elektrokalorik sıcaklık değişimi (22 kv/cm altında $\Delta T=0.66$ K) $x=0.03$ örneğinde elde edilmiştir.

TABLE OF CONTENTS

LIST OF FIGURES

Figure **Page**

LIST OF TABLES

Table **Page**

CHAPTER 1

INTRODUCTION

The alternative cooling technologies is needed to prevent the global warming and climate changes as a result of greenhouse gas effect triggered by halocarbon gases emitted by existing cooling technologies. One of the alternative technologies is based on the electrocaloric effect that employs ferroelectric materials.

In order to understand the electrocaloric effect, the material classes and their properties, an introduction is given in this chapter.

1.1. Ferroelectricity

The electrocaloric effect is observed in ferroelectric, relaxor ferroelectric and antiferroelectric materials. In this subsection, these materials and material properties will be explained.

1.1.1. Ferroelectric Materials

Ferroelectrics are type of pyroelectric crystal classes defined as polar insulator materials. The lack of center of symmetry brings the spontaneous polarization property. Therefore, ferroelectric materials exhibit polar symmetry having a spontaneous polarization where the direction of polarization could be switched by application of electric field. [1]

These properties classify the ferroelectric materials under the dielectric material class as shown in Venn diagram in Figure 1.1 with characteristic features of the materials.

Switchable polarization direction property of ferroelectrics yields hysteresis loop behavior as shown in Figure 1.2.

In the beginning (in the absence of electric field), the randomly oriented domains that minimize the electrostatic energy, are separated by domain walls. By applying external electric field, the domains are oriented in the direction of the electric field and grow at the expense of unfavorable ones and continue till to a single domain is formed

with the same direction with electric field. This corresponds to the saturation polarization (P_s) shown at point D in Figure 1.2. When the electric field is removed, the domain structure, in which polarization is in the same direction with the electric field, wishes to return to its original state. However, this require a re-formation of the domain walls, and a remanent polarization (P_r) value is kept in the material.

When the electric field direction is reversed, the same conditions are valid and negative saturation polarization and negative remanent polarization ($-P_r$) are achieved ,respectively.[2] E_c is term donating coercive field of the material that represents the minimum electric field that must be applied to depolarize the material, the hysteresis loop is characteristic for the materials.

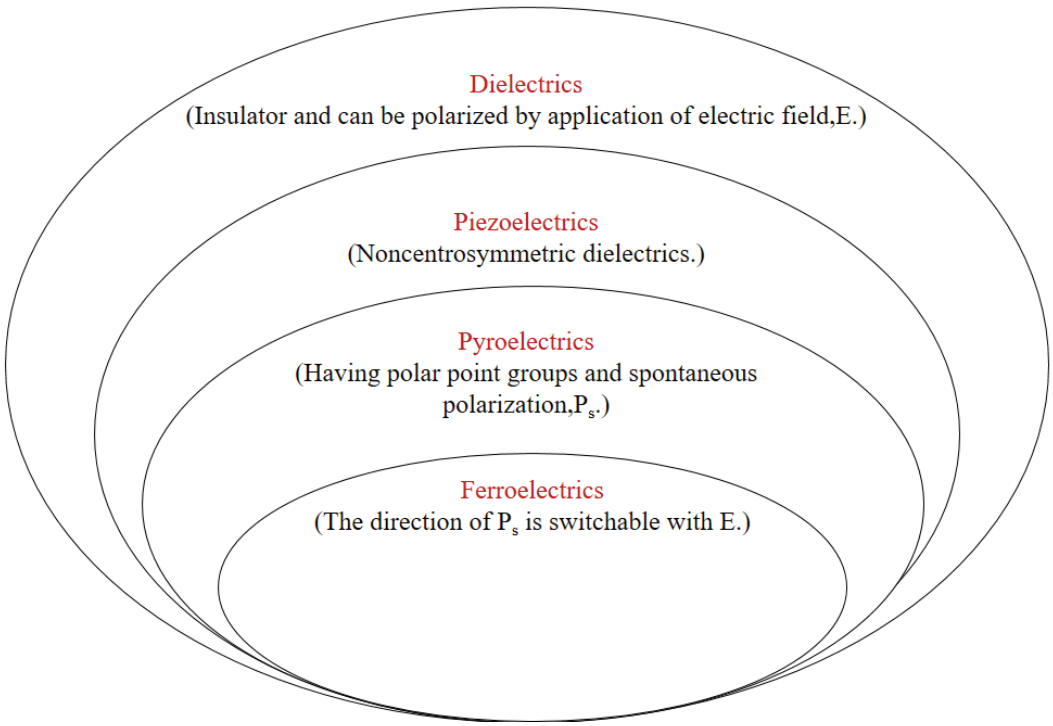

Figure 1.1. Venn diagram showing the relation between dielectrics, piezoelectrics, pyroelectrics and ferroelectrics.

Hysteresis behavior is preserved with narrowing of the loops as the temperature increases until the temperature called as the Curie temperature,T_c at which the material with ferroelectric property (low symmetry phase) have a phase transition to the non-polar phase named as paraelectric phase (high symmetry phase).[1,3]

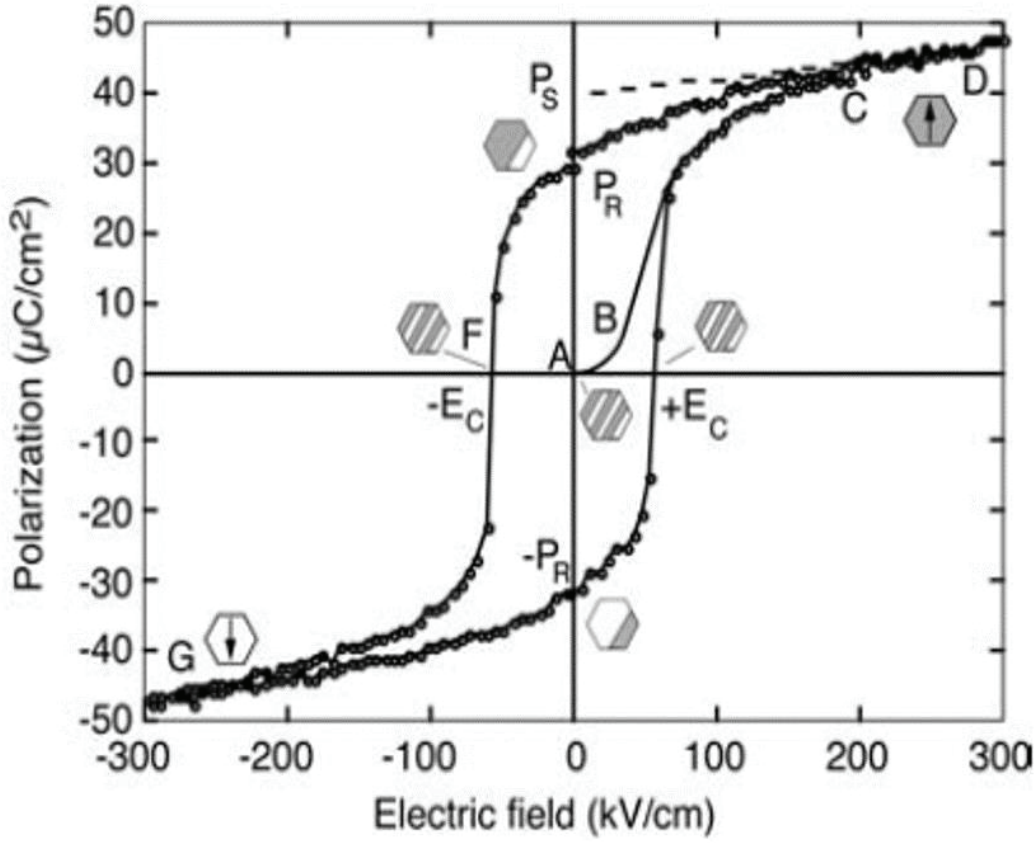

Figure 1.2. Hysteresis loop of a ferroelectric material.[4]

At the phase transition temperature (T_c), the ferroelectric materials have a peak in the dielectric constant. Therefore dielectric constant is very high. The temperature dependence of the dielectric constant is defined by Curie Weiss law[1] as given in Equation 1.1.

$$\varepsilon = \frac{C}{T - T_0} \tag{1.1}$$

T_0 is the Curie Weiss temperature and defined as the temperature at which the dielectric constant begins to be linear. C is the Curie Weiss constant.

Since the ferroelectric materials are also piezoelectric, a relative displacement is obtained in the unit cell by the applied electric field. This is referred to as a piezoelectric effect and leads to strain-electric field hysteresis with typical butterfly-shaped curve as shown in Figure 1.3.

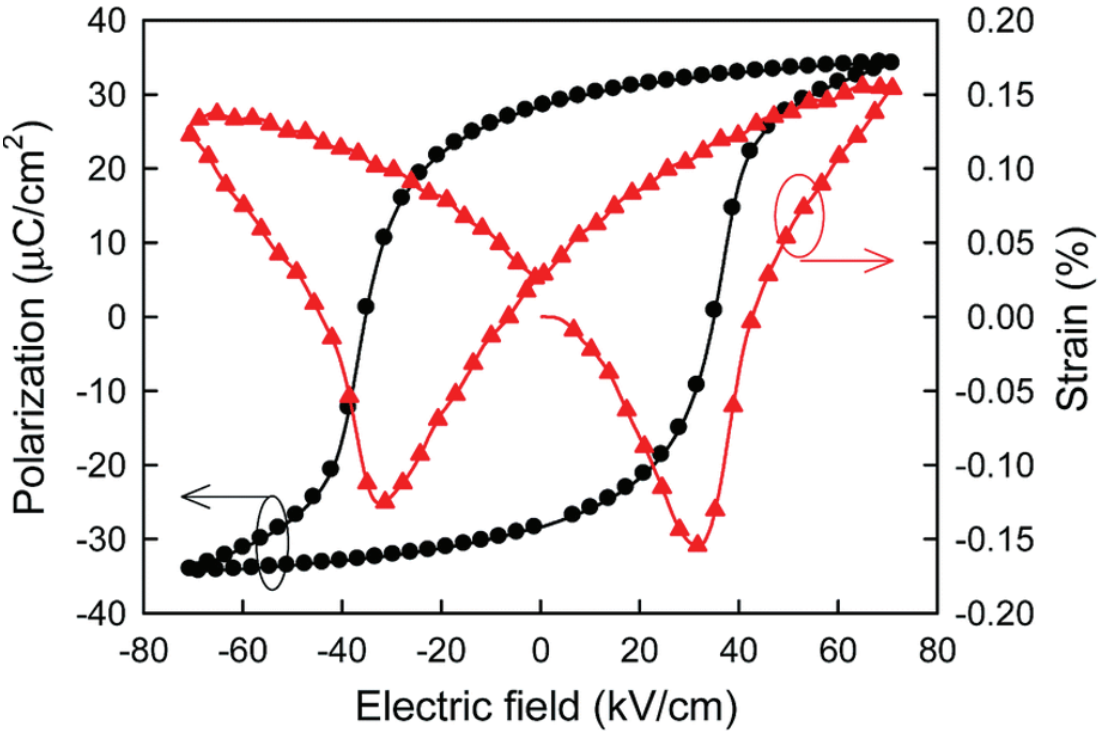

Figure 1.3. Strain-electric field hysteresis loop with butterfly shape in ferroelectrics.[5]

The strain of the crystal is zero in the absence of electric field. A displacement occurs in the unit cell under the applied electric field and a strain value is obtained under the formed stress or displacement. The maximum strain value is observed when the polarization of material is saturated. When the electric field is removed, the strain drops to the zero. If the electric field is applied in the opposite direction, same behavior occurs in the material and negative strain values are obtained. Thus, butterfly shaped strain electric field curve is formed.

Ferroelectric materials have perovskite type crystal structure with the chemical formula ABO_3. The perovskite structure is very important for ferroelectric materials offering the possibility to dope the material at both A and B sites. The dopant atoms affect the phase transition character and phase transition temperature of the ferroelectric materials and cause changes in the tolerance factor that describe the stability or distortion of the crystal structure. Thus doping brings different properties to the ferroelectrics. The Goldschmidt tolerance factor (t) formula is given in Equation 1.2[1] where r_A, r_B and r_O are the radii of A and B sites and the oxygen atom, respectively.

$$t = \frac{(r_A + r_o)}{\sqrt{2}(r_{B+} r_o)} \qquad (1.2)$$

The doping of the material either to the A or B sites causes distortion of the crystal structure. The distortion weakens the bond between the B site ion and the oxygen ion, which is the source of ferroelectricity. This affects the phase transition characteristics of ferroelectric materials and change it from the first order phase transition (FOPT) at which the materials have sharp permittivity maximum over a narrow temperature range, to the diffuse phase transition (DPT) where the materials have a broad dielectric permittivity maximum with no or little frequency dependence.

Further increase in the doping level changes the domain structure of the ferroelectric materials and causes the formation of nanodomains, such ferroelectrics are called as **relaxor ferroelectrics**. Relaxor ferroelectricity occurs due to compositional disorder induced by doping which provides more than one element in the doped site of the perovskite structure. This disorder does not include charge disorder due to charge neutrality rule however it leads to change in off-center ionic shifts.[3] The frequency dependence and the shift in dielectric maxima with respect to the frequency are the fingerprints of the dielectric behavior of the relaxor ferroelectrics.[6]

Relaxor ferroelectrics shows hysteresis behavior till T_m (the dielectric maxima). T_m shifts to higher temperature with increasing frequency and dielectric loss is broad and frequency-dependent. Relaxors can be divided into two subgroup as ergodic and nonergodic relaxors.[5] Figure 1.4 shows the schematic representation of domain structure in the ergodic and nonergodic relaxors.

Two different temperatures are defined for polar nanoregions (PNRs) (relaxor ferroelectrics). T_B is the Burns temperature which is the phase transition temperature from nonergodic relaxor to paraelectric phase as shown in Figure 1.4. T_F is the freezing temperature where the transition occurs between nonergodic relaxor to ergodic relaxor. Below the T_F, the nonergodic relaxors show ferroelectric hysteresis and this behavior is induced by application of the electric field and the dielectric behavior is nearly frequency independent at this temperature. When the material is cooled under the electric field, ferroelectric domains become visible. The domain pattern disappeares at T_F by removing the electric field and reheating the material.

Figure 1.5 (a)-(c) shows the comparison of normal and relaxor ferroelectrics. In summary, when ferroelectric and relaxor ferroelectrics are compared, ferroelectrics have macro-sized domains, whereas relaxors consists of nanodomains. The coercive field and remanent polarization values of the ferroelectric materials are much higher than the relaxors and the slim loop is observed in the relaxors (see in Figure 1.5 (a)). While the

ferroelectrics have a sharp phase transition around the Curie temperature (T_C), the relaxors display a broad dielectric maximum at T_m and the change in polarization with respect to the temperature is not sharp (Figure 1.5 (b)).

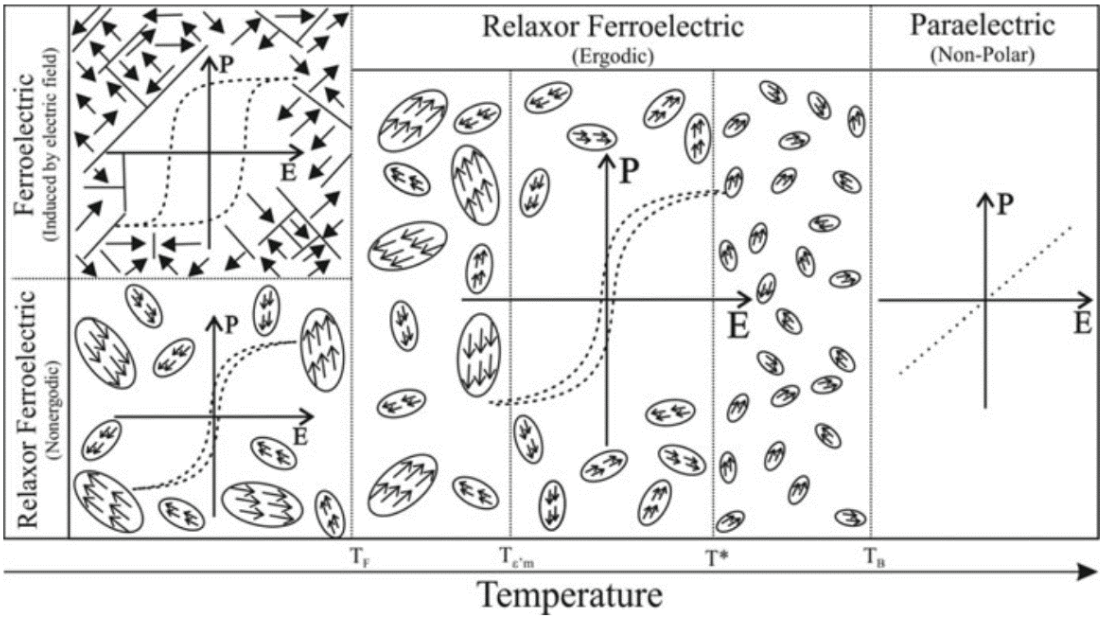

Figure 1.4. The polar nanodomains in different type of relaxor ferroelectrics.[7]

In terms of dielectric properties, ferroelectrics reach a dielectric maxima with a sharp transition in a narrow temperature range without frequency dependence. In relaxor ferroelectrics, frequency dependent dielectric behavior is observed over a wide temperature range and dielectric maxima shifts with frequency to higher temperatures. Relaxor ferroelectrics show a strong deviation from Curie-Weiss law while the ferroelectrics follow the Curie-Weiss law. Relaxors can be described by the modified Curie-Weiss law as given in Equation 1.3 where ε_m is the maximum dielectric constant observed in T_m temperature.

$$\frac{1}{\varepsilon} - \frac{1}{\varepsilon_m} = (T - T_m)^{\gamma} \tag{1.3}$$

Where the ɣ is the diffuseness coefficient and equals to 1 for normal ferroelectrics (undoped) and the increase in the doping level causes the ɣ value to approach 2 for relaxor ferroelectrics.

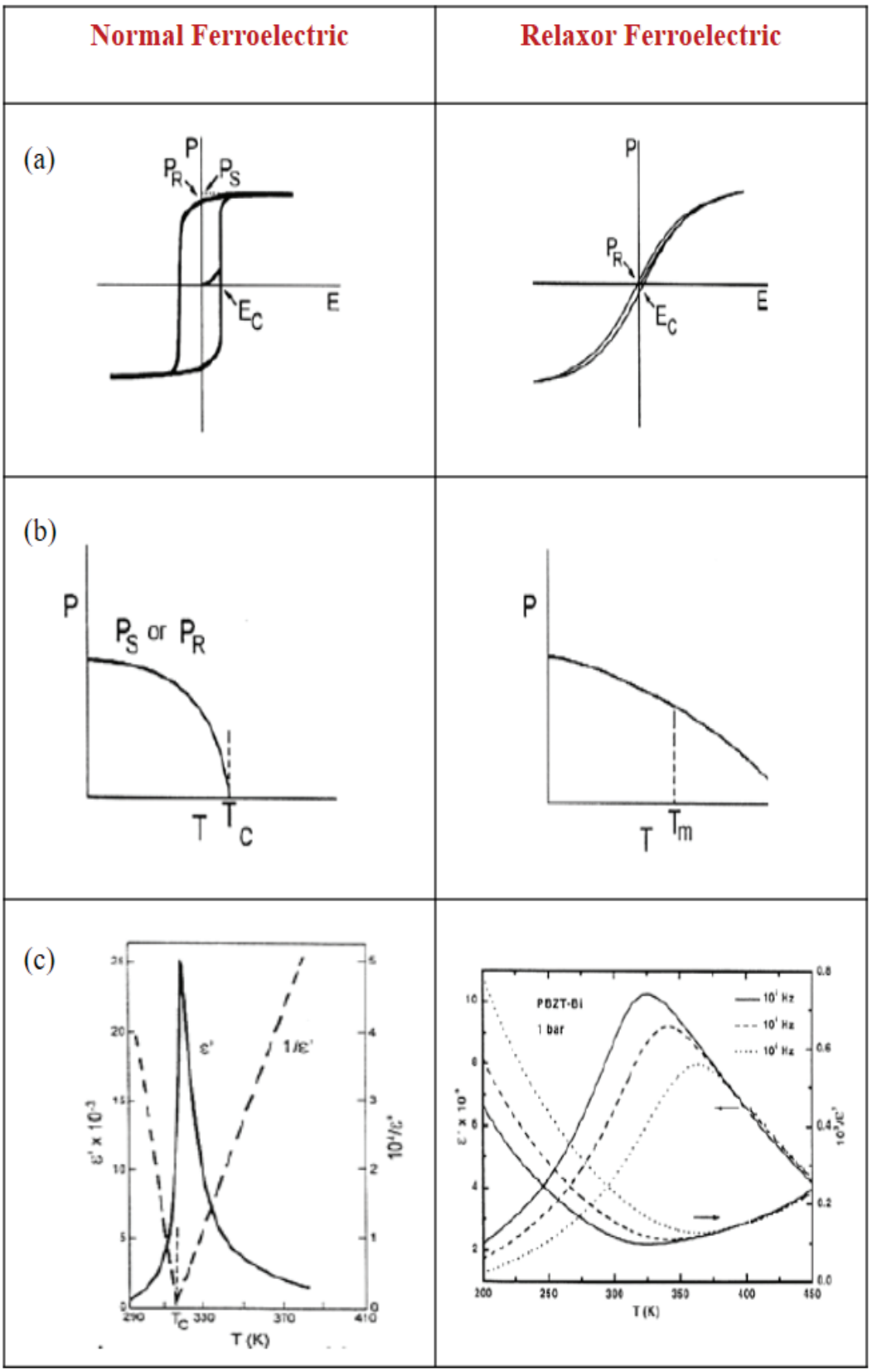

Figure 1.5. Comparison of (a) hyteresis curves (b) phase transition behavior (c) dielectric behavior of the normal ferroelectrics and relaxor ferroelectrics.[8]

1.1.2. Antiferroelectric Materials

Antiferroelectric materials have domain structures with antiparallel electrical dipole moments and application of electric field induces a ferroelectric phase by switching the polarization directions in parallel order.[9] This type of materials have a non-polar crystal symmetry and there must be a transition from the non-polar to polar symmetry with application of the electric field which means that in antiferroelectrics there is a competition between the polar and non-polar phases where the free energy difference is small. Figure 1.6 (a) shows this situation. The double hysteresis loop (as shown in Figure 1.6 (b)) in antiferroelectrics is the fingerprint of the induced phase transition.

Since the nonpolar and polar phases have different crystal symmetry, the transition between these two phases, that takes place with the help of applied electric field, provides a high strain value due to the large volume expansion.[10]

This type of materials also exhibit a dielectric anomaly at the structural phase transition temprature from the antiferroelectric to the paraelectric phase and antiferroelectric materials obey the Curie-Weiss law (Equation 1.1) above the transition temperature.

Polarization switching under electric field due to phase transition from antiferroelectric to the ferroelectric phase causes current switching and large current values. Figure 1.7 shows the switching current behavior of antiferroelectrics.

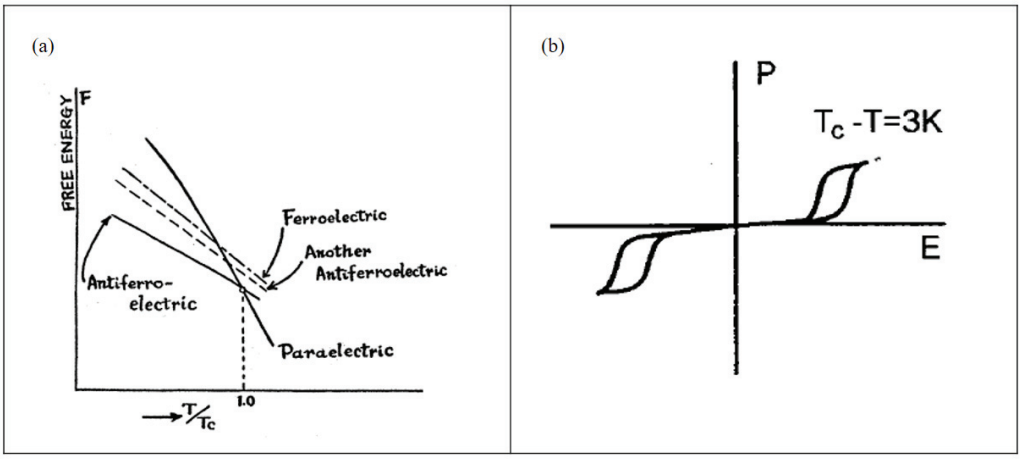

Figure 1.6. (a) The free energy curves of the antiferroelectric $PbZrO_3$ material. (b) Typical double hysteresis curve of $PbZrO_3$.[10]

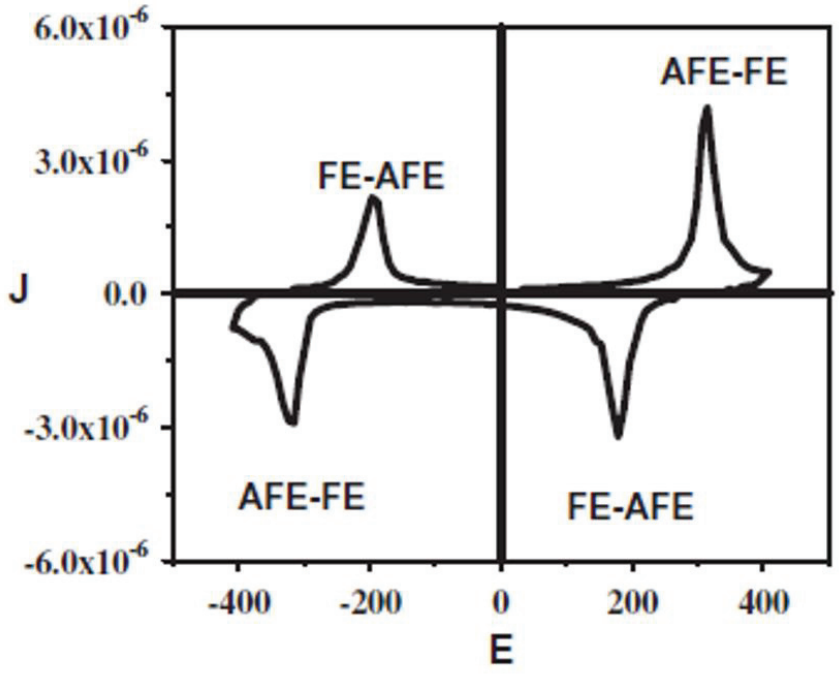

Figure 1.7. Typical current density-electric field curves of antiferroelectric materials.[11]

4 peaks and large current values in the J-E curve are clearly shown in Figure 1.7. When an electric field is applied to the antiferroelectric phase, antiparallel dipoles orient in the direction of electric field and become parallel. This causes large current (AFE-FE point in the Figure). Similarly, a large current is observed when the ferroelectric phase reaches the antiparallel dipole arrangement again (FE-AFE point in the Figure). These J-E curves can also be used to characterize the antiferroelectric behavior.

1.2. Electrocaloric Effect (ECE)

In this section, history of electrocaloric effect, its working principle, measurement methods and application areas will be discussed.

1.2.1. History of ECE

The discovery of the electrocaloric effect was achieved by Kobeko and Kurtschatov in 1930 with Rochelle salt. Since the values obtained with potassium dihydrogen phosphate in 1950 are also as small as Rochelle salt, the electrocaloric effect is not considered for utilization in alternative cooling technology until 2000s. In the

2000s, a large electrocaloric temperature change of 12 K was obtained by Mischenko et al. in the PZT thin film.[12] This giant value brings new excitement to the studies on electrocaloric effect. After that, many studies have been done. These studies will be explained in detail in sections 1.3 and 1.4.

1.2.2. Phenomenological and Thermodynamical Description of ECE

The electrocaloric effect (ECE) is observed in dielectric materials named as ferroelectrics and this phenomenon is based on the change in dipolar entropy by application of electric field under adiabatic conditions.[13] The total entropy of the ferroelectric material is equal to the sum of dipolar subsystem and thermal subsytem (given in Equation 1.4). Therefore the electrocaloric effect could be defined as the exchange entropy between these two subsystem.[14]

$$S_{total}(T) = S_{dipolar} + S_{phonon} \tag{1.4}$$

When the electric field is applied to the ferroelectric materials, the dipolar orientation occurs. Change in the entropy of the dipolar subsystem is balanced with a change (increase) in thermal subsystem to keep the total entropy constant under adiabatic conditions and this leads to increase in temperature of the ferroelectric material. When the electric field is removed from the system the material cools down. Figure 1.8 shows the schematic representation of the ferroelectric dipoles under applied electric field.

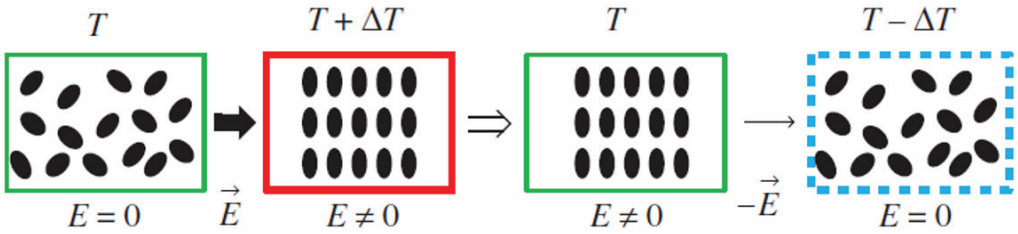

Figure 1.8. Schematic representation of dipoles under applied electric field.[14]

The alternative cooling technologies become a necessity due to halocarbon gases that are emitted by existing cooling technologies. The electrocaloric effect is a promising

alternative for cooling technology. Figure 1.9 shows the comparison between electrocaloric and vapor-compression cooling cycle.

In the beginning, the dipoles of the materials are randomly oriented and application of electric field causes alignment of the dipoles and dipolar entropy decreases. Material heats up to keep the total entropy constant. This polarization process is equvalent to the adiabatic compression step of current cooling technology. Then, resulting heat is removed to the cold sink part of the electrocaloric coolers and electric field is kept constant to prevent reabsorption of the resulting heat. Next, the electric field is removed and dipoles become randomly oriented. Therefore, material cools down. This stage is equvalent to the expansion step of the vapor compression technology. Finally, the negative heat is transferred to the hot sink of the electrocaloric coolers and the cycle is closed.

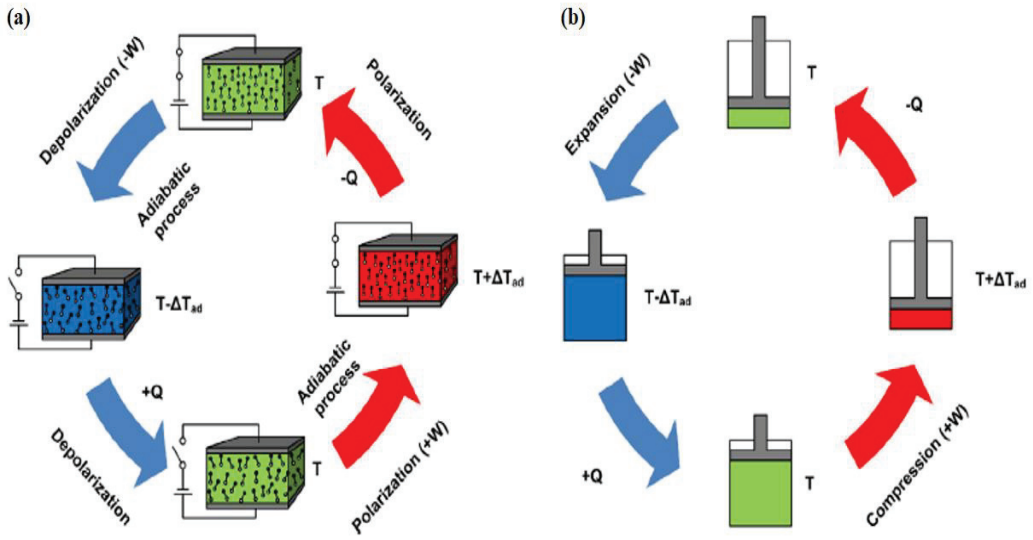

Figure 1.9. Comparison between the (a) electrocaloric cooling cycle and (b) the vapor-compression cycle.[15]

1.2.3. Measurement Methods for ECE

One of the most important part of electrocaloric effect (ECE) studies is accurate and precise measurement of ECE. ECE can be measured by using either the direct or indirect method.

1.2.3.1. Direct Method

The temperature change or the resulting heat in the material caused by the application of electric field is directly measured in this type of measurement method using the differential scanning calorimeter (DSC) or adiabatic calorimeter.

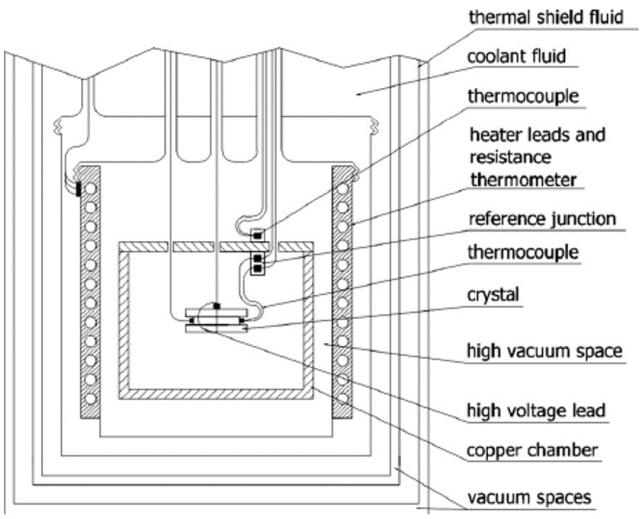

Figure 1.10. Schematic representation of an adiabatic calorimeter.[13]

In the adiabatic calorimeter, the sample in the thermally insulated container is exposed to the electric field and Figure 1.10 shows the schematic representation of adiabatic calorimeter that not only measure the ECE as a function of temperature but also the polarization. With this method a temperature change of 10^{-4} K can be measured. However, there are some issues that need to be considered in order to determine the ECE precisely. The thermocouples, electrodes or any parts used in the measurement should have very small heat capacity compared to sample. Thermal insulation must also be enough for precise determination of temperature change of sample.[13]

In the DSC method, the equal heat flows are applied to the sample and reference while the electrocaloric material or sample exhibit a temperature change caused by absorbtion or emission of heat due to electrocaloric effect. Precise temperature sensors record this change. Schematic representation of modified DSC is shown in Figure 1.11 (a). Figure 1.11 (b) shows the heat flow occurring in the sample measured by DSC method. An exothermic temperature change occurs in the sample with the applied electric field. When the electric field is removed, the DSC signal decreases to the baseline level.

The endothermic peak is observed when the material cools down below the baseline with the absence of electric field. However, it is difficult to provide adiabatic conditions in the DSC method and the adibatic temperature change can only be determined correctly if the electric field is switched on very quickly.[13]

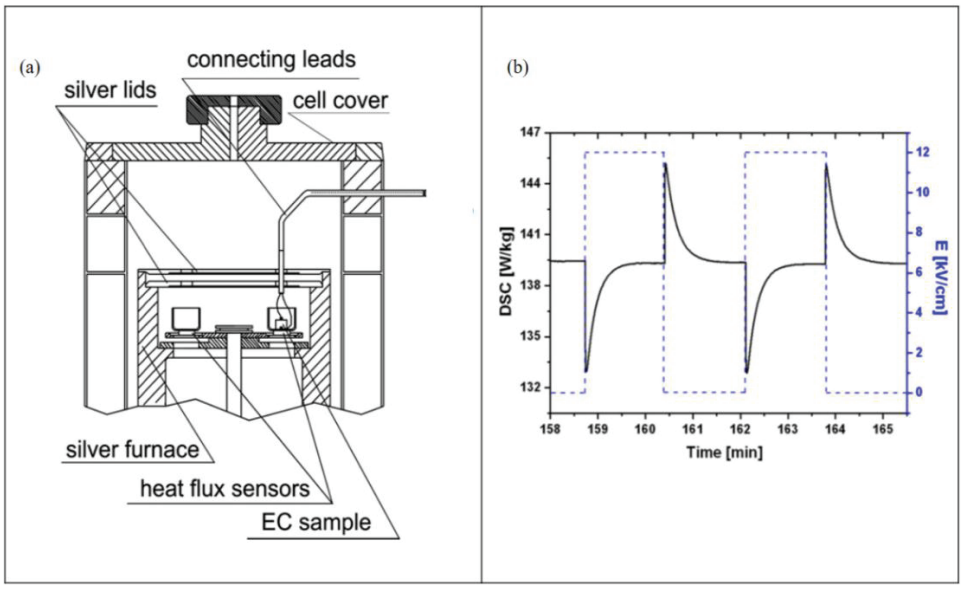

Figure 1.11. (a) Schematic representation of a modified DSC. (b) Example of heat flow of a material under an applied electric field.[13]

1.2.3.2. Indirect Method

The indirect determination of the electrocaloric effect is based on the Maxwell relation (Equation 1.5).

$$\left(\frac{\partial P}{\partial T}\right)_E = \left(\frac{\partial S}{\partial E}\right)_T \tag{1.5}$$

To obtain ΔT value, the following electrocaloric temperature change formula (Equation 1.6) is used. Here, E_1 and E_2 are the initial and final applied electric field, respectively. C_p is the heat capacity of the sample determined by DSC method and ρ denotes the density of the material. Equation 1.7 represents the adiabatic entropy change formula.

$$\Delta T = -\frac{T}{\rho C_p}\int_{E_1}^{E_2}\left(\frac{\partial P}{\partial T}\right)_E dE \tag{1.6}$$

$$\Delta S = -\frac{1}{\rho}\int_{E_1}^{E_2}\left(\frac{\partial P}{\partial T}\right) dE \tag{1.7}$$

The electrocaloric temperature change (ΔT) is determined by using polarization versus temperature (P-T) graphs obtained from the upper branches of the measured hysteresis loops at different temperature and constant electric field. The slope of P-T curve is obtained either by numerical differentiation (Equation 1.8) or by fitting P-T curves with a polynomial and then differentiating the curves.

$$\left(\frac{\partial P}{\partial T}\right)_E = \frac{1}{2} * \left(\frac{P_n - P_{n-1}}{T_n - T_{n-1}} + \frac{P_{n+1} - P_n}{T_{n+1} - T_n}\right) \tag{1.8}$$

Indirect determination of electrocaloric effect is more easier than direct determinaion. Therefore, it is used by many groups.

However, there are some factors that restrict the applicability of the indirect method. It is not a correct approach to determine the electrocaloric temperature changes of the non-ergodic relaxor samples (mentioned in section 1.1.1). Very low relaxation times of these materials limit the reproducibility of the method.[13] In addition, saturated polarization curves should be used when using the indirect method.

1.2.4. Application Areas

As mentioned earlier, the need for alternative cooling technologies increases due to the negative effects of existing cooling tecnologies on the environment. Several consortiums have been established to support the research on alternative cooling technologies and studies have been accelerated. One of them is CaloriCool™ - The Caloric Materials Consortium. CaloriCool™ includes Pacific Northwest and Oak Ridge National Laboratories, University of Maryland, Pennsylvania State University, GE Global Research, United Technologies Research Center, Astronautics Corporation of America, and Citrine Informatics.

Some groups have focused on prototype studies. The most important one among these studies is a small cooling device made by the group in the University of California. This device uses a thin, flexible and elastic electrocaloric polymer that is shown in Figure 1.12 (a). In addition, a process called electrostatic activation is used to make this device more energy efficient than traditional methods. This allows quick transfer of heat from one side to another. This device can be used to prevent heating of smartphones and laptops, or can be used for personal conditioning in wearable clothing.[16] Figure 1.12 (b) shows the result of the experiment. The difference in the temperature of the battery with and without the EC cooling device is quite large.

Considering all these studies, prototypes and the properties and advantages of electrocaloric effect, ECE is a promising alternative to existing cooling technologies.

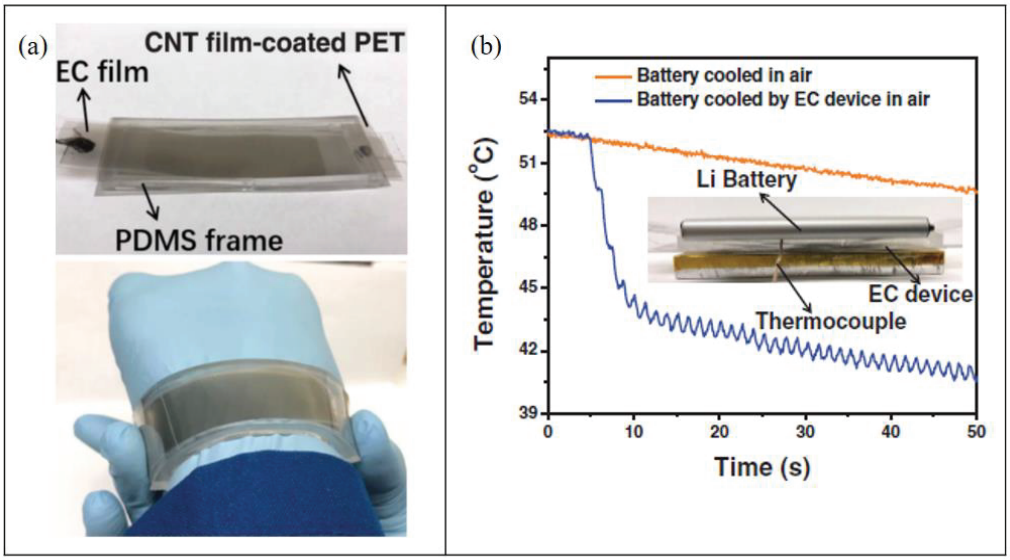

Figure 1.12. (a) The flexible electrocaloric polymer. (b) The temperature of smartphone battery with and without an electrocaloric device.[16]

1.3. Electrocaloric Materials

In this section, lead-containing and lead-free electrocaloric materials studied in the literature will be explained and compared in detail.

These materials are in the form of polycrystalline samples, single crystals, thin film or thick films, consisting of ceramics or polymers. When the electrocaloric response of these forms of materials are compared, the single crystals are not suitable for

application because of the difficulties and cost of fabrication. Thin and thick films have a high electrocaloric responses under a high electric field however this material form is not suitable for macro-cooling applications because of the volumetric reason. (Only very small areas can be cooled.) Therefore, researchers focused on the polymers and polycrystalline ceramics.

1.3.1. Lead-Containing Perovskites

As previously mentioned in Section 1.2.1, the electrocaloric effect was discovered in Rochelle salt and KH_2PO_4. Obtained electrocaloric temperature changes from these materials were very small. The electrocaloric effect become popular again with the discovery of giant 12 K temperature change in $PbZr_xTi_{(1-x)}O_3$ (PZT).[17] The reason for the high temperature change obtained in PZT is that this material undergoes AFE-FE phase transition. [17]

One of the most studied lead-containing electrocalorics are $(1-x)PbZn_{1/3}Nb_{2/3}O_3$-$(x)PbTiO_3$ (PZN-PT)[18] systems and PMN-PT.[19–27] The main reason for this is that it has a high electromechanical effect in the MBP region and maximum ECE is obtained in the same region.

$Pb_{0.99}Nb_{0.02}(Zr_{0.75}Sn_{0.20}Ti_{0.05})$ (PNZST) is another material that exhibit a high temperature change among lead-containing electrocaloric materials.[28] The $PbSc_{1/2}Ta_{1/2}O_3$ (PST) ceramic studied by the same group also showed a high ECE response under high electric field.[29]

Table 1.1 shows and summarizes the electrocaloric reponses or temperature changes (ΔT) of lead-containing materials with their form and applied electric fields. The electrocaloric responses of lead-containing materials are relatively high however these values are obtained under high electric field (ΔE). The important parameter to compare the electrocaloric effects of materials is the temperature change per unit electric field, that is $\Delta T/\Delta E$.

Development of lead-containing electrocaloric materials is pushed aside because of the toxic effect of lead element since the main goal and idea in the electrocaloric effect is to develop an environmentally friendly alternative cooling technology. Therefore, researchers focus to develop lead-free electrocaloric materials.

Table 1.1. The electrocaloric responses of the most important lead-containing materials.

Material	Form of Material	T(°C)	ΔE (kV/cm)	ΔT(K)	ΔT/ΔE (10^{-6}m.K/V)	Measurement Method	Ref.
PZT (95/05)	Thin Film (350 nm)	222	776	12	0.15	Indirect	[17]
PZN-PT (92/08)	<110> Single Crystal	180	12	0.23	0.21	Direct	[18]
PMN-PT (92/08)	Ceramic	23	15	1.4	0.93	Direct	[19]
PMN-PT (90/10)	<111> Single crystal	55	40	1	0.25	Indirect	[20]
PMN-PT (87/13)	Ceramic	70	24	0.56	0.23	Direct	[27]
PMN-PT (85/15)	Ceramic	17	16	1.7	1.06	Direct	[26]
PMN-PT (75/25)	Ceramic	120	14	0.49	0.36	Direct	[24]
PMN-PT (75/25)	<111> Single crystal	100	10	0.78	0.78	Direct	[25]
PMN-PT (72/28)	<011> Single crystal	130	9	0.53	0.59	Direct	[22]
PMN-PT (72/28)	<111> Single crystal	130	12	2.7	2.25	Indirect	[23]
PMN-PT (65/35)	Thin Film (240 nm)	140	750	31	0.41	Indirect	[21]
PNZST	Ceramic	163	25	2.6	1.04	Indirect	[28]
PST (50/50)	Multilayer Capacitor	23	138	2.4	0.17	Direct	[29]

1.3.2. Lead-Free Perovskites

Among the lead-free ferroelectric materials, the most studied one is $BaTiO_3$ (BT). This material has a perovskite structure and has three structural phase transition around -

80°C, 5°C and 125°C from rhombohedral to orthorhombic, orthorhombic to tetragonal and tetragonal to cubic with the polar directions <111>, <110> and <001> ,respectively. Higly polarisable character and the large dielectric strength of $BaTiO_3$ makes the material a potential candidate for electrocaloric cooling.[30]

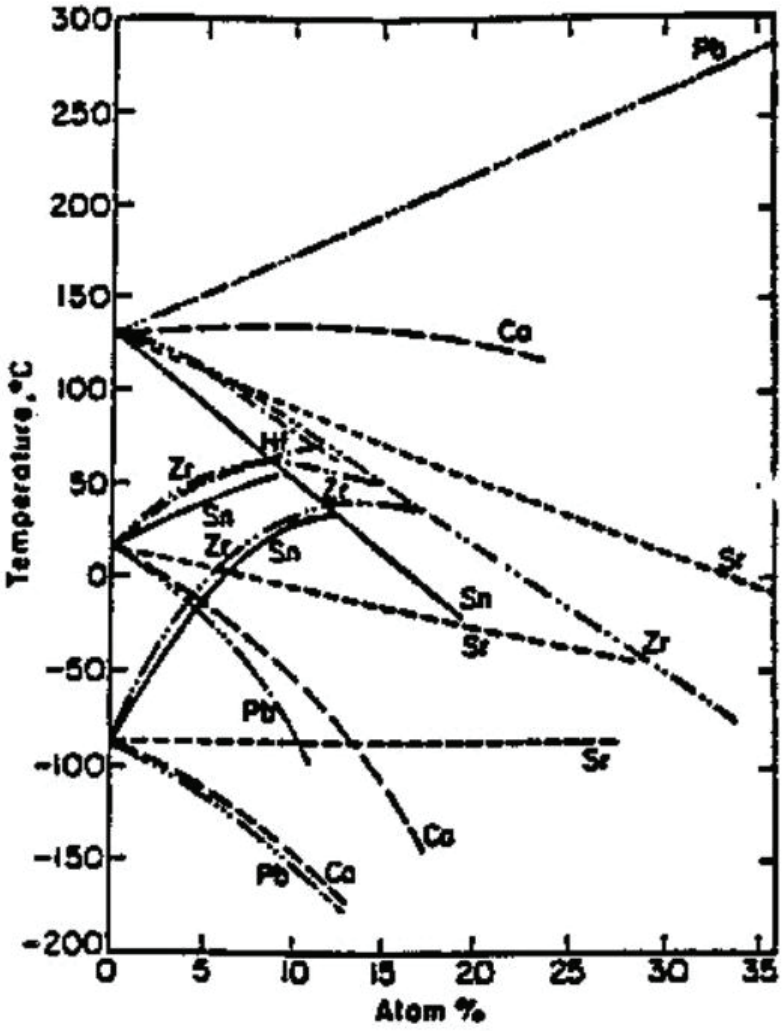

Figure 1.13. A and B site dopants for $BaTiO_3$ and the effect on transition temperatures.[30]

As mentioned earlier, the major advantage of ABO_3 or perovskite structure is that it allows doping at both A and B-sites. The factors that should be taken into consideration during the doping process is the selection of compatible dopant atom based on the ionic valency and ionic radius. Thus the distortion of the crystal structure is minimized and charge neutrality will be conserved without any charge defect. The effect of common dopants on the phase transition temperautres of $BaTiO_3$ are shown in Figure 1.13.

Table 1.2. The electrocaloric responses of the most important lead-free materials.

Material	Form of Material	T(°C)	ΔE (kV/cm)	ΔT(K)	ΔT/ΔE (10^{-6} m.K/V)	Measurement Method	Ref.
$BaTiO_3$	Ceramic	128	10	1.3	1.3	Indirect	31
$BaTiO_3$	Single Crystal	129	12	0.9	0.75	Direct	33
$BaTi_{1-x}Sn_xO_3$ (x=0.105)	Ceramic	28	20	0.61	0.31	Indirect	37
$Ba_{1-x}Ca_xTi_{0,95}Sn_{0,05}O_3$ (x=0.05)	Ceramic	113	10.8	0.53	0.49	Indirect	38
$Ba(Zr_{0,1}Ti_{0,9})_{1-x}Sn_xO_3$ (x=0.075)	Ceramic	30	8.7	0.19	0.22	Indirect	36
$BaHf_xTi_{1-x}O_3$ (x=0.11)	Ceramic	70	10	0.35	0.35	Indirect	41
$Ba_{0,85}Ca_{0,15}Ti_{1-x}Hf_xO_3$ (x=006)	Ceramic	128	21	0.65	0.31	Indirect	39
$Ba_{0,8}Ca_{0,2}(Zr_xTi_{1-x})O_3$ (x=0.04)	Ceramic	113	7.95	0.27	0.34	Indirect	40
$BaSn_{0.1}Ti_{0.9}O_3$	Ceramic	64	15	0.48	0.32	Indirect	42
NBBST0.10	Ceramic	110	40	0.22	0.18	Indirect	43
NBT-ST (x=0.25)	Ceramic	60	50	1.64	0.33	Indirect	44
KNN-ST	Ceramic	67	159	1.9	0.12	Direct	45
$0.94Bi_{0.5}Na_{0.5}TiO_3$-$0.06KNbO_3$	Ceramic	76	70	1.73	0.24	Indirect	46
$Na_{0.5}Bi_{0.5}TiO_3$–$BaTiO_3$	Ceramic	25	50	0.12	0.24	Indirect	47
0.82NBT–0.18KBT	Ceramic	80	77	1.62	0.21	Indirect	47
0.90NBT-0.05KBT-0.05BT	Ceramic	90	74	1.47	0.2	Indirect	47
0.96KNNSb-0.04BNK-0.5Zr	Ceramic	77	40	0.51	0.13	Indirect	48
$0.97KNN-0.03LiSbO_3$	Ceramic	72	40	3.33	0.83	Indirect	49

The electrocaloric temperature changes obtained from pure and doped BT studies[31–37] are listed in Table 1.2 with applied electric field and phase transition

temperatures. Doping did not increase the electrocaloric responsivity of BT. However maximum the response temperature or T_c was reduced from 128°C to 28°C. One of the main objectives in electrocaloric research is to bring the phase transition temperature (T_c) closer to room temperature for applications.

Bi-based ferroelectric materials wiht lone pair electrons are considered as one of the most promising alternatives to lone pair electron containing Pb-based perovskites. Most important Bi-based systems[38–44] are listed in Table 1.2 with their electrocaloric response.

The resulting temperature changes (ΔT) that is obtained from lead-free materials are not sufficient yet to integrate these materials into refrigeration technologies. For this reason, many studies are carried out to improve the electrocaloric properties of materials. Therefore, it is necessary to understand the mechanisms that enhance the electrocaloric effect of materials.

1.4. Mechanisms to Enhance the Electrocaloric Effect

In this section, the mechanisms that affect the electrocaloric effect will be disccussed.

1.4.1. First Order Phase Transition, Diffuse Transition, Relaxor Ferroelectricity

The effects of doping that changes the ferroelectric phase transition characteristics and the phase transition temperature will be discussed.

As mentioned earlier, the perovskite structure (ABO_3) of ferroelectric materials allows the doping to both A and B sites. Due to doping, the phase transition character of the normal ferroelectrics changes from, namely "**the first order phase transition**", where the polarization changes sharply with respect to the temperature and the resulting large increase in $\partial P/\partial T$ leads to high electrocaloric temperature change (ΔT) value in a narrow temperature range. Increasing doping affects the phase transition character and the dopant amount increases, first the diff**use phase transition (DPT)** and then **relaxor property** is observed. One of the main objectives of doping is to bring the operating temperature closer to room temperature for cooling applications. The operating temperature range of

the materials that exhibit diffuse phase transition or relaxor properties is spread over a wide temperature range. Doping can be used to achieve this. To sum up, doping is essential for ECE because the ΔT value obtained from the materials with the first order phase transition character is high but only in a narrow temperature range. Therefore, DPT or relaxor property are promising for applications.

Relaxor ferroelectric materials include polar nano regions (PNRs) which increase the entropy that might enhance the ECE. The most important relaxor ferroelectrics are PMN and PMN-10PT. These materials show strong relaxor property and the resulting ΔT values are quite high in a broad temperature range. Among lead-free ferroelectrics, Hf and Zr doped BT are the important relaxor ferroelectric materials.[34,35]

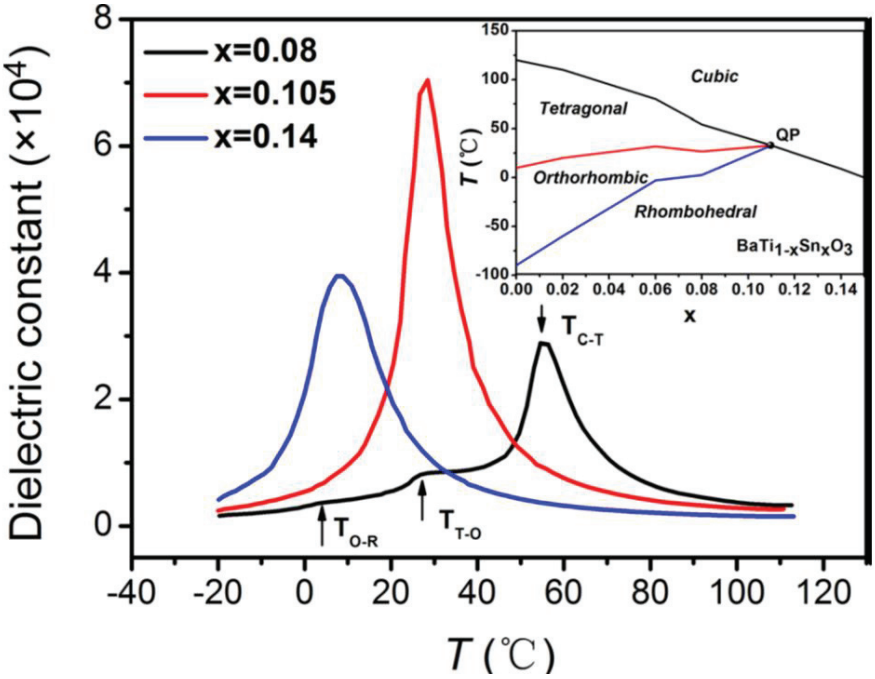

Figure 1.14. The phase diagram of $BaTi_{1-x}Sn_xO_3$ ceramic.[32]

There is another mechanism called as critical point where more than one ferroelectric phase coexist. The most relevant studies of critical point containing systems in the literature are done on Sn, Zr and Hf doped BT.[32,36]. Figure 1.14 shows the phase diagram obtained for Sn-doped BT ($BaTi_{1-x}Sn_xO_3$) and the critical point is observed in the x = 0.105 composition and the ΔT value is very high for this composition. In critical point region, the multiphase coexistance leads to larger EC temperature change due to the ease of inducing remarkable polarization/entropy change with application of electric field

as well as large entropy change caused by multiphase coexistence. The disadvantage of critical point is that the high ΔT is observed in a narrow temperature range.

Considering all these studies, importance of doping process is well understood and the studies mainly continue on BT and NBT-based ceramic materials.

1.4.2. Morphotropic Phase Boundary (MPB)

Another mechanism that enhances ECE is called as morphotropic phase boundary (MPB). The morphotropic phase boundary is an area of phase diagram where two ferroelectric phase coexist at a certain composition and the crystal structure could easily change from the first ferroelectric phase to another by changing the composition. This leads to more polarization directions and therefore it is possible to orient the dipoles by applying a lower electric field. Also, a large enhancement of the electromechanical properties is observed in the MBP region in e.g. PZT[45] and PMN-PT[46] systems and their piezoelectric coefficients equal to 750 pm/V and 700 pm/V, respectively. The field-induced polarization rotations could lead to unit cell deformation and enhance the piezoelectric and dielectric properties and the electrical polarization value is maximum at the MBP region.

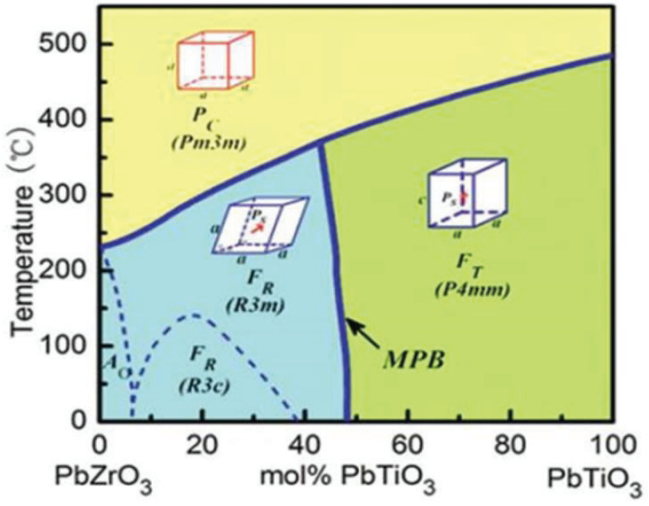

Figure 1.15. The phase diagram of $PbZr_{1-x}Ti_xO_3$.[47]

Figure 1.15 shows the phase diagram of $PbZr_{1-x}Ti_xO_3$ ceramic which is the best piezoelectric material. Composition-dependent dielectric constant, polarization and

piezoelectric constant graphs of this system where the MBP is observed in x = 0.47 composition, are displayed respectively in Figure 1.16 (a)-(c). Considering these graphs, the importance of the MBP is quite clear.

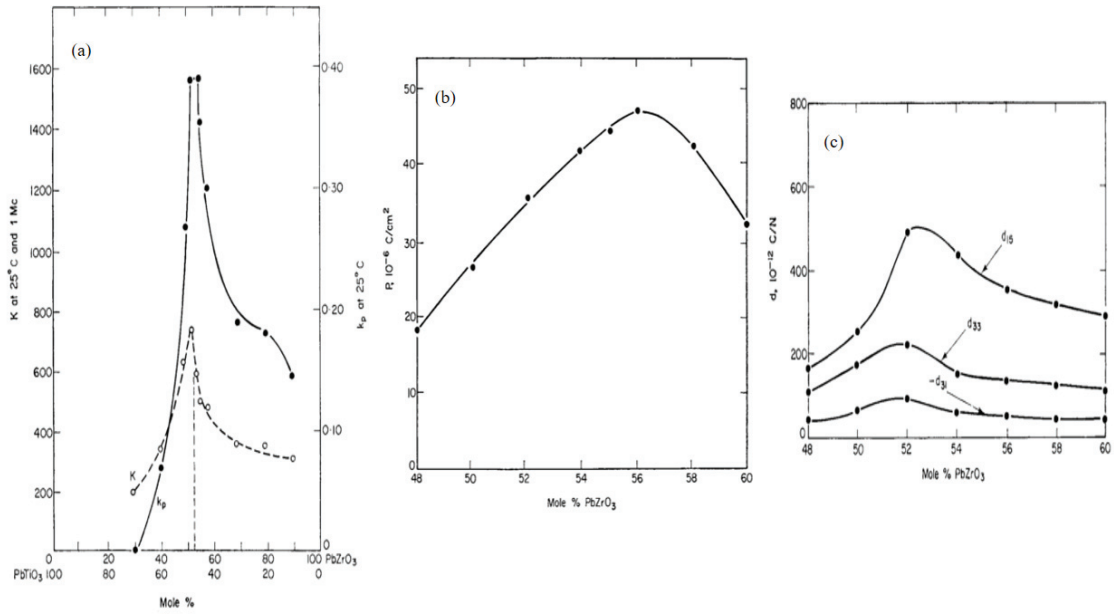

Figure 1.16. (a) Dielectric constant versus composition for the system $PbTO_3$-$PbZrO_3$. (b) Polarization versus composition for the system $PbTiO_3$-$PbZrO_3$. (c) Piezoelectric constant versus temperature for $Pb(Ti_{0.47}Zr_{0.53})O_3$.[30]

1.4.3. Ferroelectric-Antiferroelectric (FE-AFE) Phase Transitions

The antiferroelectricity previously described in section 1.1.2 was first observed in $PbZrO_3$, followed by lead-free materials such as $(Na_{1/2}Bi_{1/2})O_3$, $AgNbO_3$ and $NaNbO_3$ and their solid solutions.[48] As previously mentioned, an arrangement of the antiparallel dipole order exists in antiferroelectrics. Under the application of electric field, the low energy barrier between the ferroelectric phase and the antiferroelectric phase causes a switching from antiferroelectric to ferroelectric phase. When the applied electric field is large enough, the dipoles of the metastable ferroelectric phase are oriented and the electric field induced phase transition leads to a large volume expansion.[10] Therefore, the piezoelectric properties obtained from materials having this type of phase transition are quite high.[49,50]

All of these properties were observed in Pb-based materials ($PbZrO_3$, PNZST).[48] Although these materials exhibit outstanding properties in engineering applications, the

toxicity of the lead causes environmental concerns and the investigation of lead-free materials having AFE-FE phase transition is of particular interest. $(Na_{1/2}Bi_{1/2})O_3$ and its solid solution ($(1-x)(Na_{1/2}Bi_{1/2})O_3$-$xBaTiO_3$,NBT-BT) are the most important ones among this type of lead-free materials.

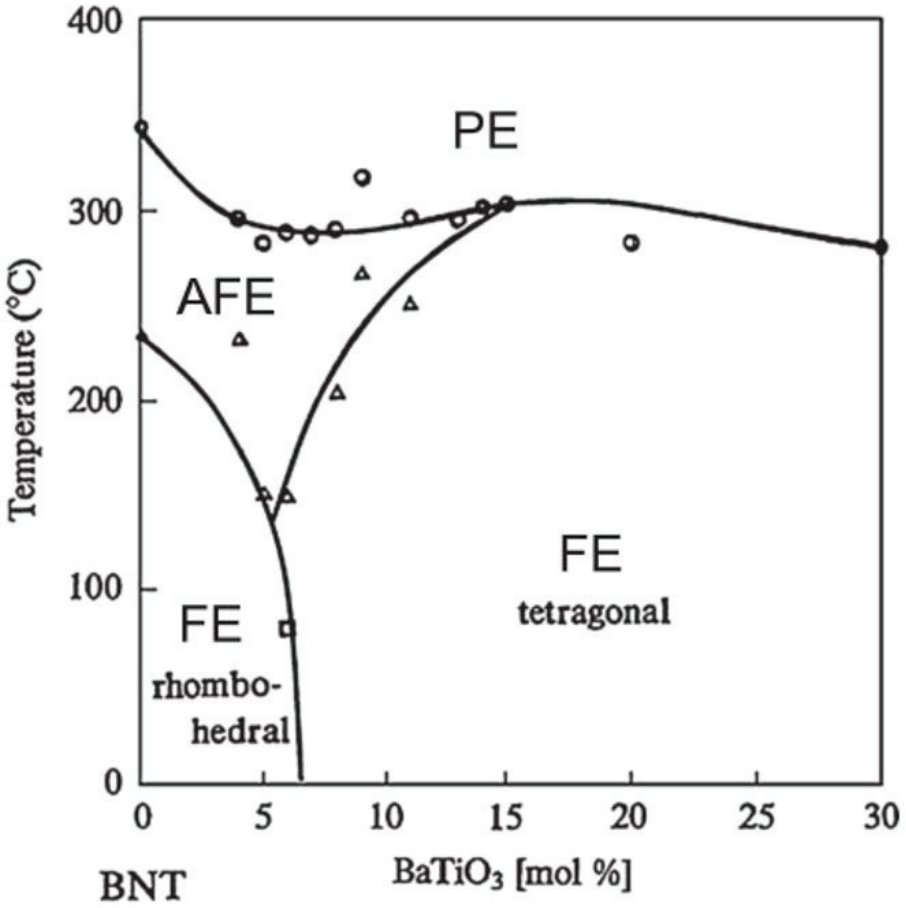

Figure 1.17. Phase diagram of $(1-x)(Na_{1/2}Bi_{1/2})O_3$-$xBaTiO_3$.[48]

Figure 1.17 belongs to the phase diagram of NBT-BT material and shows the compositions having FE-AFE phase transition. The electrocaloric effect obtained in the NBT-BT with x=0.07 composition is quite high due to the presence of a MBP and FE-AFE phase transitions observed in that composition. The ferroelectric phase induced by the electric field in this composition is a metastable phase and FE(rhombohedral) to FE(tetragonal) phase transition can be observed depending on the applied electric field. With a small amount of $(K_{0.5}Na_{0.5})NbO_3$ (KNN) doping, this ferroelectric phase becomes more stable and thus the strain is increased [48,51]

Table 1.3 shows the electrocaloric properties of the materials[17,39,41,52,53] with FE-AFE phase transitions.

Table 1.3. The electrocaloric responses of the materials having FE-AFE phase transition.

Material	Form of Material	T (°C)	ΔE (kV/cm)	ΔT (K)	ΔT/ΔE (10^{-6}m.K/V)	Method	Ref
$Pb_{0.99}Nb_{0.02}(Zr_{0.75}Sn_{0.20}Ti_{0.05})_{0.98}O_3$	Ceramic	161	30	2.5	0.83	Direct	57
PZT (95/5)	Thin Film (350 nm)	222	776	12	0.15	Indirect	17
NBT-ST (x=0.25)	Ceramic	60	50	1.64	0.33	Indirect	44
BNT–0.06KN	Ceramic	76	70	1.73	0.25	Indirect	46
0.7BNT-0.3BT	Ceramic	150	50	2.1	0.42	Indirect	48

1.5. Motivation of the Thesis

In 2011 Chukka et al. found a giant EC temperature change (ΔT_{max}) as 2.7 K at 127°C in MPB composition (0.7PMN-0.3PT) of single crystal of PMN-PT at 12 kV/cm where the EC efficiency ($\Delta T_{max}/\Delta E$ (10-6 K.m/V)) equals to 2,25.[54] This giant ECE is a proof that MPB is an effective mechanism. The coexistence of different ferroelectric phases leads to an increase of the possible polarization directions. Therefore, polarization of the ceramics becomes easier with application of smaller electric field and this enhance the EC efficiency. In this respect, motivation of this thesis is to investigate the electrocaloric effect of Bi-based $(1-x)BaTiO_3-xBi(Li_{1/3}Ti_{2/3})O_3$ $0.03\leq x\leq 0.08$ system with a MPB.

According to the XRD measurements (Figure 1.18(a)-(b)) of the article[55], tetragonal peak splitting $(002)_T/(200)_T$ was observed for the $x\leq 0.07$ compositions and x=0.10 sample showed orthorhombic peak splitting $(022)_O/(200)_O$. Thus, it has been suggested that there is an MPB between x=0.07 and 0.10 compositions. Piezoelectric (d_{33}) coefficient (Figure 1.18 (c)) for x=0.07 composition gives the maximum value at room temperature confirming the existence of the MPB.

In the dielectric measurements (Figure 1.19), a dielectric peak at around 130°C was observed in all compositions, which is the Curie temperature of the samples. Also, depending on the composition, a frequency-dependent anomaly at lower temperatures is clearly observed. Such double peak behavior is caused by microstructures called core-shell. Dielectric measurements confirm the existence of the core-shell structure. The shell region includes ferroelectric nanodomains and there are large ferroelectric lamellar domains within the core. The reason for the formation of core-shell structure is incomplete diffusion process due to the limited sintering temperature where a volatile precursor is involved in the solid solution such as Li_2CO_3 and Bi_2O_3.

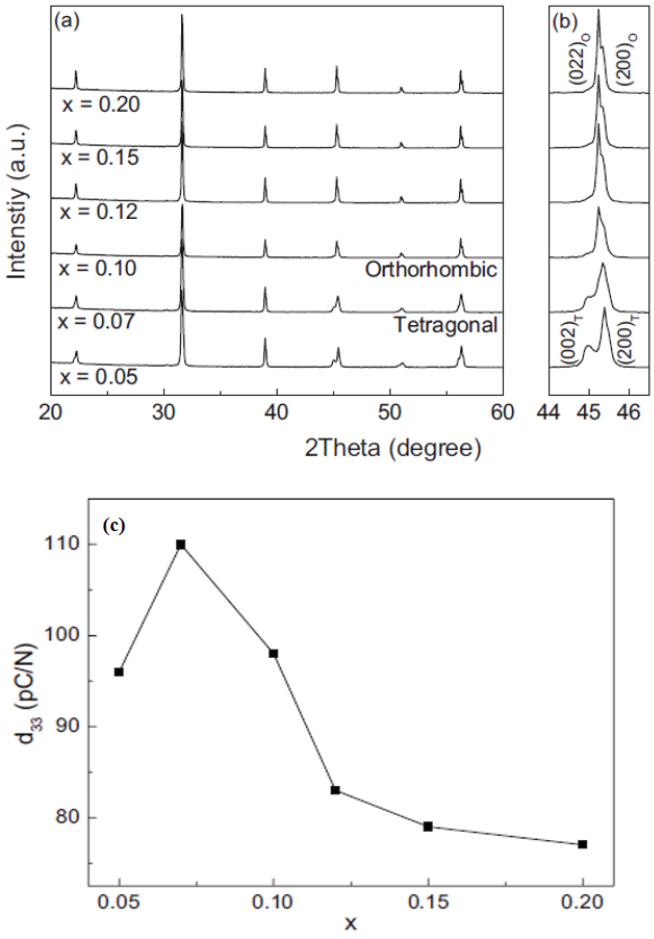

Figure 1.18. XRD patterns of $(1-x)BaTiO_3-xBi(Li_{1/3}Ti_{2/3})O_3$ between (a) 20-60° and (b) 44-46.5°. (c) Piezoelectric (d_{33}) coefficient of all $(1-x)BaTiO_3-xBi(Li_{1/3}Ti_{2/3})O_3$ ceramics.[55]

This situation is common in BT-$Bi(X)TiO_3$ solid solutions[56,57] due to the limited sintering temperature of these ceramics to prevent the loss of volatile Bi element. During

sintering, diffusion proceeds faster through the grain boundaries. $BaTiO_3$ (BT) forms first and $Bi(Li_{1/3}Ti_{2/3})O_3$ (BLT) diffusion takes place more quickly along the grain boundaries than through the grains.

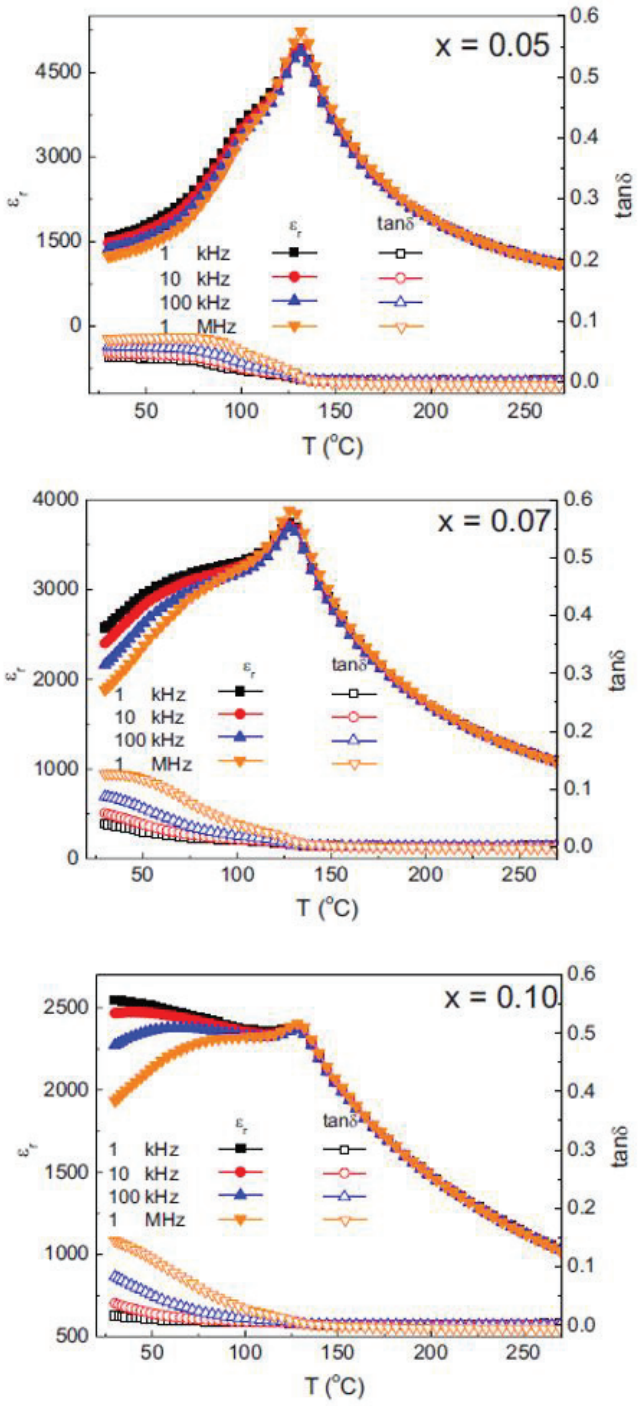

Figure 1.19: Dielectric behavior of $(1-x)BaTiO_3-xBi(Li_{1/3}Ti_{2/3})O_3$ ceramics as a function of temperature measured at 1 kHz, 10 kHz, 100 kHz and 1 MHz.[55]

The incomplete diffusion after sintering leads to formation of the core-shell structure where the core area is BT-rich with minimum amount of BLT, while the shell region is BLT-rich. The peak around 130°C which is observed in all compositions in the temperature dependent dielectric measurements is associated with the core and corresponds to the T_C of BT. The second frequency dependent anomaly corresponds to contribution from the shell which is rich in BLT. Large BLT content distrupts ferroelectric order and induces frequency dependent relaxor ferroelectric behavior in the dielectric constant.

In the BT ceramics, where the core-shell structure is desired, the dielectric peak observed at lower temperatures due to the shell contribution provides high dielectric constant in a wide temperature range. This is especially important for commercial capacitor applications.[58,59]

The aim of this thesis is to investigate the effect of core-shell microstructure and MPB on the electrocaloric response by changing the synthesis conditions of $(1-x)BaTiO_3$-$xBi(Li_{1/3}Ti_{2/3})O_3$ ($0 \leq x \leq 0.2$) ceramics. Even though the ferroelectric, piezoelectric and dielectric properties of BT-BLT is reported by Ma. et al., high temperature ferroelectric properties have not been reported and electrocaloric properties of this system are not known.

CHAPTER 2

EXPERIMENTAL METHODS

The synthesis conditions and characterization techniques used for microstructure and phase analysis and methods used in electrical measurements will be explained.

2.1. Material Preparation

In this section, different synthesis routes of the ceramics will be explained with their flow charts.

2.1.1. Synthesis Route-I

Figure 2.1 shows the flow chart of route-I. The powders of Bi_2O_3 (99.9%, Sigma-Aldrich), Li_2CO_3 (99.999%, Sigma-Aldrich), $BaCO_3$ (99.9%, entekno), TiO_2 (99.9%, Sigma-Aldrich) were used as starting materials and $(1-x)BaTiO_3-xBi(Li_{1/3}Ti_{2/3})O_3$ $0.03 \leq x \leq 0.10$ ceramic synthesis is initiated by drying of the starting powders at 200°C for 12 hours in oven. Stoichiometric amount of powders were mixed and homogenized in a ball mill (Retsch PM 100) in ethanol medium with 7 zirconia balls (diameter of 10 mm) in a Nalgene bottle (volume: 30 ml) with a 21:1 ball to powder mass ratio for 2 hours and then dried in an oven until all solvent is evaporated. The mixture was calcined at 1000°C for 5 hours.

The calcined powders were mixed with 2 wt % polyvinyl alcohol (PVA)-water solution, by using ball milling for 1 hour with the same milling conditions. PVA was used to facilitate pelletization of calcined powders. After all water is removed by drying at 80°C, the powders are pelletized at 375 MPa. Binder (PVA) was removed by heating at 600°C for 1 hour with ramp rate of 1°/min.

Sintering was performed at 1200°C for 3 hours for all compositions. Pellets were buried in the calcined powder to minimize the loss of Bi^{3+} and Li^{+} during sintering.

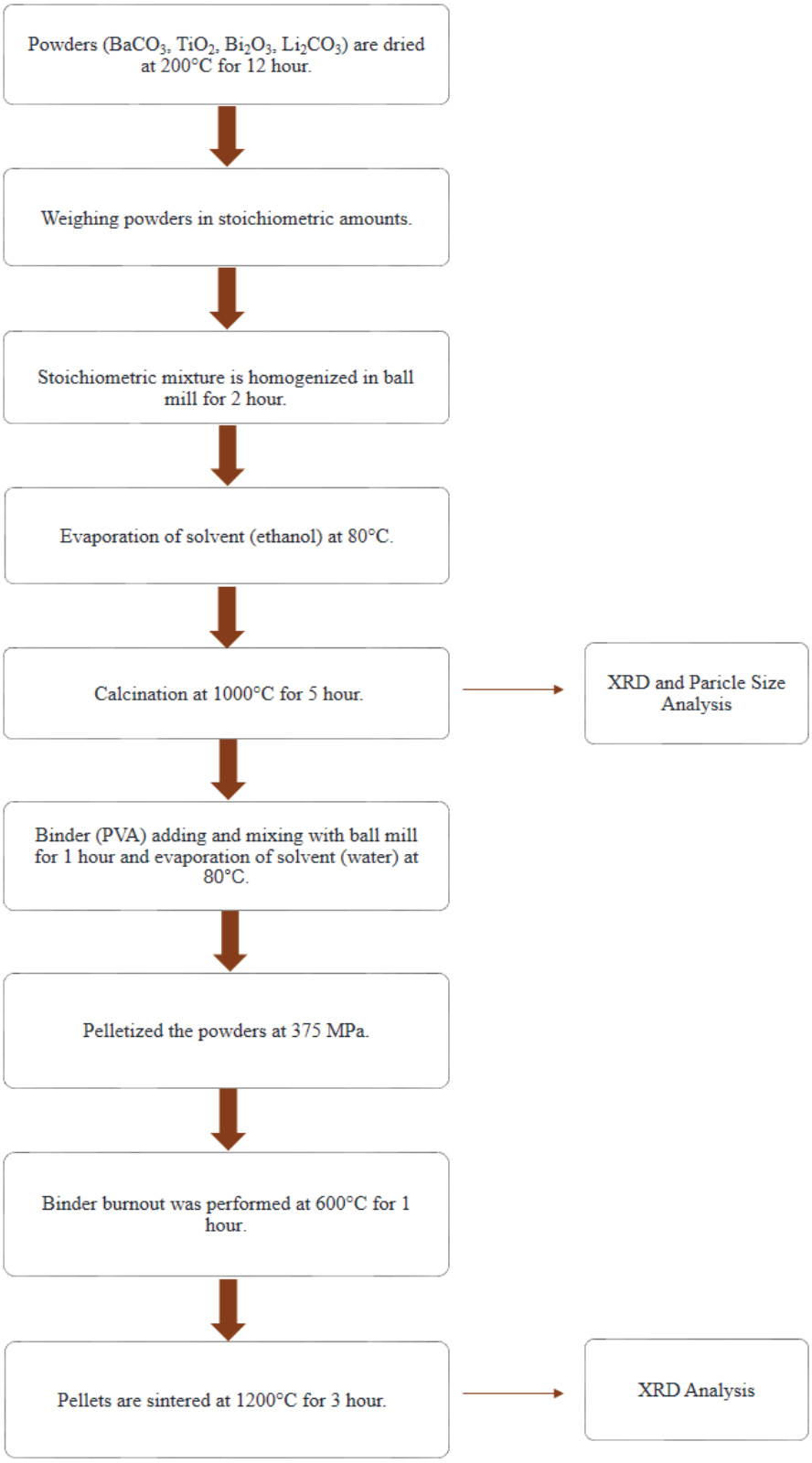

Figure 2.1. Flow chart of the synthesis (Route-I) and the used characterization methods.

2.1.2. Synthesis Route-II

Figure 2.2 shows the flow chart of route-II. The powders of Bi_2O_3 (99.9%, Sigma-Aldrich), Li_2CO_3 (99.999%, Sigma-Aldrich), $BaCO_3$ (99.9%, entekno), TiO_2 (99.9%, Sigma-Aldrich) were used as starting materials and $(1-x)BaTiO_3-xBi(Li_{1/3}Ti_{2/3})O_3$ $0.03 \leq x \leq 0.08$ ceramic synthesis is initiated by drying the starting powders at 200°C for 12 hours. Stoichiometric amount of powders were mixed and homogenized in a ball mill (Retsch PM 100) in ethanol medium with 160 zirconia balls (diameter of 5 mm) in a Nalgene bottle (volume: 30 ml) with a 10:1 ball to powder mass ratio for 6 hours and then dried in oven until all solvent is evaporated. The mixture was calcined at 900°C for 5 hours and then milled for another 6 hours under the same milling conditions. After drying, the powders were mixed with 2 wt % polyvinyl alcohol (PVA)-water solution by using ball milling for 4 hours with the same milling conditions and the dried powders were sieved with the help of 65 μm sieve that is used to prevent the negative effect of the agglomeration on the sintering kinetics. Then powders are pelletized at 375 MPa. Binder was burnouted at 600°C for 4 hours with ramp rate of 1°/min. The sintering was done between 1200°-1250°C for 3 hours, according to the BLT content. Pellets were buried in the calcined powder to minimize the loss of Bi^{3+} and Li^{+}.

For both synthesis routes, the surfaces of the sintered samples were polished with 600,1000 and 2000 mesh SiC sandpaper to prepare the samples for the measurements of density and electrical properties.

2.2. Characterization of the Materials

The used characterization methods for the synthesized ceramics are described in this section.

2.2.1. Particle Size Analysis

Particle size analysis is done by using dynamic light scattering (DLS). DLS is a technique used to determine the particle size distribution. When light hits to the particles, the light scatters in all directions (called as Rayleigh scattering) as a function of the size of the particles.[60]

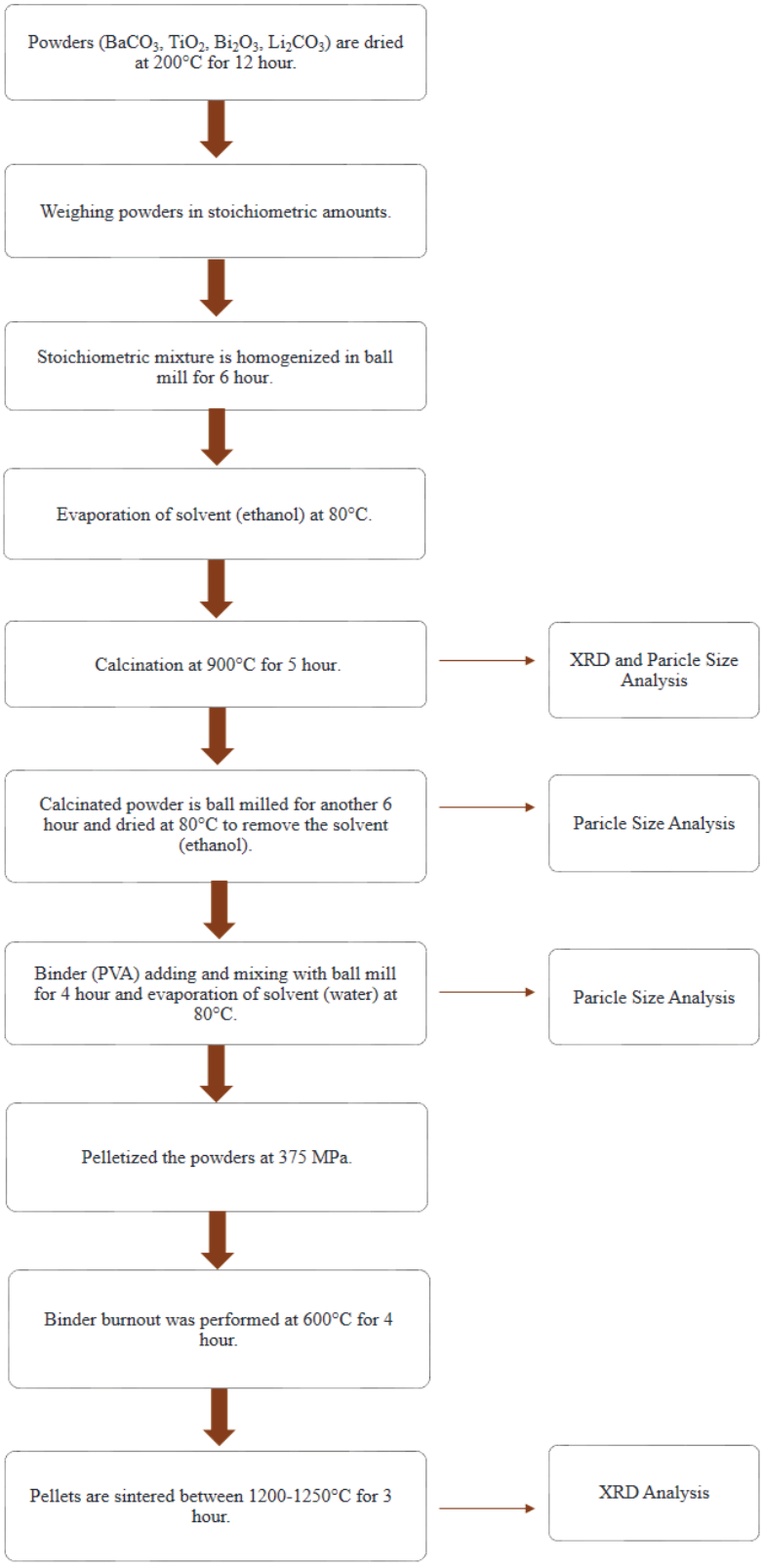

Figure 2.2. Flow chart of the synthesis (Route-II) and the used characterization methods.

Scattering intensity fluctuates over a time. Small molecules in the solution receive Brownian motion that cause to this fluctuation and the distance between the scattered molecules changes with time. The Brownian motion of the particles depend on their size, refractive index, measurement temperature and the viscosity of the solvent. The signal is read out only the constructive phases occurs and it carries the information about the fluctuation intensity of the scattered light as a function of the time. Figure 2.3 shows the schematic representation of the dynamic light scattering experiment.[61]

To measure the particle size of the ceramic samples, 5 mg of the milled powder was dissolved in 1.5 ml ethanol and ultrasonically disaggregated for 2 minutes. Then the measurement is carried out by using a dynamic light scattering instrument (DLS; Zetasizer Nano ZS, Malvern Instruments, Worcestershire, UK) provided by IZTECH Material Science and Engineering Department. The particle size distribution of the ceramics are determined by DLS measurements before and after the calcination and before the sintering process.

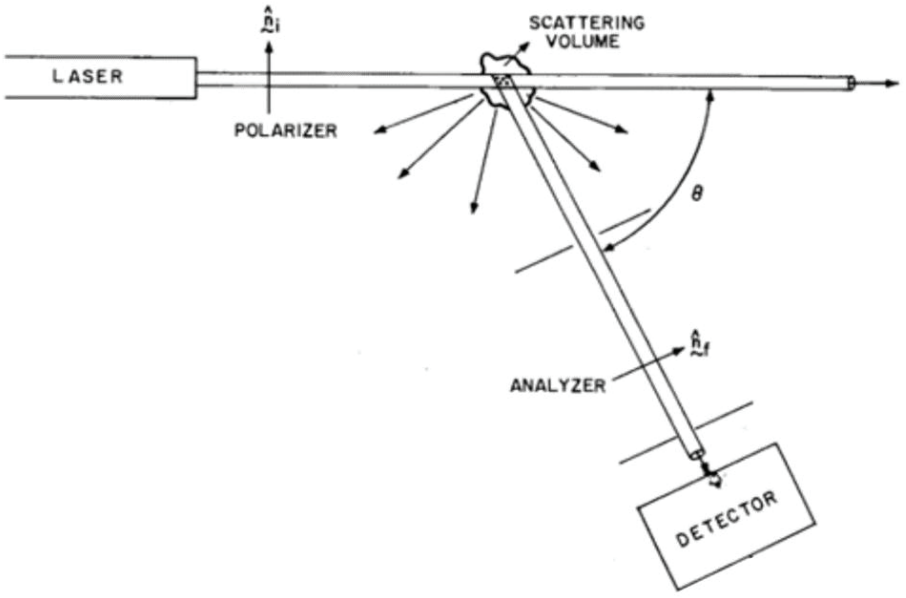

Figure 2.3. A schematic representation of the dynamic light scattering experiment.[61]

2.2.2. Archimedes' Method

The density of the sintered samples is measured based on the Archimedes' principle using the density determination kit of Radwag –AS 220 R2 analytical balance.

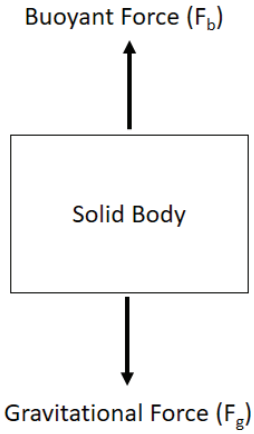

Figure 2.4. A schematic representation of the Archimedes' principle.

Archimedes' principle is based on the balance of the buoyant or upward force and the gravitational force acting on the sample. Figure 2.4 shows the schematic representation of the principle. The buoyant force (F_b) is produced by the liquid on the sample fully immersed in the liquid. This force is equal to the gravitational force (F_g), where;

$$F_g = m_f . g \qquad F_b = P_f . V_g$$

For an object having a volume V, the $F_g = \rho_w . V.g$, where the ρ_w is the density of the water. The mass of object in the air is (M), M= ρ.V, where the ρ is the density of the sample. The difference between the actual weight of an object and the magnitude of the buoyant force gives the apparent mass (M_{app}) of the sample that is the mass (M_w) when the object is immersed in water totally.

$$M_{app} = M_{actual} - F_b$$

$$M_w g = M.g - \rho_w . V . g$$

$$M_w = M - \rho_w . V \qquad , where\ V = {}^{M}/_{\rho}$$

$$Finally, \qquad \rho = \frac{M}{M - M_w} . \rho_w \tag{2.1}$$

2.2.3. X-Ray Diffraction

X-Ray Diffraction (XRD) was used to determine the symmetry of the phases and phase purity in calcined powder and also to obtain the information about the incorporation of the substituting atoms by following the shifts of the XRD peaks as a result of substitution. XRD measurements were done with a high resolution X-ray diffractometer (Philips X'Pert Pro) provided by the Izmir Institute of Technology (IZTECH) Material Research Center.

XRD can define the interatomic distances and angles and the positions of the atoms. This method is based on the fact that distances between atoms in the crystals and the wavelength of the X-rays that are of the similar magnitude (1 Å or 100 pm).[62]

X-ray diffraction patterns of the samples were collected with 0.0170 step size (°2θ) between 20-80 degrees. The scan step time (s) value for both calcined and sintered samples synthesized following route-I and calcined samples synthesized following route-II are equal to 15 seconds while the scan step time for sintered samples following route-II is increased to 54 seconds. The phase analyses of the X-ray diffraction patterns of samples were done by using search and match process in HighScore Plus program.[63]

2.2.4. Scanning Electron Microscopy

Scanning Electron Microscope (SEM) was used to determination of grain sizes, porosity of samples and identification of impurity phases that are not detected by XRD. Both secondary electron and back scattering (BS) imaging were used for these purposes. The SEM instruments used in this work are Philips XL 30S FEG with and EDX (Energy Dispersive X-Rays) detector provided by the IZTECH Material Research Center and Carl Zeiss 300VP provided by Izmir Katip Celebi University (IKCU) Central Research Laboratory.

In SEM, the focused beam of the electrons with high energy is used to produce image of a sample. Imaging the surface topography, morphology, chemical composition and crystalline structure is based on the interaction between electrons and the sample. After the beam is produced in the vacuum and pass through the electromagnetic fields and lenses, the beam is focused on the sample and interacts with it. Secondary electron emission, back-scattered electrons and X-rays are formed due to this interaction. Detector

collects the emission and converts it to signal. For morphology and topography analysis the secondary electrons are used. To see the contrast in samples with multiphases the preferred emission is the backscattered electrons. For composition information, the X-rays that are scattered by the sample surface are used with the help of the Energy Dispersion X-Rays (EDX) detector.[64] When the incident electron energy is sufficient to ionize the surface atoms, it causes the excitation of surface electrons to the higher energy levels. Due to relaxation of electrons to the lower energy levels, X-rays arev emitted and elemental analysis can be done.[65]

The sintered samples are polished by using 600, 1000 and 2000 mesh SiC sandpaper for SEM analysis. Thus, the surface morphological disorders were eliminated and scattering was minimized. After polishing an etching procedure is required to image the grains. In general, the etching process is carried out at a temperature of 100-150°C below the sintering temperature for 15 minutes to several hours and these conditions vary depending on the composition and grain structure of the sample.[66,67] The thermal etching process allows the diffusion of particles from boundary region, that is termodynamically weak due to polishing, towards the grains. Thus heat treatment provides a contrast between grain and grain boundary. In this thesis study, the thermal etching process was done at a temperature that is 100°C below the sintering temperature and for 1 hour.

2.2.5. Tranmission Electron Microscopy

In this project, the Transmission Electron Microscope (TEM) was used to check possible core-shell structure. and confirm the crystallographic symmetry using Selected Area Electron Diffraction (SAED).

This method is based on the interaction between the transmitted electrons through the sample and atoms. This interaction gives information about the crystal structure and the microstructural properties of the sample such as dislocations, grain and grain boundaries and domain structure in ferroelectrics. The speed and the wavelength of the electrons directly affect the image. For high quality images, fast electrons with shorter wavelength is preferred. The light areas in the image are the areas where more electrons pass through the sample whereas the dark ones are the dense areas of the sample. These differences give information about the feature of microstructure of the sample.

The TEM images contain series of spots and each spot has a diffraction condition with respect to crystal structure of the sample. SAED is used to identify phases and lattice parameters and also helpful for determination of structural growth. In this method, the thin strip of metal is located into TEM instrument to block the beam to obtain the diffraction information from the "selected" part of the sample. The interaction between the sample and a parallel beam that is travelling in one direction provide these information.

Sample preparation and Transmission Electron Microscopy (TEM) measurements of the samples was done by Dr. Aziz Genç at the ICREA Institute in Barcelona.

2.3. Electrical Characterization

In this section, the techniques used in the electrical measurements of the samples will be explained. The polished samples with 1 mm thickness and 10 mm diameter were coated with silver paste and subsequently fired at 135°C for 7 minutes to form the contants. During the electrical measurements, sample holder is filled with silicone oil to prevent the formation of electric arcs.

2.3.1. Dielectrıc Permittivity Measurements

The measurements of dielectric permittivity were performed with a Keysight E4980AL LCR meter on the unpoled samples. Dielectric measurements were done between 25-200°C. 1 V AC signal was applied at different frequencies (120 Hz, 1 kHZ, 10 kHz, 100 kHz). The sample is placed into sample holder and the temperature is controlled by the temperature controller of TF1000.

The LCR instruments that measure the inductance (L), capacitance (C) and resistance (R) of a circuit and therefor named as LCR meter. Definition of impedance is shown in Figure 2.5 to describe the working principle of LCR meter. The impedance has two parts as real (resistance,Rs) and imaginary (reactance,Xs) parts. Impedance can be defined in terms of Z and phase angle θ where Z=Rs+jXs. The reactance become as inductive or capacitive if the $\theta > 0$ or $\theta < 0$, respectively.

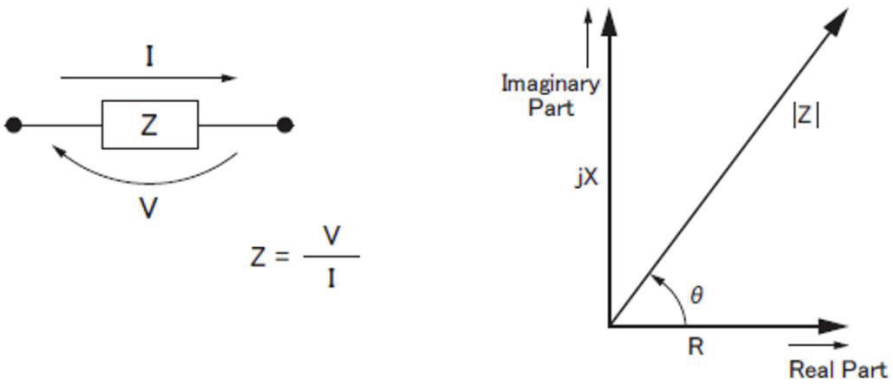

Figure 2.5. Definition of impedance.[68]

After the capacitance value is obtained, the following parallel plate capacitor equation (Equation 2.3) is used to calculate the dielectric constant of the materials.

$$\varepsilon_r = \frac{C * d}{A * \varepsilon_0} \tag{2.3}$$

ε_r is the dielectric constant of the sample, A is the area of the sample, d is the distance between the plates (thickness for our materials) and ε_0 is the permittivity of the space and is equal to 8.85×10^{-12} F/m.

2.3.2. Hysteresis Loop and Current-Voltage Measurements

In this study, polarization versus electric field (P-E) loops at different temperatures are used to determine the electrocaloric temperature change based on indirect method by using Maxwell relations.

P-E loops measurements were performed with an Aixacct TF Analyzer 1000 unit that is connected with a high-voltage amplifier (TREK Model 610E) which allows to apply up to 10 kV. The measurement frequency and the amplitude of the applied voltage affects the shape of the hysteresis loops and TF analyzer assists to observe the evalution of the loops.

The excitation signal to record a hysteresis loop consist of a prepol pulse and three bipolar excitation signals. The relaxation time is 1 second for each signal. The defined polarization states are identified by the prepol pulse and second pulse of the signals. The negative state of the remanent polarization is observed due to the prepol pulse while the

positive state is obtained by the second pulse. This condition is shown in Figure 2.6. The hysteresis loop starts with the negative remanent polarization (P_{rrel-}) and reaches to the positive saturation (P_{max+}) value with the first pulse of the first signal and then arrives to the positive remanent polarization (P_{r+}) state when the voltage is completely removed. Then the voltage is applied the reversed direction and negative saturation (P_{max-}) and the (P_{r-}) are observed, respectively. Due to the loss of polarization with respect to the time, this point is not same with the starting point. ($P_{rrel-} \neq P_{r-}$)

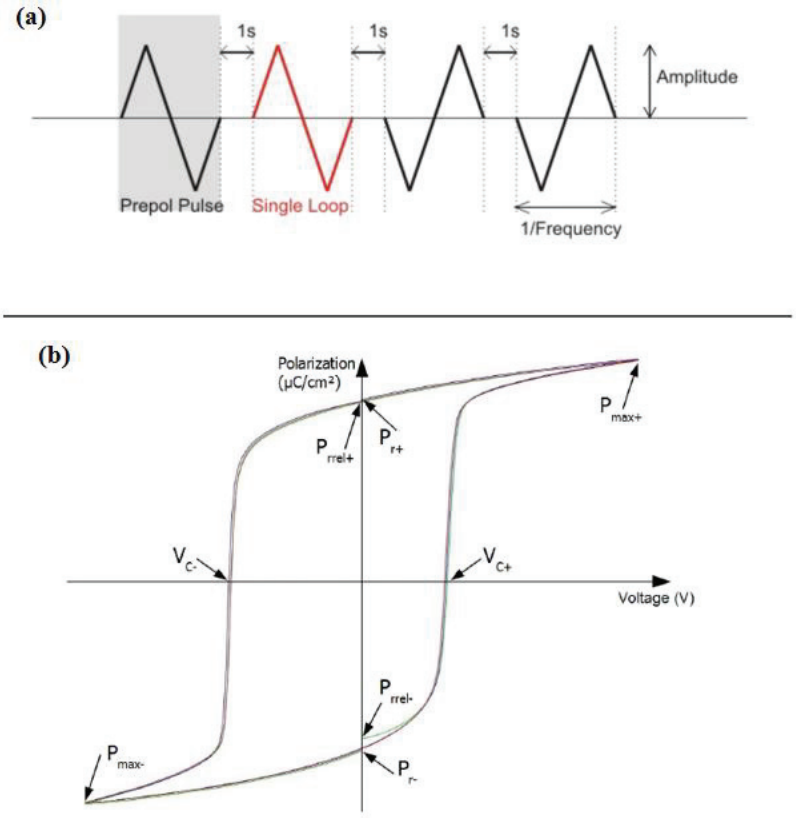

Figure 2.6. (a) The excitation signals (b) The hysteresis loops corresponding to the signals.[65]

During the polarization measurement process, sample holder is fulled with silicone oil to prevent electric arcs.

Current density versus electric field (I-E) data are obtained by using polarization hysteresis loops by differentiating the polarization with respect to the time and shown in Equation 2.4.

$$I = \int_{E_1}^{E_2} \left(\frac{\partial P}{\partial t}\right) dE \tag{2.4}$$

I-E curves show characteristic peaks depending on the polar/nonpolar nature of the sample and are helpful to probe the phase transitions and determine whether the phase has ferroelectric or antiferroelectric character.

2.3.3. Strain Measurements

In this study, strain-electric field measurements were used to differentiate the ferroelectric or antiferroelectric character of the samples. These measurements were performed with a MTI 2100 Photonic Sensor that integrated within the Radiant Precision LC ferroelectric property measurement system by Dr. Murat Avcı at the Prof. Dr. Ender Suvacı's laboratory of the Eskişehir Technical University.

As previously mentioned, ferroelectric ceramics also have a piezoelectric character, resulting in dimension change (displacement) of materials against the applied electric field. The strain versus electric field graphs were obtained for x=0.03 and 0.07 ceramics by using the Equation 2.5 and the displacement values obtained from measurement, and are shown in Figure 3.24.

$$\%\, strain = \frac{Displacement\ (\mu m)}{L\ or\ thickness\ of\ the\ pellets(mm) * 1000\ \ \mu m/mm} * 100 \tag{2.5}$$

The obtained strain values were converted to normalized strain coefficient (d_{33}* (pm/V)) values by using the Equation 2.6[69] where S_{max} and E_{max} are the maximum strain and electric field, respectively. The calculated d_{33}* values compared with the literature and listed in Table 3.4.

$$d_{33} * = {}^{S_{max}}/_{E_{max}} \tag{2.6}$$

CHAPTER 3

RESULTS AND DISCUSSION

3.1. Synthesis Route-I

In this section, the results obtained from materials synthesized by route-I will be discussed in details.

3.1.1. XRD Measurements

X-Ray diffraction patterns were collected after both the calcination and sintering processes.

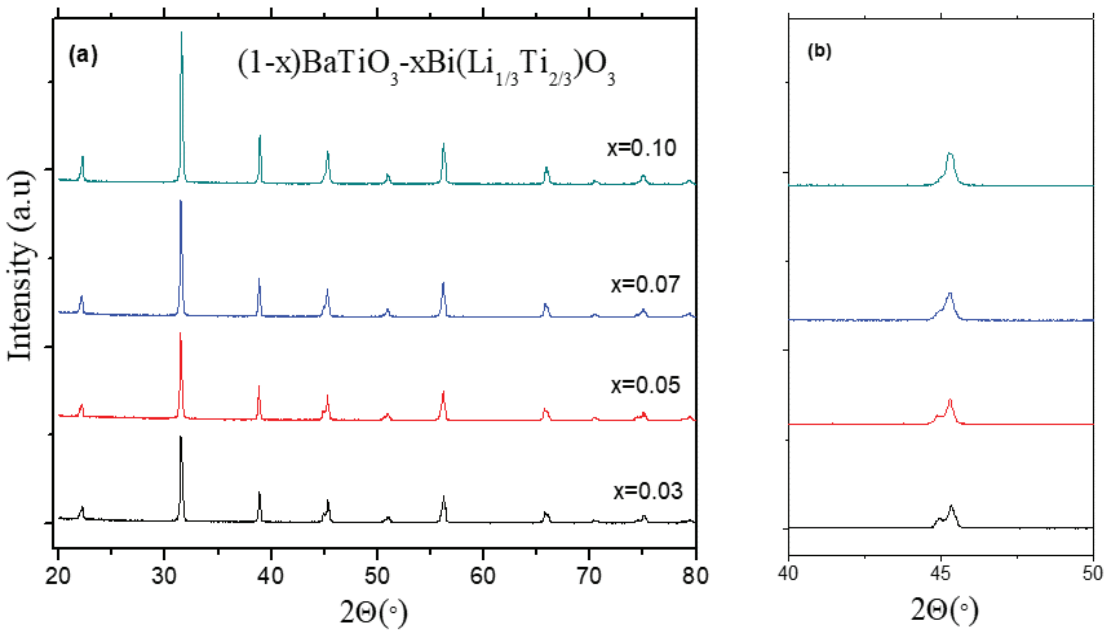

Figure 3.1. XRD patterns of all $(1-x)BaTiO_3-xBi(Li_{1/3}Ti_{2/3})O_3$ calcined samples in the range of 2Θ (a) from 20° to 80° and (b) 40° to 50.

Figure 3.1(a)-(b) shows the room temperature XRD patterns collected on calcined ceramics of different compositions in Figure 2.1. There are no extra peaks seen in XRD diffractogram after calcination and this shows that pure perovskite structure is formed.

Figure 3.1(b) shows the close examination of peak splitting at the 45°. For low BLT containing compositions splitting of the (002)/(200) peaks indicates tetragonal phase is already formed. Tetragonality decreases as the amount of BLT increases.

Figures 3.2 (a)-(b) indicate the XRD patterns of sintered samples. For x≤0.07 samples tetragonal peak splitting at 45°is quite sharp implying tetragonal symmetry and completion of the phase formation. x=0.03 and 0.05 samples have significant tetragonal peak splitting whereas the splitting is low for x=0.07. Different to the other compositions, x=0.10 sample shows orthorhombic splitting. As the $Bi(Li_{1/3}Ti_{2/3})O_3$ (BLT) content increases, the stability of the tetragonal phase decreases at room temperature. Thus, compositions containing a large amount of BLT (x>0.07) are no longer tetragonal but orthorhombic at room temperature. This symmetry change between the x=0.07 and 0.10 compositions suggests that there is a morphotropic phase boundary between these two compositions, and these results are consistent with the literature.[55]

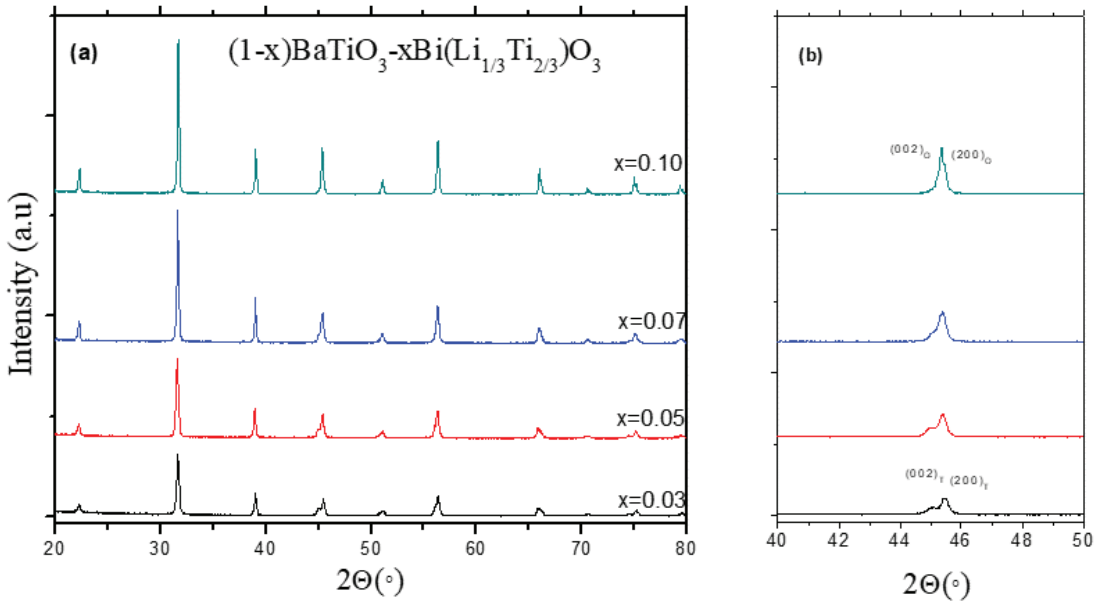

Figure 3.2. XRD patterns of all $(1-x)BaTiO_3-xBi(Li_{1/3}Ti_{2/3})O_3$ sintered samples in the range of 2Θ (a) from 20° to 80° and (b) 40° to 50.

3.1.2. Particle Size Analysis

The Dynamic Light Scattering (DLS) technique was used to analyze the particle size that is important for the sintering process.

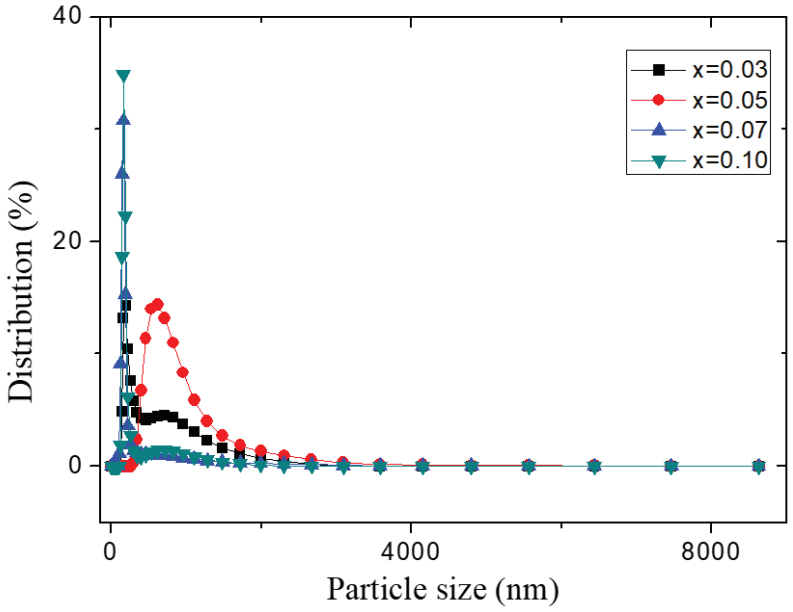

Figure 3.3. Particle size distribution of $(1-x)BaTiO_3-xBi(Li_{1/3}Ti_{2/3})O_3$ ceramics.

Figure 3.3 shows the particle size distribution of all compositions. The same particle distribution behavior was observed in all compositions and the powders before the sintering process have two different particle sizes as 200 and 700 nm. The particle with 200 nm size appears to be in the majority.

3.1.3. Density Measurements

The density of the ceramic samples were determined by Archimedes' principle and are listed in Table 3.1.

Table 3.1. Density of sintered samples measured by Archimedes' method.

x=0.10	***x=0.07***	***x=0.05***	***x=0.03***
5.76 g/cm^3 *93%*	*5.27 g/cm^3* *86%*	*4.57 g/cm^3* *75%*	*4.07 g/cm^3* *67%*

Percent theoretical densities of the samples were calculated using tetragonal (P4mm) $BaTiO_3$ with the reference number 01-079-2265. As can be seen, the densities of the x = 0.03 and 0.05 compositions are quite low. Some of the most important factors affecting the density are particle size and sintering temperature. The sintering temperature

is 1200°C for all compositions and the particle sizes of the samples are similar as seen above (Figure 3.3). The density difference between the samples might be caused by the BLT content. In the literature, most commonly used compounds as sintering aid in the liquid phase sintering process is Bi_2O_3 and Li_2CO_3 [70–73] due to their low melting points (817°C and 723°C, respectively). Therefore, the densities of compositions containing high amounts of BLT (x=0.10 and x=0.07) are higher than the other compositions (x=0.05 and x=0.03).

3.1.4. Hysteresis Loop Measurements

The hysteresis loops were measured at different temperatures for each composition to calculate the ECE based on the indirect method by using Aixacct TF1000 device. Hysteresis loops are shown in Figure 3.4 (a)-(d).

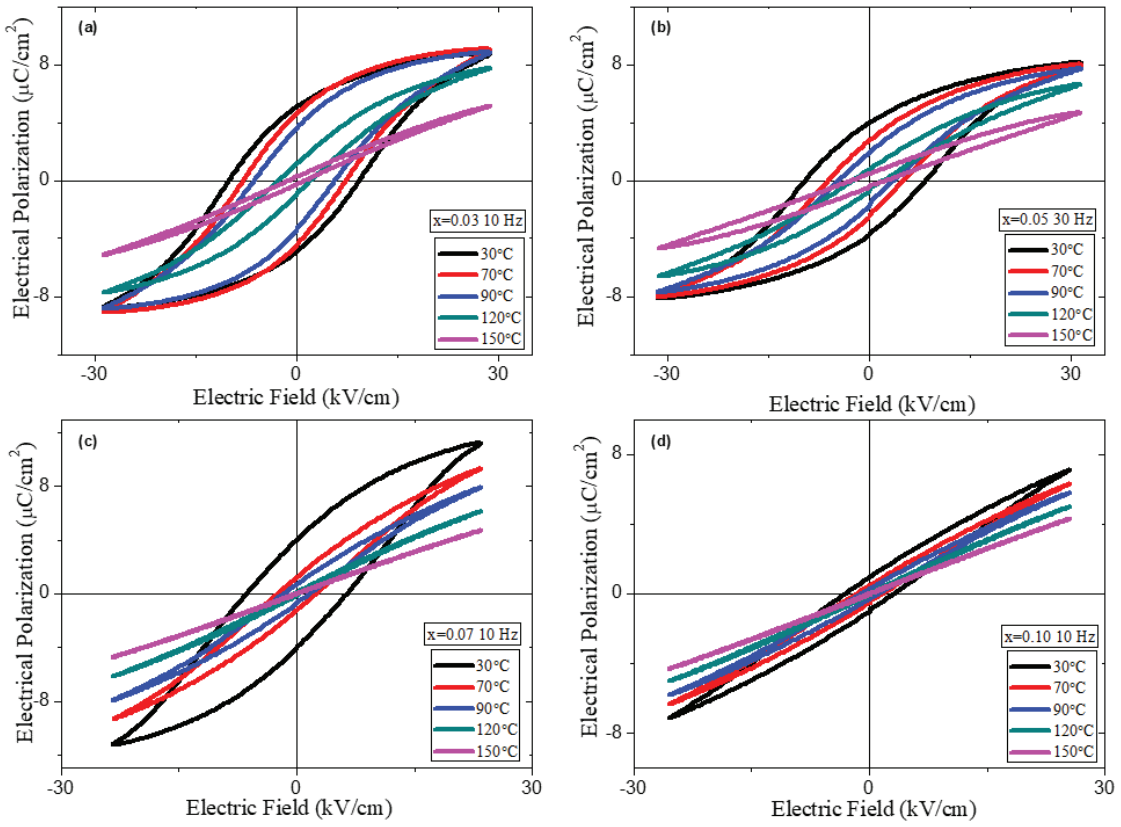

Figure 3.4. (a)-(d) Polarization hysteresis loops of all $(1-x)BaTiO_3-xBi(Li_{1/3}Ti_{2/3})O_3$ ceramics measured at different temperatures.

Saturated hysteresis loops were obtained for the samples x=0.03 and 0.05. In the case of x=0.07, the polarization value shows a faster decrease compared to the other compositions. It is predicted that this rapid drop can cause an extra peak in the electrocaloric effect of this composition. Furthermore, it is clear that the hysteresis loops becomes slimmer as the amount of BLT increases at 30°C. x=0.10 composition exhibits relaxor ferroelectric hysteresis behavior with low remanent polarization and low coercive field values.

The coercive field, E_c and remanent polarization, P_r decreased as the temperature is increased for all compositions as can be seen in Figure 3.4 (a)-(d). This is the behavior of the general ferroelectric materials. Because as the temperature increases, the sensitivity of the dipoles to the electric field increases and the material becomes easier to polarize with a lower electric field, which implies the reduction of the coercive field.[74]

3.1.5. Electrocaloric Effect Calculations

The temperature-dependent hysteresis behavior was used to calculate the electrocaloric effect of the ceramic samples indirectly by extracting the polarization values corresponding to each temperature from the loops.

The polarization versus temperature graphs obtained from the hysteresis loop measurements are shown in Figure 3.5(a)-(d) for all the compositions under various electric fields. P(T) data are used to determine the electrocaloric effect indirectly. Obviously, high polarization values were obtained in all compositions under high electric field. It is clear that the increasing electric field leads to shifting of the polarization to the higher temperatures for all compositions. Similar behavior has been reported by other studies.[35,75,76]

The electrical polarization decreases with increasing temperature. The orientation polarization of the permanent dipoles of ferroelectric materials decreases with increasing temperature due to randomization effect of the temperature. However, the polarization starts to increase as the temperature increases for x=0.03 composition in Figure 3.5(a) that brings the negative electrocaloric effect (ECE) as is seen from Figure 3.7(a).

Polarization temperature P(T) curves were fitted with a sixth order polynomial equation to obtain $\partial P/\partial T$ and are shown in Figure 3.6(a)-(d) for only 22 kV/cm. The degree of polynomial equation was chosen according to best representation of the

polarization-temperature curves. The electrocaloric temperature change (ΔT) is determined by using these curves obtained from the upper branches of the hysteresis loops for both numerical differentiation (Equation 3.1) and fitting method based on the Maxwell relations$(\delta P/\delta T)_E = (\delta S/\delta E)_T$.[77]

$$(\frac{\partial P}{\partial T})_E = \frac{1}{2} * \left(\frac{P_n - P_{n-1}}{T_n - T_{n-1}} + \frac{P_{n+1} - P_n}{T_{n+1} - T_n}\right) \tag{3.1}$$

$$\Delta T = -\frac{T}{\rho C_p} \int_{E_1}^{E_2} \left(\frac{\partial P}{\partial T}\right)_E dE \tag{3.2}$$

Equation 3.2 represents the adiabatic temperature change formula, where E_1 and E_2 are the initial and final applied electric field, respectively. C_p is the specific heat capacity of material which is accepted as an average value of 0.50 J/g.K based on $BaTiO_3$-based studies in the literature[33,78–80] for all calculations and ρ symbolizes the measured density of the ceramics.

ΔT-T curves calculated using equation 3.2 (Figure 3.6(a)-(d)) at different electric fields are shown in Figure 3.7(a)-(d). These calculations are checked by comparing with the numerical differentiation method (the right part of the Figure 3.7(a)-(d)) for 22 kV/cm. The two methods are in good agreement with each other which indicates that P-T curve fits are sensible. Fitting of P-T curve becomes easier as the polarization changes more slowly with temperature as the amount of BLT increases. The purpose of using both numerical and fitting methods in calculating the electrocaloric effect is to check the extra peaks that may arise from the imperfect fitting.

It can be seen from the Figure 3.7(a)-(d), as the electric field increases, ΔT increases and the ΔT peaks shifts to the higher temperature under the electric field.

The highest electrocaloric response of the material is obtained at the phase transition temperature. It can be seen in Figure 3.7(a)-(d) that all compositions have a ΔT peak which does not change with the composition which occurs approximately at the phase transition temperature (T_{FE-PE} = 123°C) of undoped $BaTiO_3$. However the amplitude of the ΔT peaks decrease with increasing BLT content. Such peaks which does not change with composition might have been caused by core-shell microstructure. Core-shell microstructure was introduced earlier in section 1.5. The core-shell microstructure, which is proven in the literature[55], causes a dielectric anomaly that belongs to the core

and this anomaly's temperature does not change depending on the composition. Therefore, it is thought that the unchanged ΔT peak in all compositions might belong to the core. Moreover, an extra peak can be observed in ΔT versus T graphs of x=0.07 composition (Figure 3.7(a)-(c)) and it is thought that it may correspond to the shell contribution.

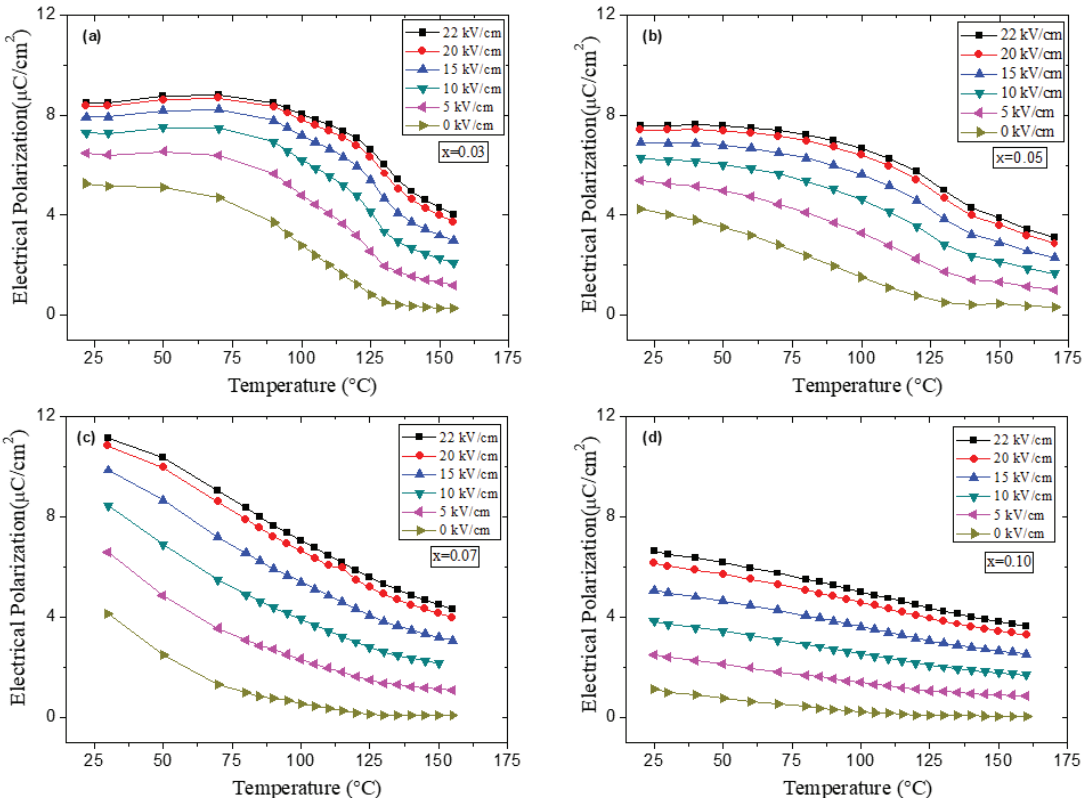

Figure 3.5. (a)-(d) Polarization versus temperature graphs of all (1-x)$BaTiO_3$ - x$Bi(Li_{1/3}Ti_{2/3})O_3$ ceramics measured under different electric fields for (a)x=0.03, (b)x=0.05, (c)x=0.07, (d)x=0.10.

As mentioned previously, a negative electrocaloric effect resulting from the increase in polarization in the x=0.03 ceramic, was obtained and is shown in Figure 3.7 (a). There is no physical basis for this effect.

Figure 3.8(a)-(b) shows the electrocaloric temperature change of all ceramics with respect to the composition obtained from both fitting and numeric differentiaton methods at 22 kV/cm. The obtained electrocaloric behavior are the same for these two methods showing the quality of the fits. As the amount of BLT increases, ΔT peak value decreases. The structural changes in the $BaTiO_3$ with the increasing amount of dopants also changes

the phase transition character and the first-order phase transition of $BaTiO_3$ becomes diffuse phase transition. This means the change of the polarization with temperature become less sharp around the phase transition temperature. Therefore, the decrease of the ΔT value with BLT content is expected.

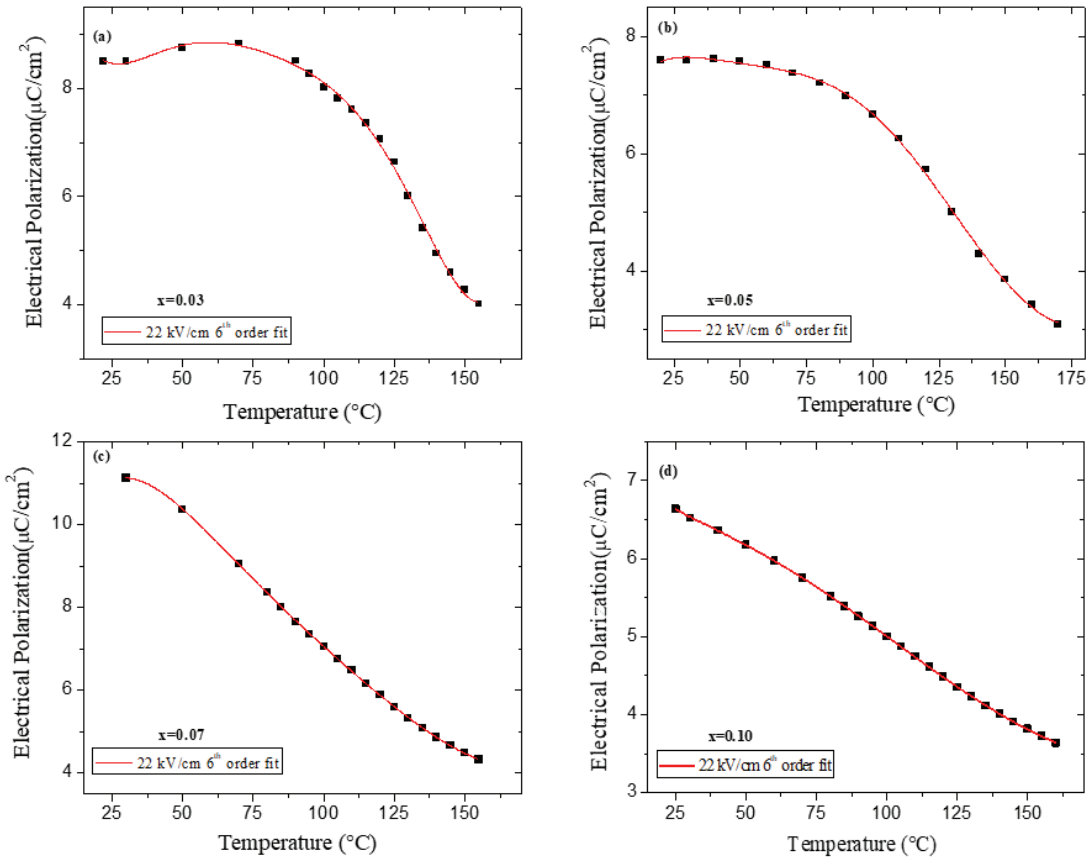

Figure 3.6. (a)-(d) Polarization versus temperature graphs fitted with a 6th order polynomial of all $(1-x)BaTiO_3-xBi(Li_{1/3}Ti_{2/3})O_3$ ceramics measured at 22 kV/cm for (a) x=0.03, (b) x=0.05, (c) x=0.07, (d) x=0.10.

Core-shell structure which might be responsible from the electrocaloric behavior may result from slow sintering kinetics. As mentioned before, particle size affect the sintering kinetics. When the kinetics of diffusion and sintering is not sufficient to incorporate the dopant atom in the host structure as explained in section 1.5, the core-shell microstructure is observed. In the literature, the core-shell structure is common in BT-$Bi(X)TiO_3$ solid solutions[56,57] due to the restricted sintering temperature to prevent the loss of volatile precursor in the solid solution such as Li_2CO_3 and Bi_2O_3.

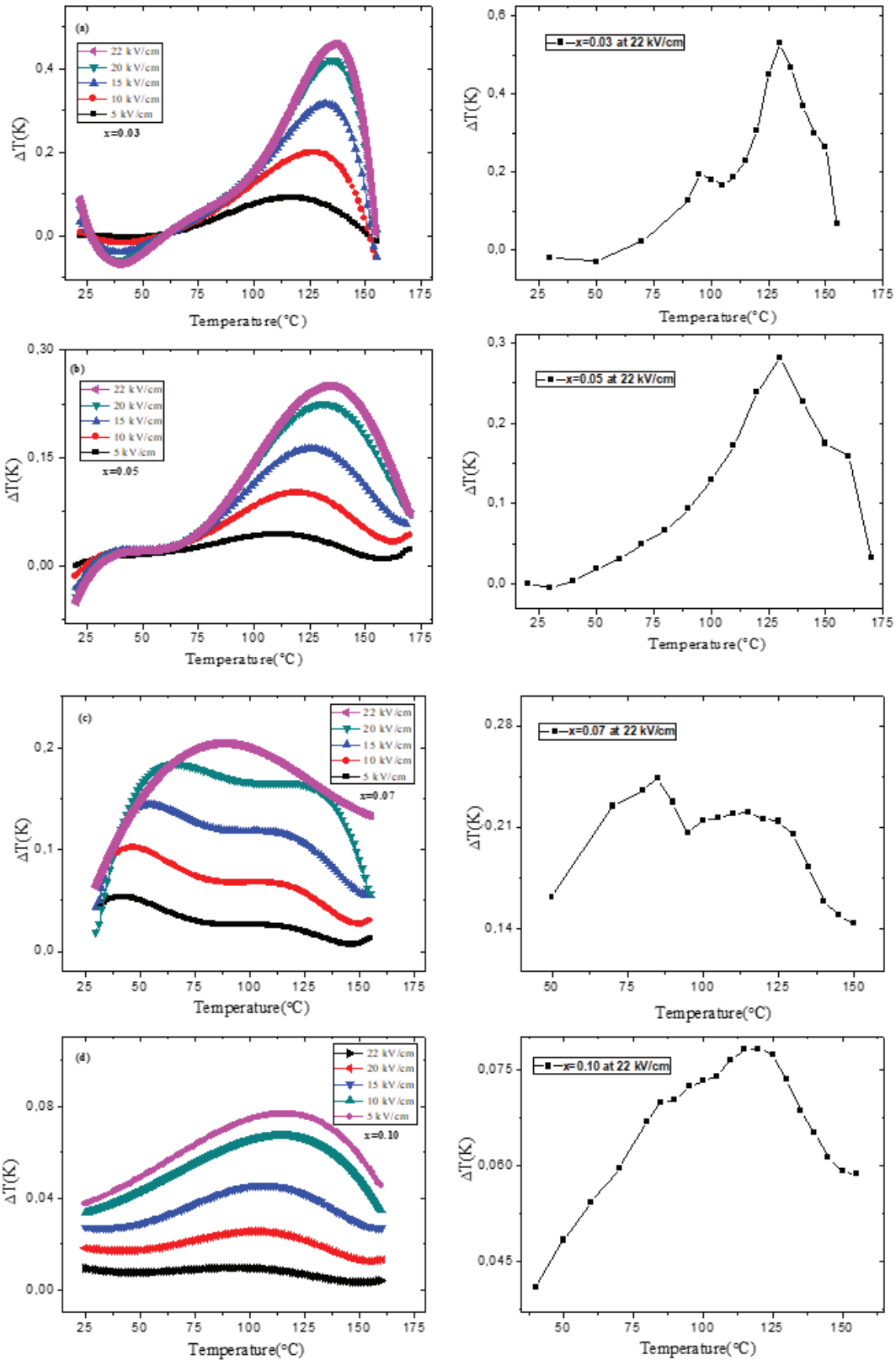

Figure 3.7. Temperature dependence of ΔT of all (1-x)$BaTiO_3$-x$Bi(Li_{1/3}Ti_{2/3})O_3$ ceramics calculated at different electric field for both fitting (left) and numerical (right) differentiation method for (a)x=0.03, (b)x=0.05, (c)x=0.07, (d)x=0.10.

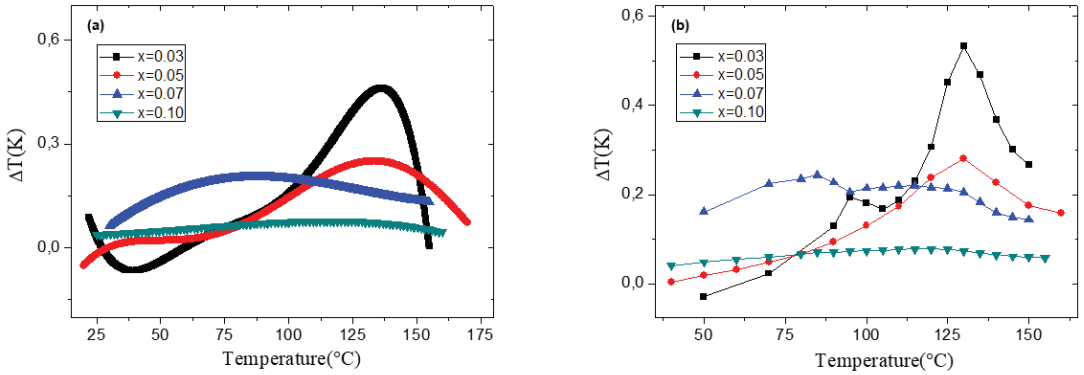

Figure 3.8. Temperature dependence of ΔT of all (1-x)$BaTiO_3$-x$Bi(Li_{1/3}Ti_{2/3})O_3$ ceramics measured at 22 kV/cm for (a) fitting method and (b) numerical differentiation.

3.1.6. Dielectric Measurements

Dielectric properties of ceramic samples were measured with LCR meter and shown in Figure 3.9 (a)-(d) with dielectric loss as a function of temperature.

In the literature, there are two anomalies related to core and shell in the dielectric behaviors of ceramic materials having core-shell structure. While the dielectric anomaly of the core remains at the same temperature for all the compositions, the anomaly belonging to the shell is seen at different temperatures depending on the frequency and composition.[55–57,81,82]

In Figure 3.9(a)-(c) there is an anomaly in $0.03 \leq x \leq 0.07$ samples corresponding to the ferroelectric-paraelectric phase transition around the Curie temperature, Tc. No secondary anomaly is seen and the frequency dependence is very low in these samples. Despite the symmetry change in XRD, the unchanging dielectric anomaly at the same temperature for all compositions shows us that there may be a core structure. However, in the case of x = 0.10 sample, there is an anomaly at lower temperature in addition to the anomaly in Tc. The frequency dependence is clearly evident in the general behavior of this sample. This is due to the fact that, after certain amounts of dopants, the long range order of ferroelectric materials is distorted, the material becomes a relaxor ferroelectric.[3] The fingerprint of the relaxor property is the shift of the dielectric anomaly through the lower temperature depending on the frequency.[6,83] The fact that the dielectric behavior of x = 0.10 sample is thought to be caused by the relaxor feature and this behavior consistent with hysteresis loop character of this composition. Moreover, the possible shell formation may be responsible for the anomaly at lower temperature.

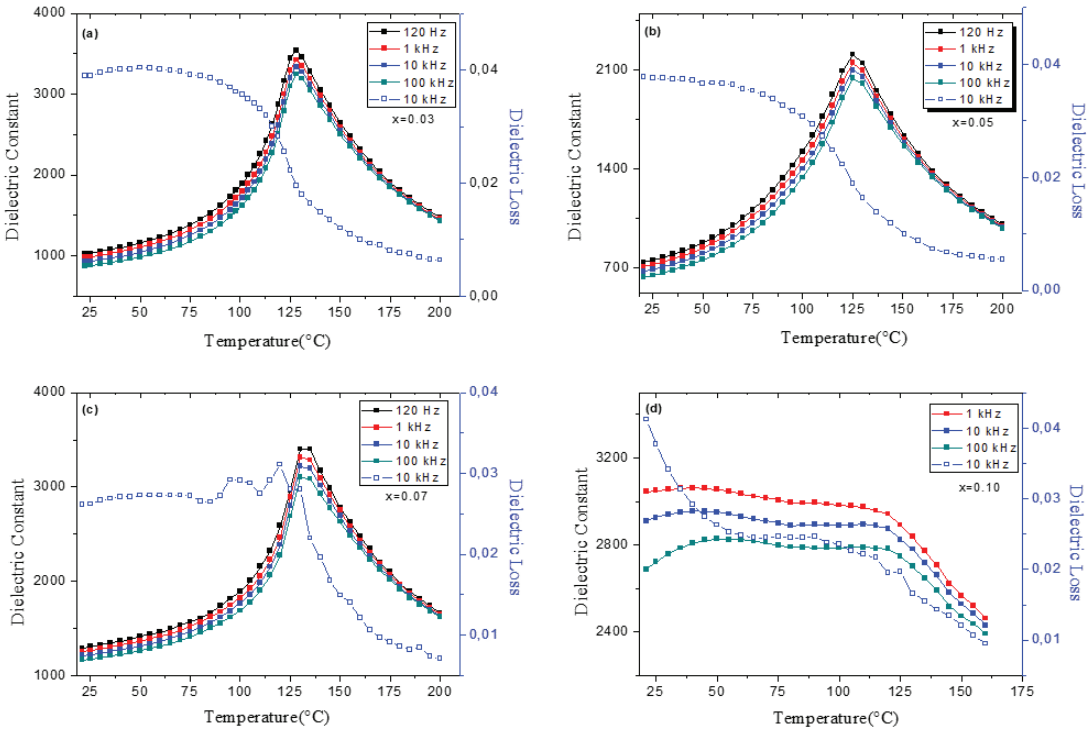

Figure 3.9. Temperature dependence of dielectric constant ε_r and dielectric loss of all $(1-x)BaTiO_3- xBi(Li_{1/3}Ti_{2/3})O_3$ ceramics at different frequencies.

The dielectric behavior of the samples are different from the Ma et al.[55] where the shell contribution is increasingly seen as the BLT amount increase. This difference is thought to depend on the synthesis conditions. Depending on the particle size the sintering kinetics is affected, the amount of more/less BLT diffusing into the core may alter the core-shell microstructure and thus causes the difference in dielectric behavior.

The peak seen in the dielectric constant at the phase transition temperature of all samples is also present in the dielectric loss behavior. Two anomalies are also observed in dielectric loss of x=0.10 composition.

3.1.7. Microstructural Analysis

Microstructure analyzes (TEM studies) were done for the determination of core-shell structure as mentioned above. x=0.07 sample is used for this analysis and the TEM micrographs of the sample is shown in Figure 3.10. The general features of the ceramic sample is illustrated in (a)-(c) and the following figures (d)-(e) are HRTEM micrographs obtained from Figure 3.10(a) from the red and green square region. Figure 3.10(d) shows

the HRTEM micrograph obtained from the red squared area, revealing the presence of a domain-like defected area continued till the grain boundary. In the middle, detailed HRTEM micrograph of the indicated region is shown where it the defects are quite clearly visible. FFT (Fast Fourier Transform) pattern obtained from this micrograph revealed that this grain is composed of tetragonal $BaTiO_3$ phase with the space group P4mm with lattice parameters of a= 0.3999 nm and c= 0.4017 nm. It is visualized along its [211] zone axis.

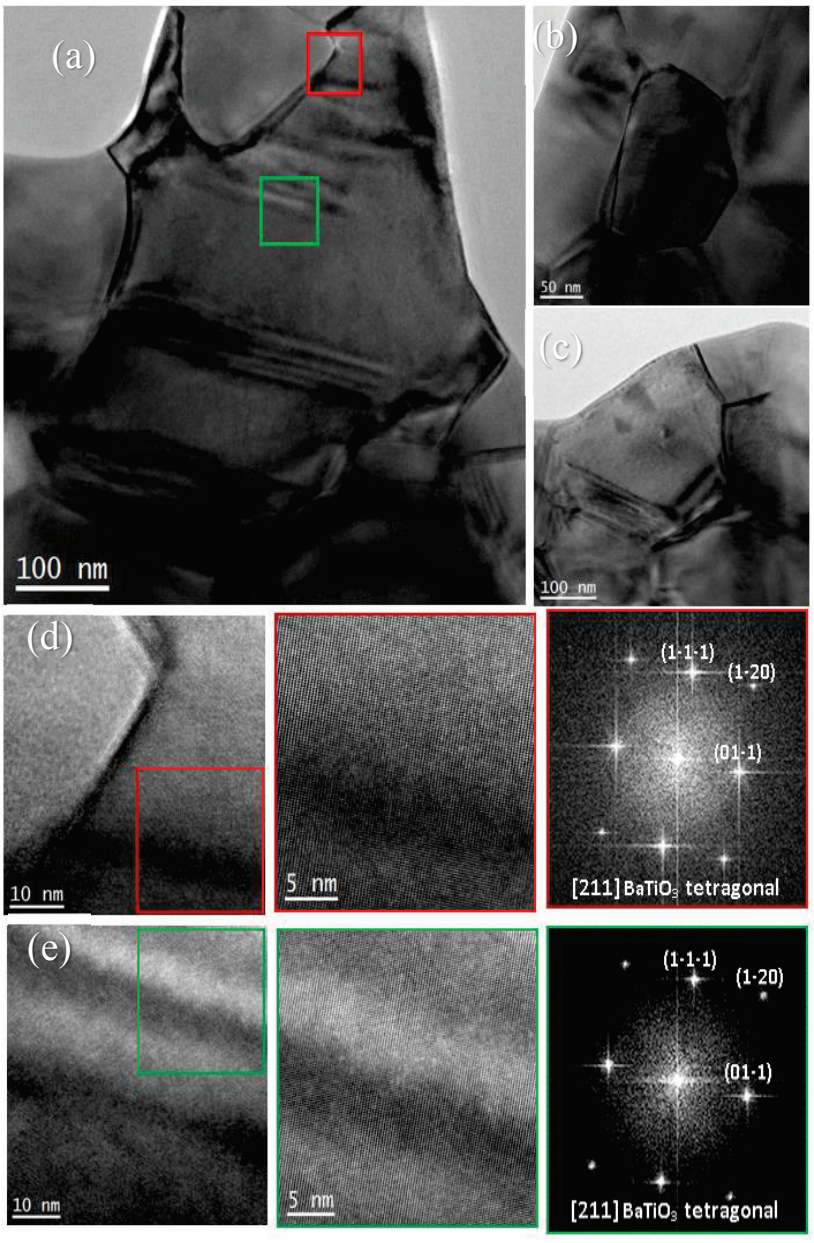

Figure 3.10. (a)-(c) Selection of low magnification TEM micrographs and (d) and (e) selected area electron diffraction patterns of $(1-x)BaTiO_3-xBi(Li_{1/3}Ti_{2/3})O_3$ for x=0.07.

The green squared area in Figure 3.10(e), reveals similar features as the region shown in Figure 3.10(d). These domain-like regions contain many defects however all of the grains are identified as the same tetragonal $BaTiO_3$ phase.

In conclusion, the shell contribution of the dielectric behavior of the x=0.07 ceramic could not be seen clearly.

3.2. Synthesis Route-II

It was aimed to improve the synthesis conditions in order to get rid of the core-shell structure and to densify the samples. The ball milling was effectively used to synthesize the samples and ball milling parameters (ball to powder ratios, grinding steps and milling times) were changed for this purpose. Thus homogeneous and single particle size (smaller than that obtained from synthesis route-I) was obtained.

3.2.1. XRD Measurements

XRD measurements were carried out after each heat treatment (i.e. calcination and sintering) of ceramic samples and shown in Figures 3.11 and 3.12, respectively.

Figure 3.11(a)-(b) shows the room temperature XRD patterns performed on calcined BT-BLT ceramics of different compositions. All samples show pure perovskite structure. It is clear that peak splitting is not sharp when examined closely (Figure 3.11(b)).

The sintering was done to stabilize the phase after calcination and to obtain a dense ceramic and Figure 3.12(a) demonstrates the sintered samples' XRD patterns. All ceramic samples exhibit pure perovskite structure and no secondary phases were observed. This is a sign for complete diffusion of all $Bi(Li_{1/3}Ti_{2/3})O_3$ into the $BaTiO_3$ lattice and solid solution formation. Figure 3.12(b) shows the close examination of the 2θ range between 40°-50° that indicates the strong $(002)_T/(200)_T$ peak splitting of the ceramics with $x<0.07$, consistent with tetragonal symmetry whereas for x=0.08 is stabilized in the orthorhombic symmetry of the $BaTiO_3$ with $(002)_O/(200)_O$ peak splitting.[55] The peak positions for the samples $0.03\leq x\leq 0.05$ are almost the same. The amount of BLT content between these three compositions is close to each other and

similar peak position in XRD patterns may be due to fact that the difference between the amount of dopant is too small to cause a significant shifting.

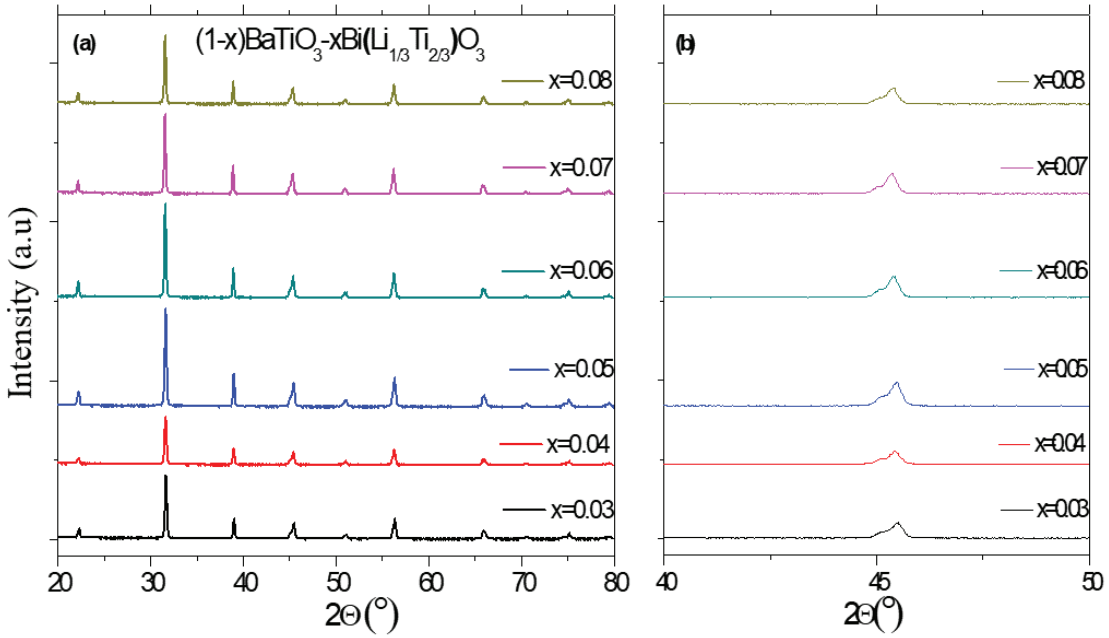

Figure 3.11. XRD patterns of all $(1-x)BaTiO_3-xBi(Li_{1/3}Ti_{2/3})O_3$ calcined samples between (a) 20° to 80° and (b) 40° to 50°.

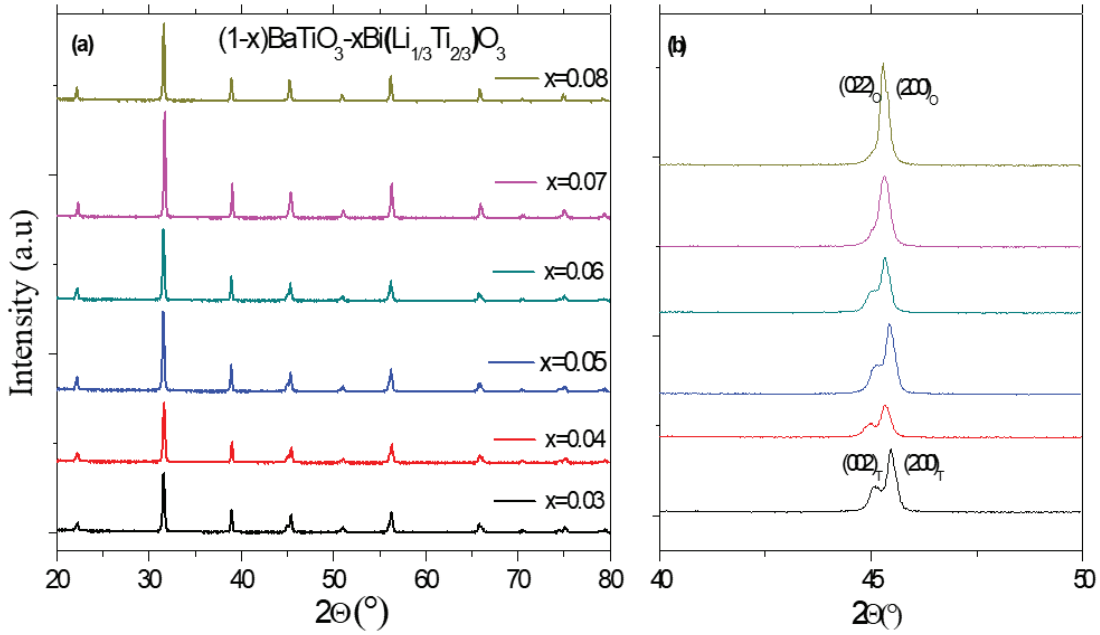

Figure 3.12. XRD patterns of all $(1-x)BaTiO_3-xBi(Li_{1/3}Ti_{2/3})O_3$ sintered samples between (a) 20° to 80° and (b) 40° to 50°.

With increase of the BLT substitution, it can be clearly seen that the peak around 46° shifts towards lower angles. The shifting is explained by the change in unit cell parameters causes due to the diffusion of BLT.

3.2.2. Microstructural Analysis

Further studies on microstructures were carried out by Tranmission Electron Microscopy (TEM) and Scanning Electron Microscopy (SEM). The TEM micrographs and the corresponding selected area electron diffraction (SAED) patterns are shown in Figure 3.13(a)-(g). As can be seen in these micrographs (Figure 3.13(a)-(c)), the grains of the sample, which are around 200 nm and 600 nm in size, are full of domain-like regions. The presence of some defects are also visible in Figure 3.13(c) micrographs. In order to investigate the presence of different phases within defects (Figıre 3.13(d)-(e)) and domain regions, (Figure 3.13(f)-(g)) SAED was performed in both two regions. It reveals that both are composed of the same tetragonal $BaTiO_3$ phase.

After TEM studies, the grain size and the morphology of sintered ceramics were analyzed with the help of SEM and SEM micrographs are shown in Figure 3.14(a)-(f). The magnification of BS images is 30.000 except for 3.14(b) where the magnification equals to 20.000. For all compositions, the ceramics has high density with no intragranular and intergranular pores. At low magnifications, it was observed that there are impurity phases at the grain boundaries and inside the grains as shown in Figure 3.15(a)-(f) with the BS images with the magnification of 10000.

For the determination of the impurity phases, EDX has been tried and no definite information about the impurity phase composition has been reached due to the overlapping of the X-Ray energy values of the Ba^{2+} ($L_{\alpha 1}$= 4.466 and $L_{\beta 1}$= 4.828) and Ti^{4+} ($K_{\alpha 1}$= 4.512 and $K_{\beta 1}$= 4.933)[84] elements and the inability of the Li^{+} element to be determined by EDX. Nevertheless, EDX analysis shows that the impurity phase contains low amount of Bismuth. It is thought that the impurity phase which also cannot be determined in XRD results is small and does not affect electrical measurements.

The grain size analysis is also performed using SEM micrograph. The results are consistent with TEM and the average grain size of all ceramics is close to each other and between 200 and 700 nm. A typical micrograph of x=0.06 composition is shown in Figure 3.16.

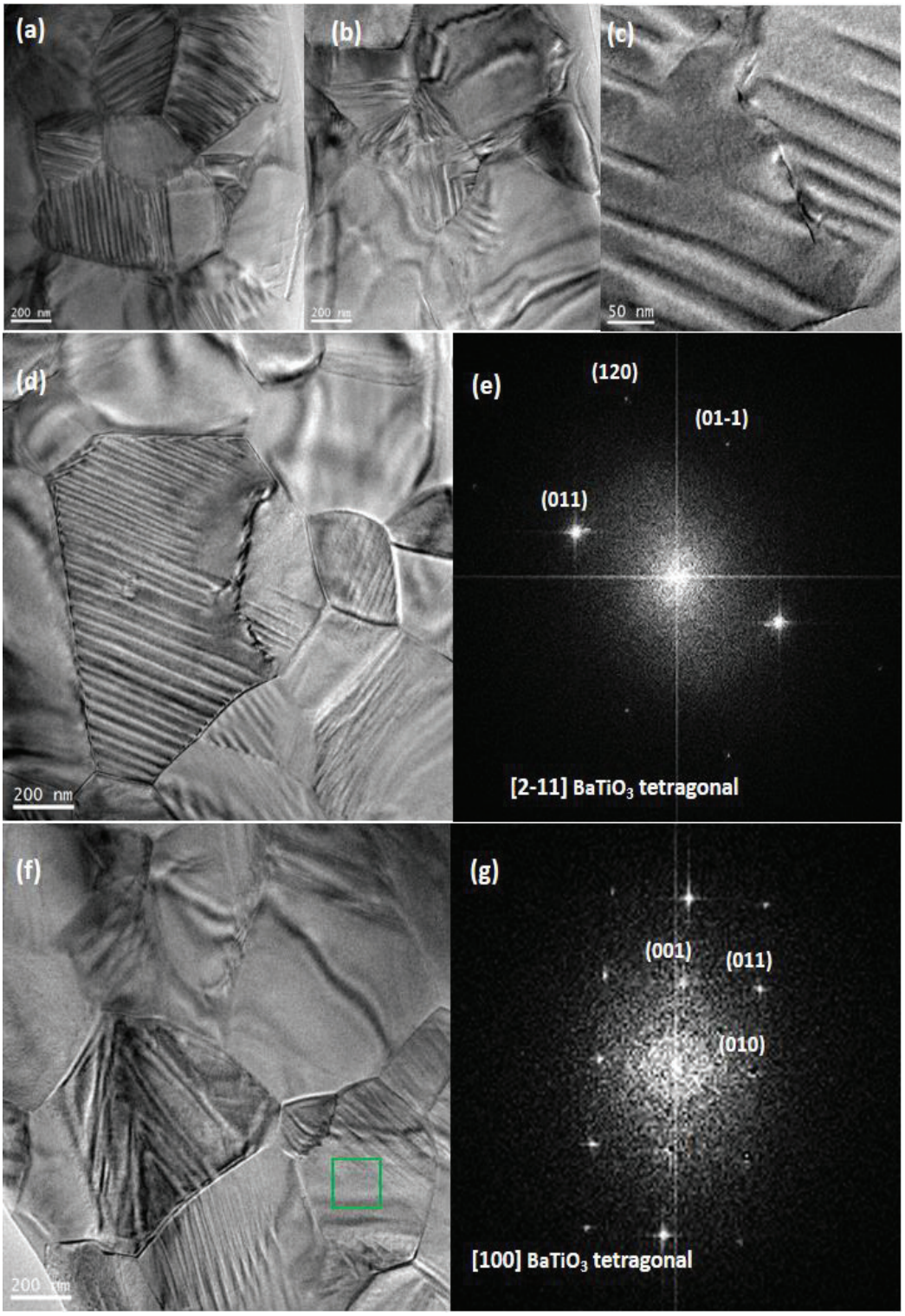

Figure 3.13. (a)-(d) and (f) Selection of high magnification TEM micrographs and (e) and (g) selected area electron diffraction patterns of $(1-x)BaTiO_3-xBi(Li_{1/3}Ti_{2/3})O_3$ for x=0.05.

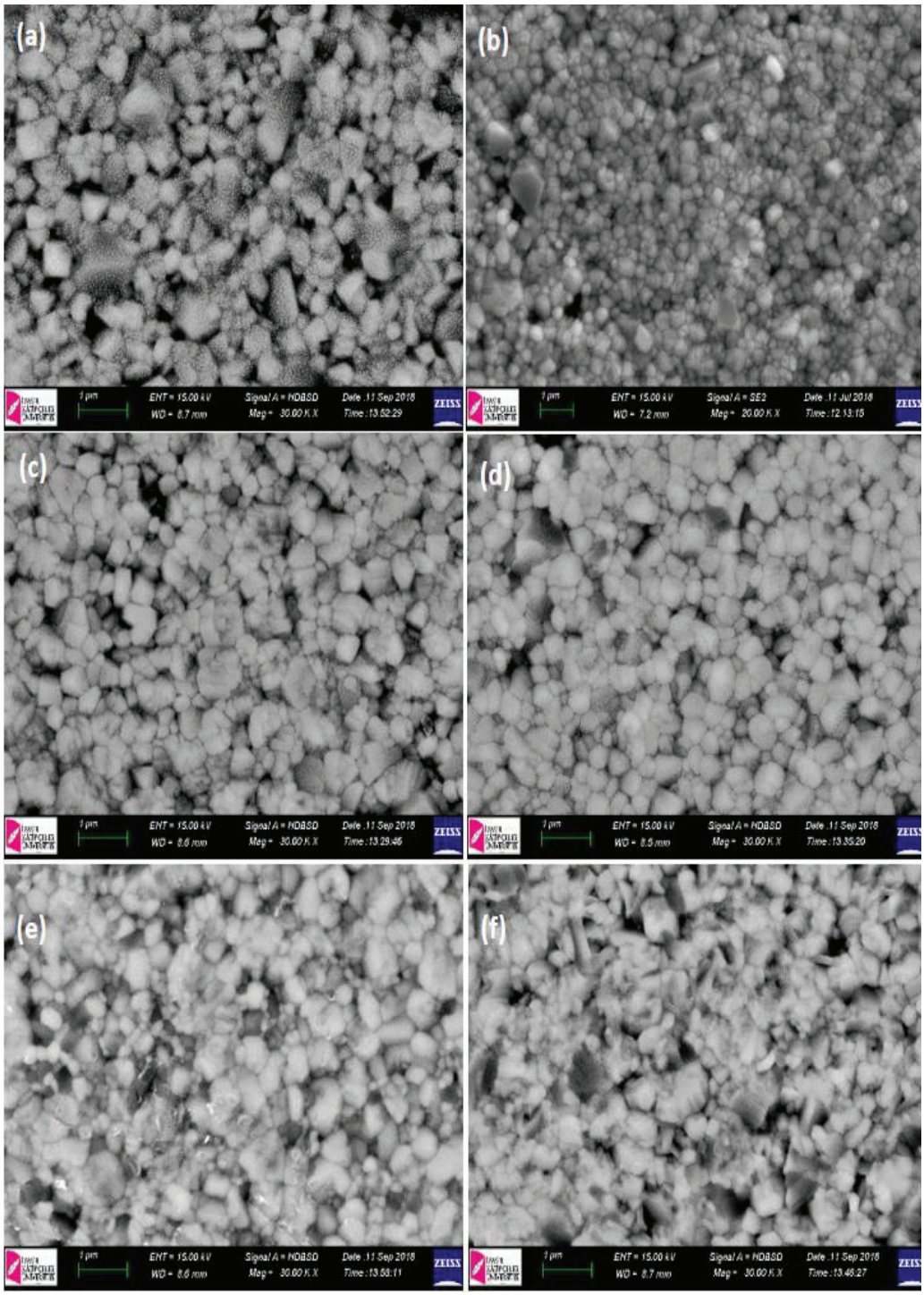

Figure 3.14. (a)-(f) SEM micrographs of all $(1-x)BaTiO_3-xBi(Li_{1/3}Ti_{2/3})O_3$ ceramics for (a)x=0.03, (b)x=0.04, (c)x=0.05, (d)x=0.06, (e)x=0.07,(d)x=0.08.

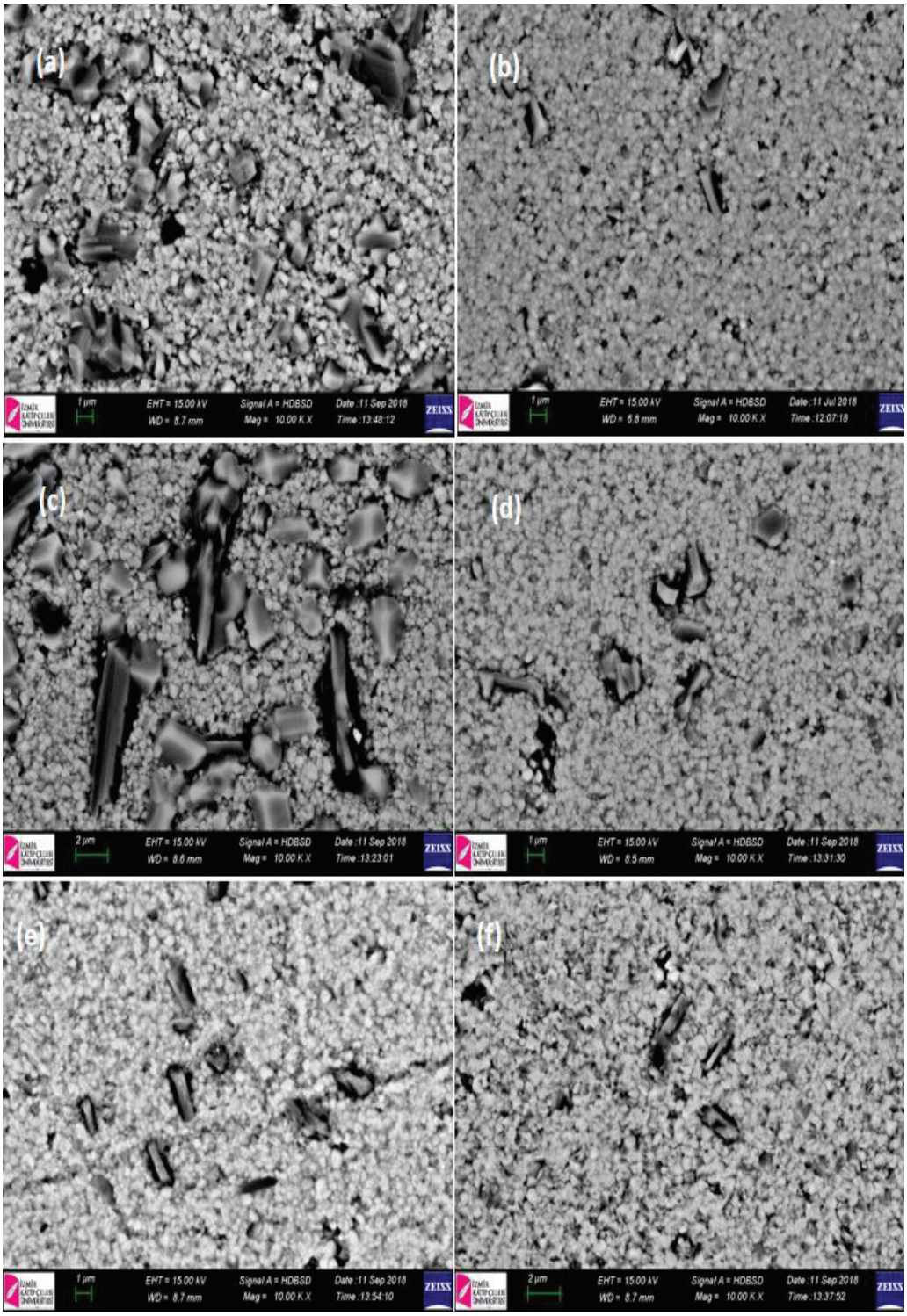

Figure 3.15. (a)-(f) SEM micrographs of all $(1-x)BaTiO_3-xBi(Li_{1/3}Ti_{2/3})O_3$ ceramics with the presence of secondary phases for (a)x=0.03, (b)x=0.04, (c)x=0.05, (d)x=0.06, (e)x=0.07, (f)x=0.08.

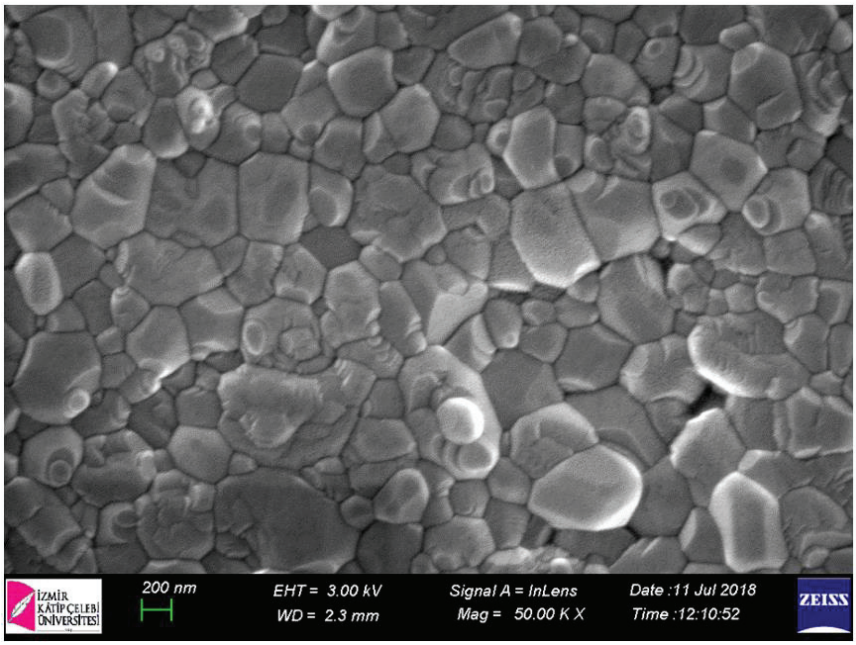

Figure 3.16. SEM image of $(1-x)BaTiO_3- xBi(Li_{1/3}Ti_{2/3})O_3$ (x=0.06).

3.2.3. Density Measurements and Particle Size Analysis

After the microstructural analysis, density of sintered ceramic samples are determined by using Archimedes' method and the values are shown in Table 3.2.

Table 3.2. Density of sintered samples measured by Archimedes' method.

x=0.08	***x=0.07***	***x=0.06***	***x=0.05***	***x=0.04***	***x=0.03***
5.71 g/cm^3 (1200°C)	*5.73 g/cm^3 (1200°C)*	*5.66 g/cm^3 (1225°C)*	*5.63 g/cm^3 (1225°C)*	*5.65 g/cm^3 (1250°C)*	*5.65 g/cm^3 (1250°C)*

The density values given in Table 3.2 are higher than 93% of the theoretical density calculated using $BaTiO_3$ with tetragonal symmetry (space group P4mm) (reference number 01-079-2265). Although ceramic materials were sintered at similar temperatures compared to materials synthesized following synthesis route-I, high density ceramics were obtained due to lower particle sizes obtained in route-II. The lower particle size is the result of modified ball milling conditions. Due to the low particle size, there will be less Bi^{3+} and Li^{+} evaporation as there is no need to increase the sintering temperature to densify the samples.

Figure 3.17 shows the particle size analysis of selected compositions of $(1-x)BaTiO_3-xBi(Li_{1/3}Ti_{2/3})O_3$ ceramics before the sintering process. The average particle size is smaller than 200 nm for all compositions, which facilitates the diffusion. The easier diffusion leads to more dense ceramics.

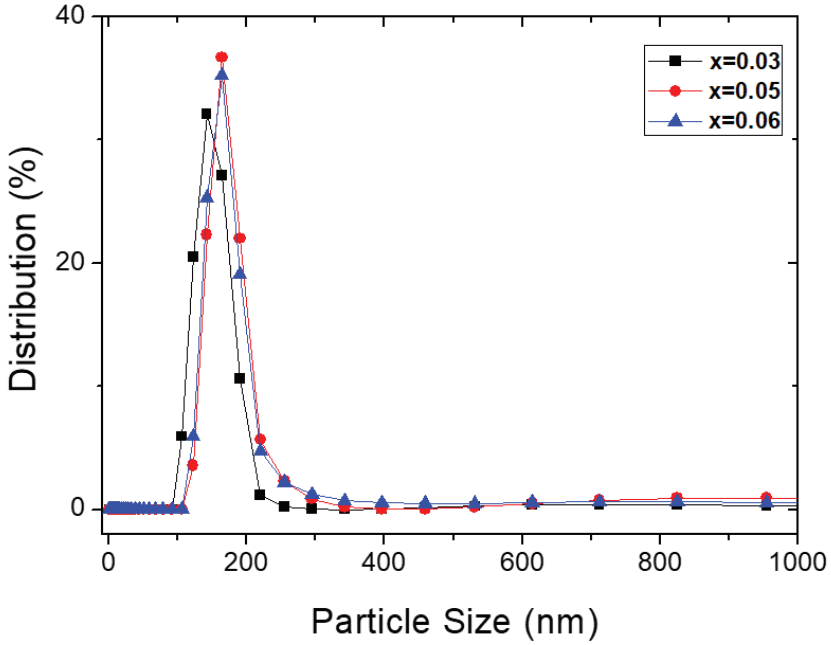

Figure 3.17. Particle size distribution of selected compositions before the sintering process.

3.2.4. Dielectric Measurements

Figure 3.18(a)-(f). shows the dielectric constant of different compositions of all $(1-x)BaTiO_3-xBi(Li_{1/3}Ti_{2/3})O_3$ samples over a broad temperature range between 25°-200°C at different frequencies of 120 Hz, 1 kHz, 10 kHz and 100 kHz. Two anomalies can be defined in dielectric constant-temperature graph, whose temperatures are named as depolarization temperature (T_d) and Curie temperature (T_c). T_d is the depolarization temperature which corresponds to the transition from a ferroelectric phase to so-called antiferroelectric phase.

The existence of FE-AFE phase transition will be explained in detail in the hysteresis loop measurement. T_d is determined by several different methods such as identifying the steepest decrease of remanent polarization, using thermally stimulated

depolarization current (TDSC), from dielectric constant versus temperature (ε_r-T) graph, and dielectric loss versus temperature (tanδ-T) behavior.[85]

In this study, the depolarization temperature (T_d) of different ceramics are determined with the help of dielectric constant versus temperature graph (Under each graph in Figure 3.18 (a)-(f), $1/\varepsilon_r$ versus temperature graphs are shown.) from the first anomaly.[86,87] Tc is defined as the temperature where the inverse dielectric constant deviates from the linear behavior in $1/\varepsilon_r$-T curves. Furthermore, the determined temperatures were also controlled by comparing with the temperatures at which the steepest decrease of remanent polarization occurs, as will be shown later.

Figure 3.18 (a)-(f) clearly shows that as the BLT ratio increases, T_d approaches the room temperature. Since the second anomaly that corresponds to the T_C remains almost the same for all compositions, the dielectric plateau is observed in a wide temperature range for the $0.03 \leq x \leq 0.07$ samples. In the case of x=0.08 sample, it is clear that T_d is observed at a temperature lower than the room temperature. Therefore, only the Curie temperature was determined in this composition.

For all ceramic samples, an increase in frequency dependence of dielectric behavior was observed between the T_d and T_C temperature range. T_d is responsible for the major peak of all ceramics where the frequency dependence of dielectric constant is higher than that of the T_C. This behavior is similar with $(Bi_{1/2}Na_{1/2})TiO_3$.[48]

The ceramic samples exhibit relaxor ferroelectric behavior with increasing amount of BLT content due to the deteriorated long range ferroelectric domain order and the frequency dependence of the dielectric constant increases with increasing amount of BLT.

The change in dielectric constant and dielectric loss with respect to the composition of ceramics are illustrated in Figure 3.19(a)-(b) respectively. As mentioned above, the first anomaly in dielectric constant shifts to lower temperatures with increasing BLT content whereas the temperature of the second anomaly does not change much.

Dielectric loss of ceramics behaves similar to the dielectric constant. Dielectric loss peak corresponding to the T_d shifts to lower temperatures with increasing BLT content whereas no anomaly corresponding to the T_c can be observed. At temperatures higher than 130°C, an artificial increase is observed in dielectric loss of all ceramics due to the increasing conductivity of samples.

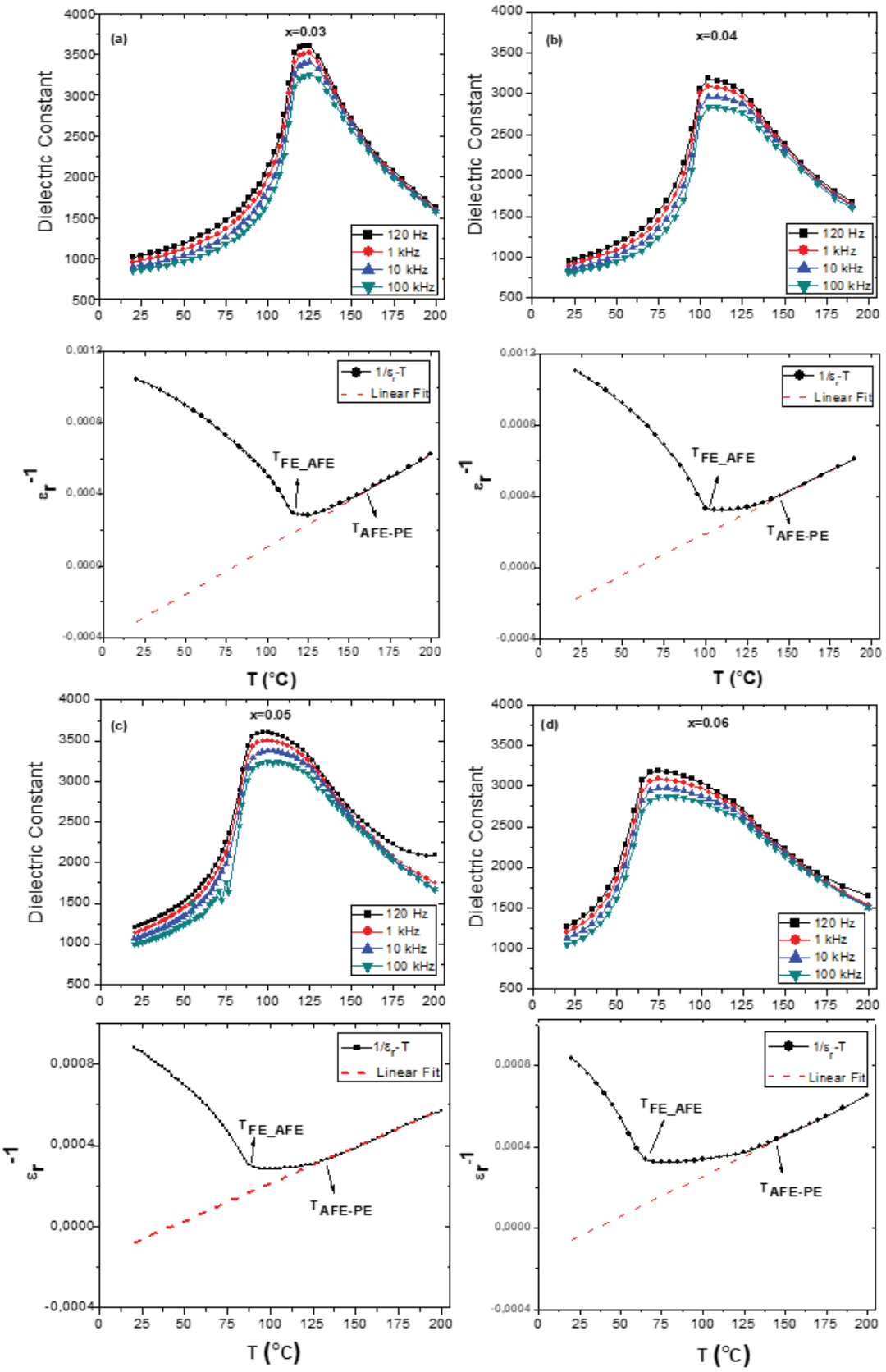
(a)
x=0.03
Dielectric Constant
120 Hz
1 kHz
10 kHz
100 kHz
(b)
x=0.04
(c)
x=0.05
(d)
x=0.06
1/ε_r-T
Linear Fit
T_FE_AFE
T_AFE-PE
T (°C)

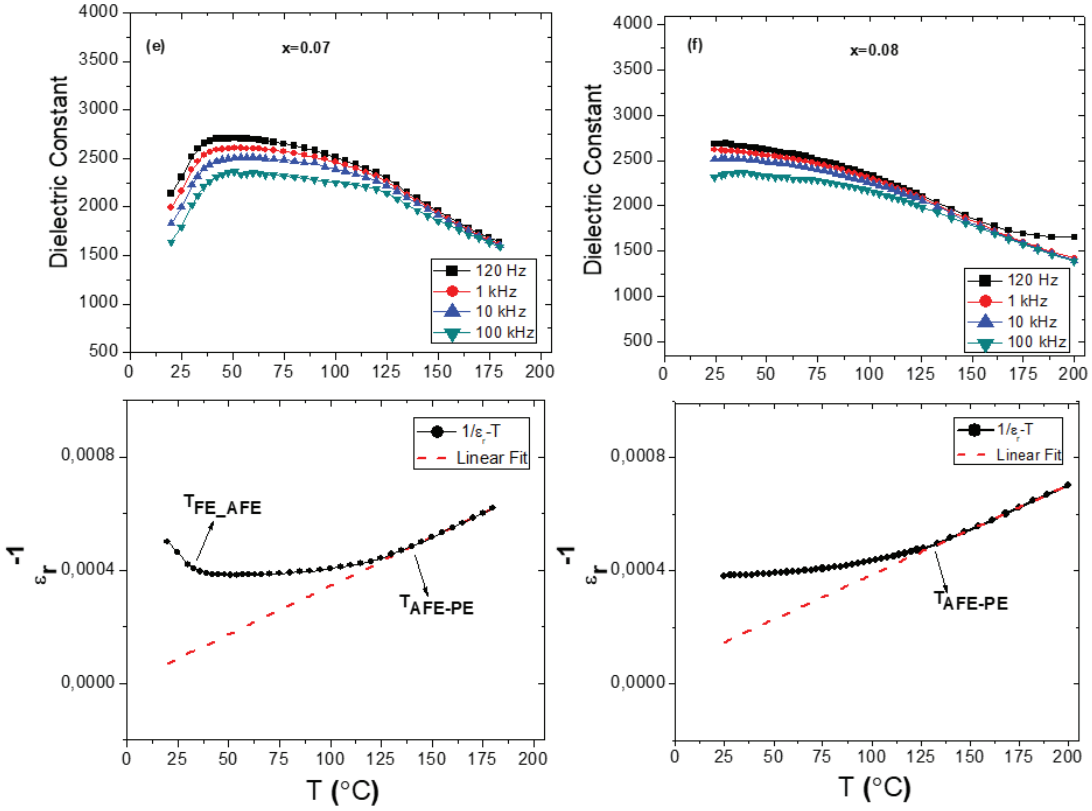

Figure 3.18. (a)-(f) Temperature dependence of dielectric constant ε_r of all $(1-x)BaTiO_3-xBi(Li_{1/3}Ti_{2/3})O_3$ ceramics at different frequencies. Under each graph in (a)-(f) $1/\varepsilon_r$ versus temperature graphs are shown.

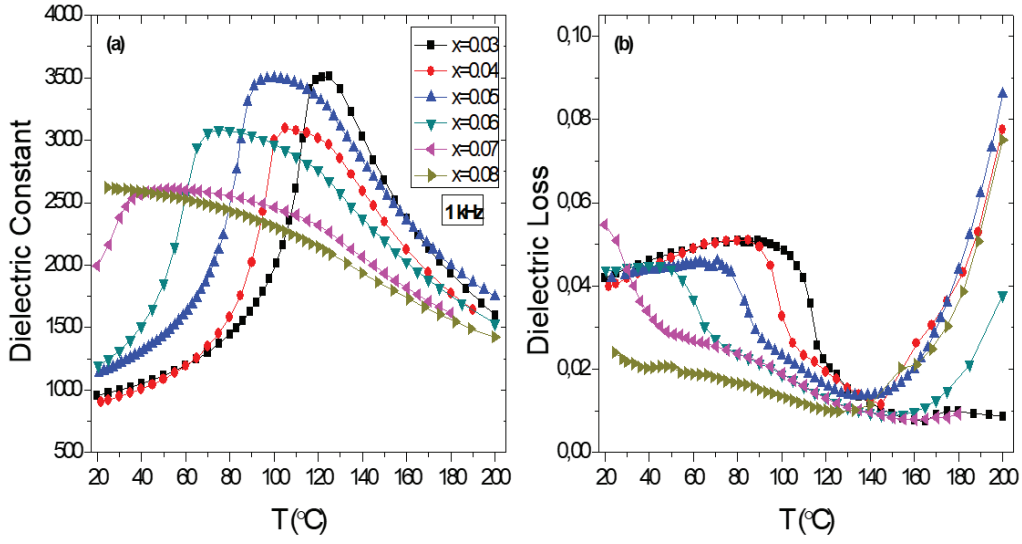

Figure 3.19. Temperature dependence of (a) dielectric constant and (b) tanδ of all $(1-x)BaTiO_3-xBi(Li_{1/3}Ti_{2/3})O_3$ ceramics at 1 kHz.

As it will be shown later in section 3.2.7, the sharp increase in the dielectric losses shown in Figure 3.19(b) affects the electrocaloric character of the ceramics by causing nonphysical behavior in hysteresis loop measurements. In order to get rid of this increase not reflecting the real behavior of ceramics, the highest frequencies that can be reached in electrical measurements have been used. It is known that the response time (frequency) of each polarization type (electronic, ionic, orientation and space charge polarization) to the electric field is different. By increasing the frequency, it is aimed to minimize the contribution of conductivity resulting from space charge polarization.

3.2.5. Hysteresis Loop Measurements

After determining dielectric characteristics and phase temperatures of ceramics, the P(E) hysteresis loops of different compositions of $(1-x)BaTiO_3-xBi(Li_{1/3}Ti_{2/3})O_3$ ceramics were measured up to 30 kV/cm at 35°C by using Aixacct TF1000 instrument and shown in Figure 3.20.

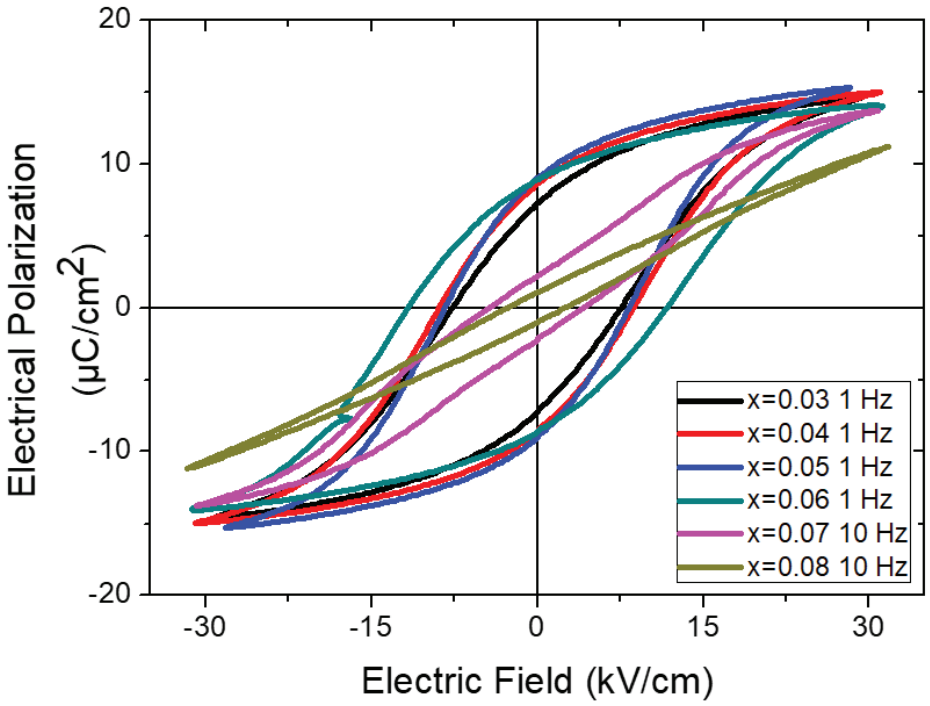

Figure 3.20. Polarization versus electric field plots of $(1-x)BaTiO_3-xBi(Li_{1/3}Ti_{2/3})O_3$ ceramics measured at 1 Hz for $0.03 \leq x \leq 0.06$ and 10 Hz for x=0.07 and 0.08 at 30 kV/cm at 35°C.

The measurement frequencies vary depending on the samples. In order to eliminate the conductivity contribution, the measurement frequency is increased in some samples.

For all compositions except x=0.07 and 0.08, at room temperature, the loops are saturated which is the typical behavior of ferroelectric materials based on the domain switching of long range ferroelectric order.[88] As displayed in Figure 3.20, the coercive field E_c and remanent polarization P_r sre nearly the same for $0.03 \leq x \leq 0.06$ and P_r reaches the maximum value of 9.03 μC/cm^2 for x=0.05. However, further increase in $Bi(Li_{1/3}Ti_{2/3})O_3$ content leads to sharp decrease in both remanent polarization and coercive field due to the increasing B-site disorder and relaxor character as evidenced by the slim loop of x=0.08.

The E_c and P_r values of all compositions at 35°C are summarized in Table 3.3. By making a comparison with the previous BT-BLT study[55] it can be concluded that a similar trend with composition is observed in our study at 35°C. Howeve, unlike the previous study, x=0.07 sample exhibits a pinched hysteresis loop at room temperature.

Table 3.3. Coercive field and remanent polarization values of all $(1-x)BaTiO_3-xBi(Li_{1/3}Ti_{2/3})O_3$ ceramics.

Composition	***x=0.08***	***x=0.07***	***x=0.06***	***x=0.05***	***x=0.04***	***x=0.03***
E_c (kV/cm)	*2.64*	*4.22*	*11.65*	*8.29*	*8.73*	*7.46*
P_r (μC/cm²)	*1.07*	*2.22*	*8.9*	*9.03*	*8.6*	*7.21*

The P(E) hysteresis loops of different compositions of BT-BLT ceramics at different temperatures are shown in Figure 3.21 (a)-(f). The temperature dependent hysteresis curves for $0.03 \leq x \leq 0.07$ clearly show that the temperature at which the pinched loop was observed approaches the room temperature with increasing amount of BLT. For x=0.08 sample, relaxor behavior was observed at all given temperatures with low E_c and P_r.

Current density-electric field (J-E) graphs are plotted in order to better understand the character of the hysteresis loops and ferroelectric-antiferroelectric phase transition and are shown in Figure 3.22(a)-(f).

J-E graphs show that at a certain temperature (called as T_{FE-AFE} which corresponds to T_d defined from dielectric measurements) depending on the composition, the current

density behavior changes. For compositions $0.03 \leq x \leq 0.06$ at low temperatures, two peaks corresponding to switching of domains can be observed. This is the proof of long-range ferroelectric order. When $T_d \leq T \leq T_c$ two additional peaks (Figure 3.22(b)-(e)) were observed. For example, for x=0.05 sample at 32°C only two peaks are observed corresponding to the saturated hysteresis loop whereas at 85°C two more peaks can be seen and the hysteresis loop at this temperature becomes pinched. The current peaks of 1 and 3 can be attributed to the transition from antiferroelectric phase to ferroelectric phase that induced by application of electric field. The current peaks 2 and 4 indicate the reverse transition. Four current peaks were also found in NBT-BT-based systems.[89–91] Observation of four peaks in J-E graphs indicates that there is a reversible structure change between weakly polar phase or antiferroelectric phase to ferroelectric phase.[92] Above T_c, J-E loops do not show any peak and the loops become linear. At 30°C, x=0.07 sample already shows 4 peaks corresponding to its pinched hysteresis loop. On the other hand, x=0.08 sample does not show any clear peaks in the J-E curves as the material becomes relaxor which shows a slim hysteresis loop.

Rise in the content of $Bi(Li_{1/3}Ti_{2/3})O_3$ in BT-BLT ceramics lead to destabilize ferroelectric phase and ‘’pinched’’ loops appear[93] suggesting the coexistence of FE and AFE-like behavior.[86] The destabilization of ferroelectric phase might be due to the decrease of the tolerance factor (t).[94] The Goldschmidt tolerance factor for an ABO_3 perovskite structure is calculated by using Equation 1.2, where r_A, r_B and r_O are the ionic radii of A, B-site ions and oxygen ions, respectively.[95]

It was reported that decreasing tolerance factor change polar order that is tuned into antipolar order. This phenomena is observed in doped $NaNbO_3$[96] and doped $BiFeO_3$[97–99]. The same condition might be present here due to size difference between B-site ions.

Destabilization of the ferroelectric phase can be correlated with the tolerance factor as well as the character of the bond. Figure 3.23 shows the electronegativity difference (x) vs tolerance factor of BT-BLT ceramics. Electronegativity difference is calculated by using the following equation[100] where x_{AO} is the electronegativity difference between oxygen and A site ion and x_{BO} is the difference between oxygen and B site ion.

$$x = \frac{x_{AO} + x_{BO}}{2}$$

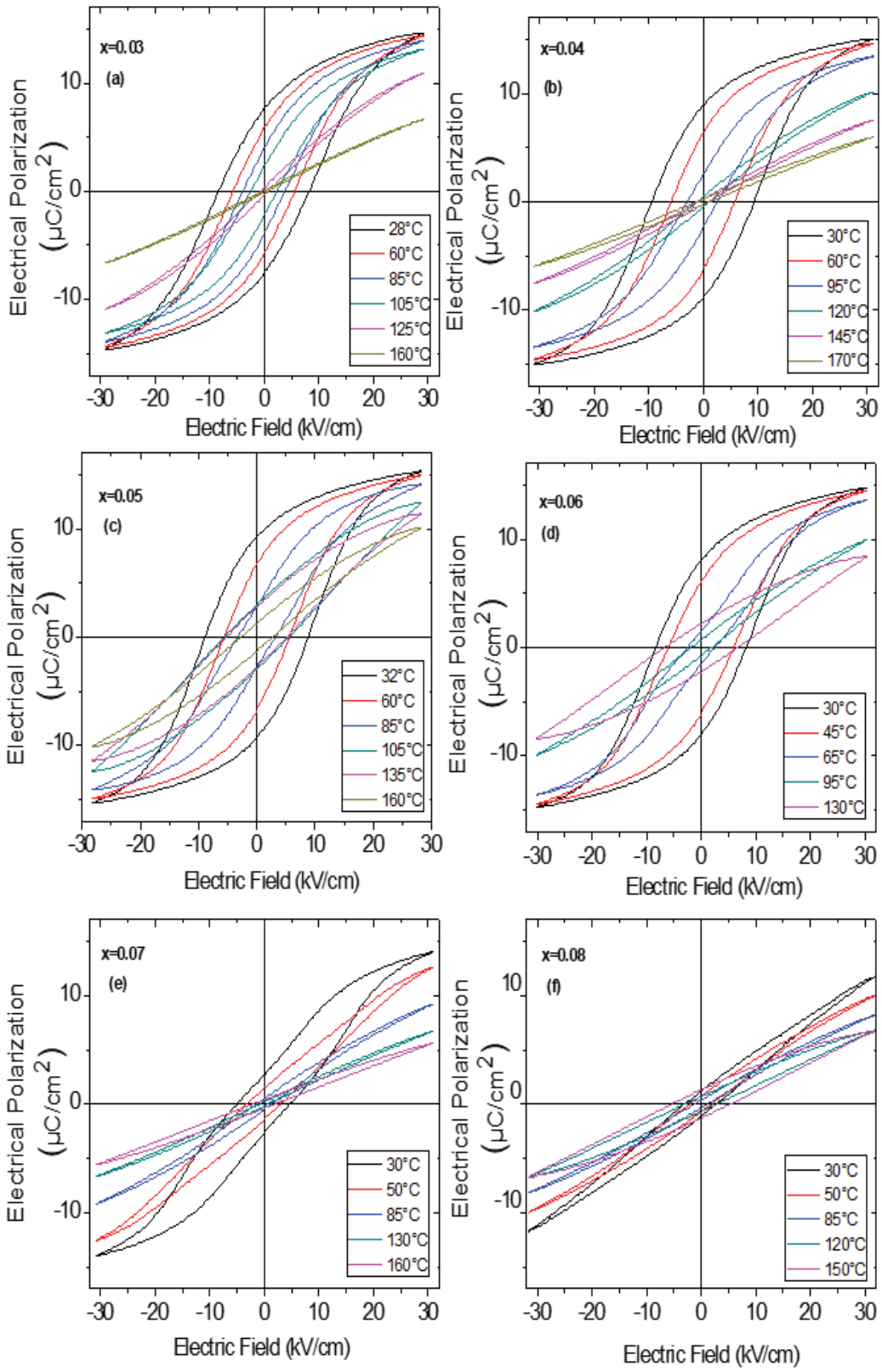

Figure 3.21. (a)-(f) Polarization hysteresis loops of all $(1-x)BaTiO_3-xBi(Li_{1/3}Ti_{2/3})O_3$ ceramics measured at different temperatures.

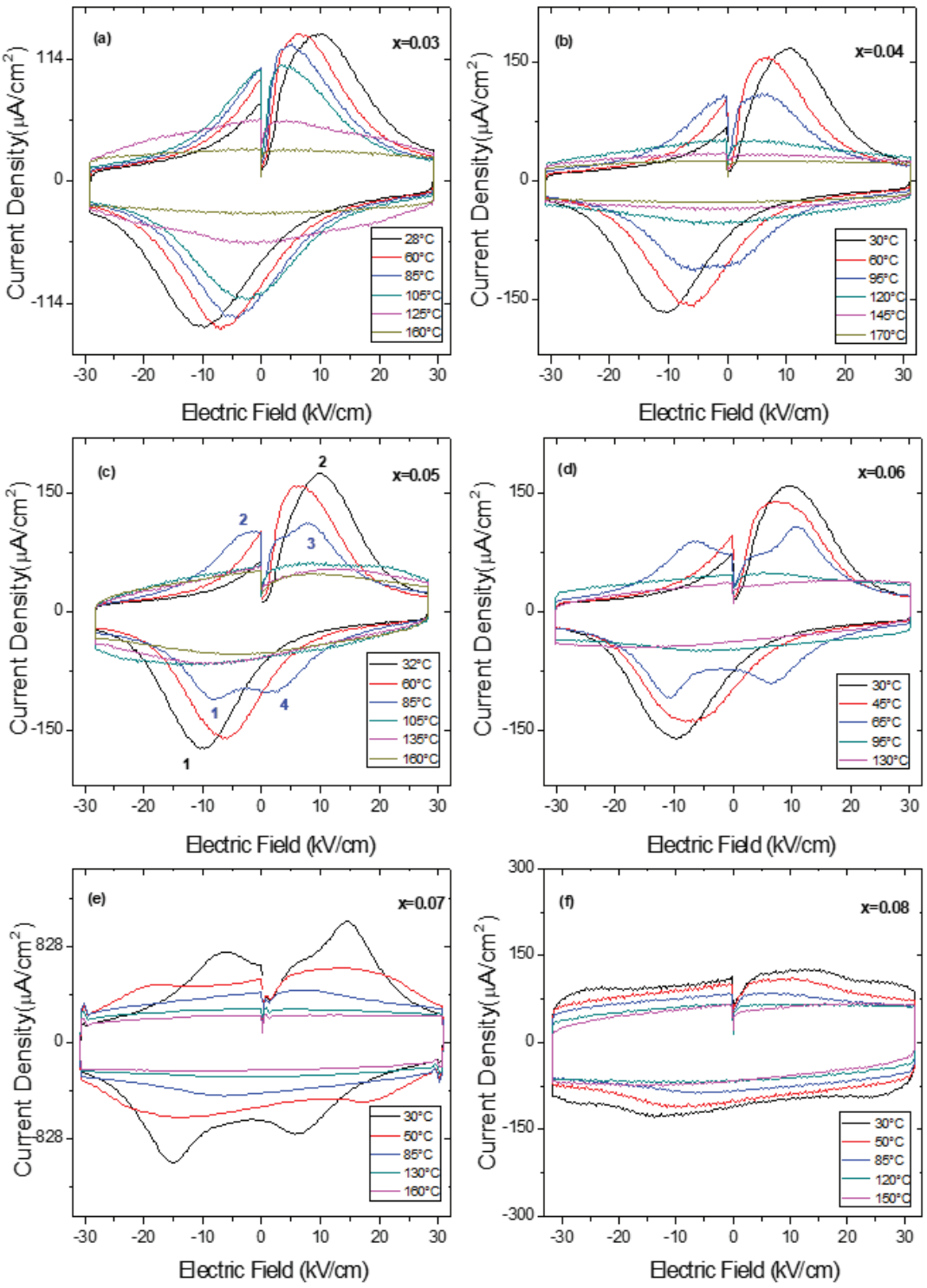

Figure 3.22. Current-electric field (J-E) curves of all $(1-x)BaTiO_3-xBi(Li_{1/3}Ti_{2/3})O_3$ ceramics measured at different tempeatures at 10 Hz.

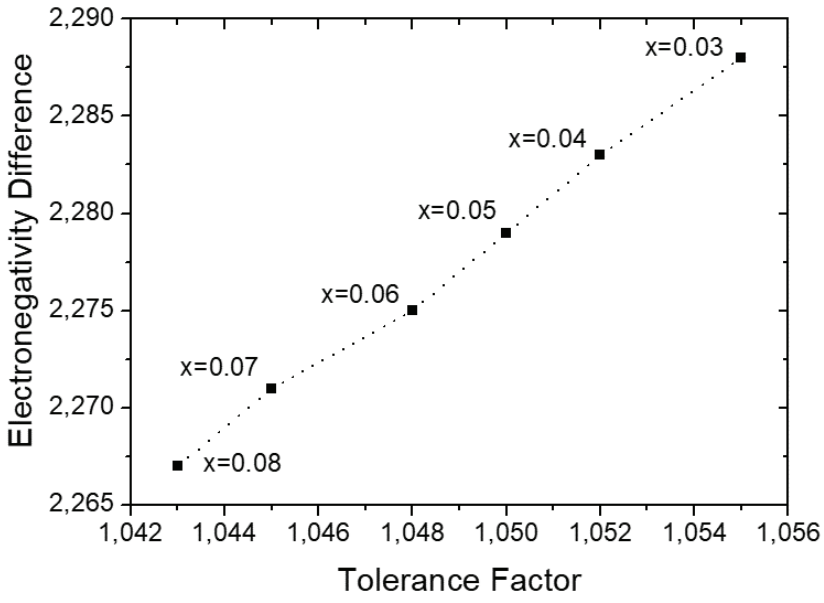

Figure 3.23. Electronegativity difference vs tolerance factor plot of all $(1-x)BaTiO_3-xBi(Li_{1/3}Ti_{2/3})O_3$ ceramics.

Adding $Bi(Li_{1/3}Ti_{2/3})O_3$ decreases the tolerance factor and the ionic character of the bonds. Increase in the covalency of the bonds lead to less stable perovskite structure resulting in destabilization of the perovskite structure.[96]

3.2.6. Strain-Electric Field Measurements

Strain-electric field (S-E) measurements were done by using a MTI 2100 Photonic Sensor that is integrated to the Radiant Precision LC ferroelectric property measurement system to differentiate between the antiferroelectric and ferroelectric character of the ceramics. Strain-electric field loops are measured simultaneously with the polarization-electric field loops. Figure 3.24(c) illustrates the room temperature S-E curves of $(1-x)BaTiO_3-xBi(Li_{1/3}Ti_{2/3})O_3$ for x=0.07 and x=0.03, the samples which display ferroelectric and antiferroelectric behavior in P-E loops, respectively. x=0.03 ceramic sample shows the typical butterfly-shaped strain curve and negative strain, which is the difference between zero-field strain and lowest strain. Negative strain and butterfly shape are consistent with the ferroelectric behavior.[101] In contrast, for x=0.07 the butterfly-shaped loop transforms into sprout-shaped S-E loop and the negative strain that originates from the long-range order disappears,[102] consistent with antiferroelectric character.

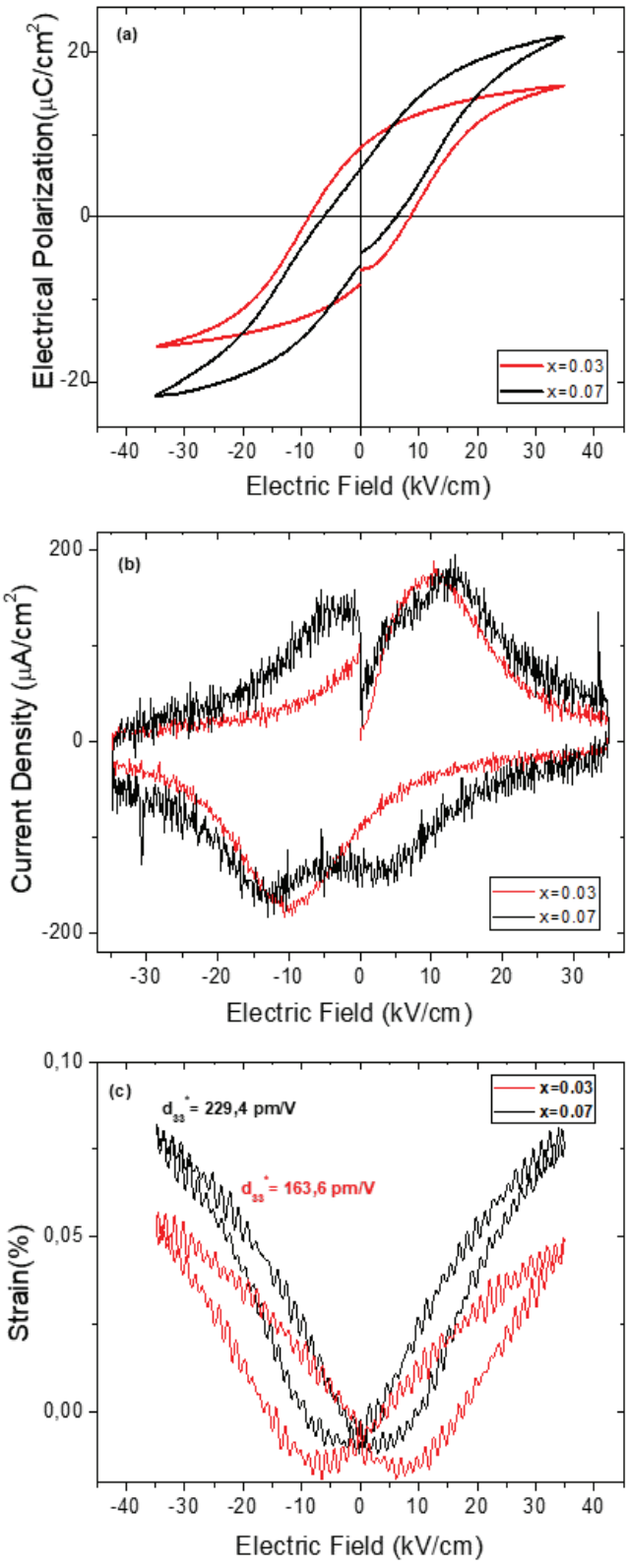

Figure 3.24. (a) Electrical polarization versus electric field (b) current density versus electric field and (c)Bipolar S(E) curves of $(1-x)BaTiO_3-xBi(Li_{1/3}Ti_{2/3})O_3$ (x=0.03 and x=0.07) measured at room temperature.

This result is in good agreement with the behavior observed in polarization hysteresis loops. The same phenomena is also observed in NBT-BT-KNN[101], NBT-BKT[88], NBT-BT[86], BMT-PT-NBT[91] and BMT-NBT-BT[49] ceramics. Table 3.4 summarizes the normalized strain values obtained in this study and provides a comparison with some NBT-based ceramics.

As can be seen from the table, the value obtained for AFE x=0.07 is larger than that of x=0.03 which is expected during the field induced AFE-FE transition large strain values are obtained.[101] The values obtained in this study are lower than literature values. This can be due to lower dielectric breakdown strength of our samples which prevented us to measure above 55 kV/cm.

Table 3.4. Comparison of normalized strain d_{33}^* (S_{max}/E_{max}) of various NBT-based ceramics.

Composition	***d_{33}^****	***Ref.***
(1-x)BNKT-xBNbT (x=0.03)	*683*	103
(1-x)BNKT-xBNbT (x=0.01)	*317*	103
BNT-BT	*240*	69
0.03NBT-0.05BT-0.02KNN	*276*	101
0.02NBT-0.06BT-0.02KNN	*567*	101
PMN-PT	*560-710*	69
x=0.03	*163.6*	*This study*
x=0.07	*229.4*	*This study*

3.2.7. Temperature Dependent X-Ray Diffraction

Temperature-dependent XRD measurements were performed to prove the FE-AFE phase transition and to determine the phase transition temperature by Dr. Gwilherm Nénert at PanAnalytical the Netherlands.

Figure 3.25 shows the change in unit cell parameters as a function of temperature obtained from profile fits (done by Dr. Nénert) of the temperature-dependent XRD measurements for x = 0.05 sample. The unit cell parameters change at the anomaly temperature corresponding to the FE-AFE phase transition in the dielectric constant measurements.

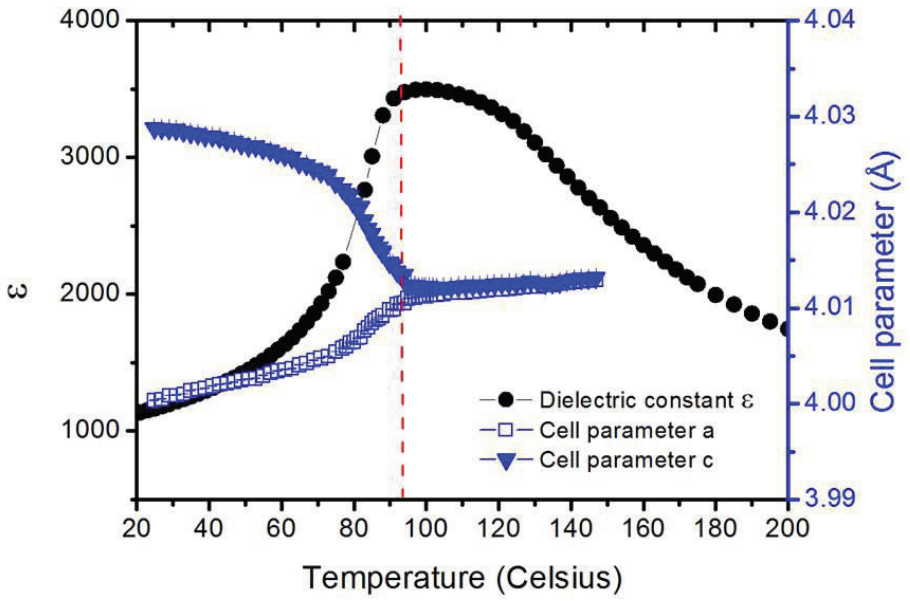

Figure 3.25. The change in unit cell parameters as a function of temperature for x=0.05 sample.

This measurement gives information about the phase transition that occurs from tetragonal FE phase to cubic-like or pseudocubic AFE phase. However, no change was observed in the unit cell parameter at the temperature corresponding to the phase transition from the noncentrosymmetric AFE phase to the cubic PE phase. This may be due to the low symmetry difference between the AFE

3.2.8. Electrocaloric Effect Calculations

The polarization versus temperature graphs obtained by extracting polarization values from the upper branches of hysteresis loop measurements are shown in Figure 3.26(a)-(f) for all the compositions under different electric fields.

For $0.03 \leq x \leq 0.06$ samples, the polarization at 0 kV/cm (P_r) sharply decreases at a temperature corresponding roughly to T_d. The temperature of the sharp decrease shifts to higher values as the electric field is increased which is caused by the stabilization of ferroelectricity under applied electric field. This decrease in polarization takes place around room temperature for x=0.07 sample as T_d of this sample is close to the room temperature. Since x=0.10 shows relaxor properties no T_d was observed in dielectric measurements and correspondingly no sharp decrease can be seen in P-T curves. Polarization slowly decreases with temperature. In general, electrical polarization

decreases with increasing temperature for a ferroelectric material. Only a transition from antiferroelectric phase to a ferroelectric phase might cause an increase in polarization. In all other circumstances the increase in the polarization is artificial and is caused by conductivity contributions in not perfectly insulating materials. In this regard, for example, the polarization increase above 125°C for x=0.05 sample is considered to be artificial.

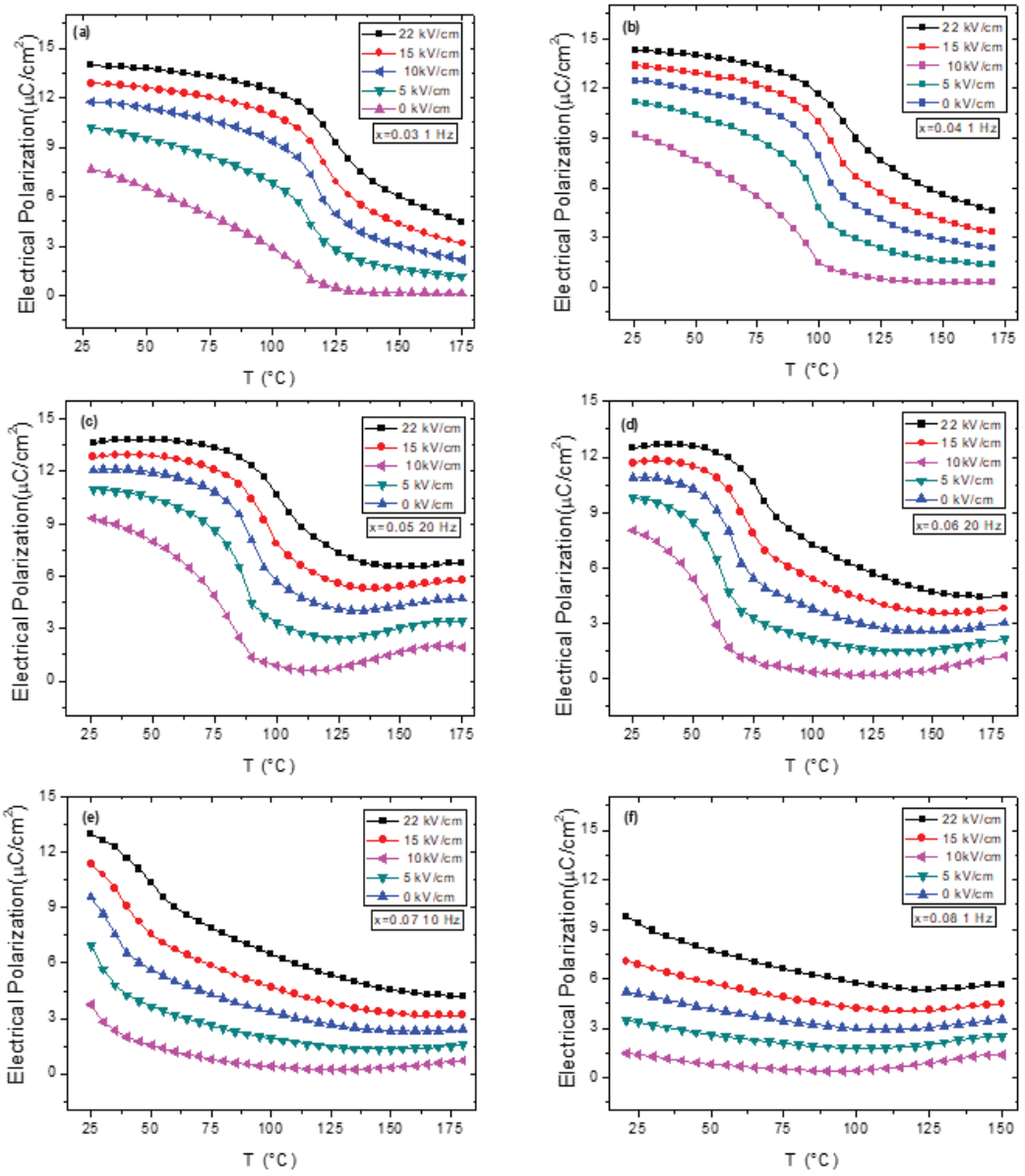

Figure 3.26. (a)-(f) Polarization-electric field graphs of all (1-x)$BaTiO_3$-x$Bi(Li_{1/3}Ti_{2/3})O_3$ ceramics measured at given frequencies for (a) x=0.03, (b) x=0.04, (c) x=0.05, (d) x=0.06, (e) x=0.07 and (f) x=0.08.

Equations 3.2 and 3.3 based on the Maxwell relation $(\partial P/\partial T)_E=(\partial S/\partial E)_T$ were used to determine the adiabatic temperature change ΔT and isothermal entropy change ΔS due to the applied electric field change from E_1 to E_2, for the material with measured density ρ as in Table 3.2 and assumed heat capacity C_p (C_p= 0.50 J/g.K) based on $BaTiO_3$-based compositions in the literature.[33,78–80]

$$\Delta T = -\frac{T}{\rho C_p}\int_{E_1}^{E_2}\left(\frac{\partial P}{\partial T}\right)_E dE \quad (3.2)$$

$$\Delta S = \frac{1}{\rho}\int_{E1}^{E2}\left(\frac{\partial P}{\partial T}\right) dE \quad (3.3)$$

The calculated temperature dependence of ΔT and ΔS at 22 kV/cm are presented in Figures 3.27(a) and 27(b), respectively. The samples show peaks in the EC responses around the phase transition temperatures from the ferroelectric phase to the antiferroelectric phase (T_{FE-AFE}). As mentioned before, T_{FE-AFE} transition temperature (T_d) decreases down to the room temperature as the BLT content increases. Thus, ΔT_{max} peak shifts from 125°C to 60°C upon increasing the BLT content.

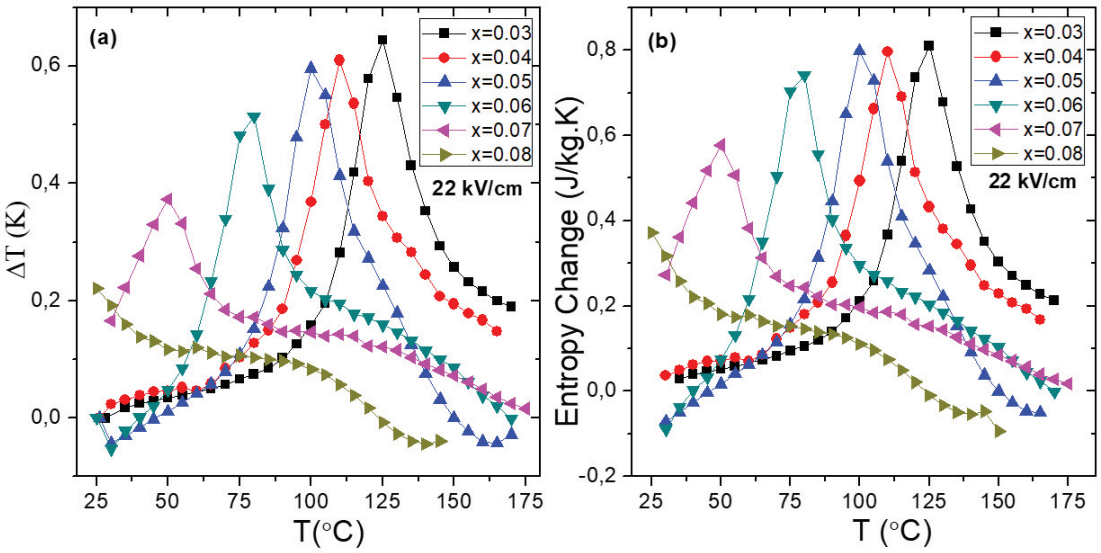

Figure 3.27. Temperature dependence of ΔT and ΔS of all $(1-x)BaTiO_3-xBi(Li_{1/3}Ti_{2/3})O_3$ ceramics at 22 kV/cm.

No electrocaloric temperature change was obtained corresponding to the second phase transition (T_{AFE-PE}). It is thought that the absence of the electrocaloric temperature

change peak at the temperature around T_{AFE-PE} is due to low symmetry difference between nonpolar cubic-like AFE and cubic PE phases.

Table 3.5. Comparison of the ECE properties for different materials.

Material	T (K)	ΔT (K)	ΔE (kV/cm)	ΔT/ΔE (10^{-6} K.m/V)	Ref.
NBT-ST (x=0.25)	333	1.64	50	0.33	39
NBT-ST (x=0.26)	323	1.52	50	0.3	39
$BaTi_{0.895}Sn_{0.105}O_3$	301	0.61	20	0.31	32
KNN-ST	340	1.9	159	0.12	40
$Ba_{0.65}Sr_{0.35}TiO_3$	303	2.1	90	0.23	104
$0.94Bi_{0.5}Na_{0.5}TiO_3$-$0.06KNbO_3$	349	1.73	70	0.24	41
$0.87Pb(Mg_{1/3}Nb_{2/3})O_3$–$0.13PbTiO_3$	343	0.556	24	0.23	27
$Na_{0.5}Bi_{0.5}TiO_3$–$BaTiO_3$	298	-0.12	50	0.024	105
$Ba_{0.8}Ca_{0.2}(Zr_{0.04}Ti_{0.96})O_3$	389	0.27	7,95	0.34	35
NBBST0.10	383	0.22	40	0.18	38
x=0.03	398	0.66	22	0.3	**Present study**
x=0.04	383	0.61	22	0.28	**Present study**
x=0.05	373	0.59	22	0.27	**Present study**
x=0.06	353	0.52	22	0.24	**Present study**
x=0.07	323	0.38	22	0.17	**Present study**
x=0.08	298	0.23	22	0.10	**Present study**

According to the ECE parameters listed in Table 3.5, x=0.03 sample showed a maximum ECE ΔT_{max}=0.66 K under 22 kV/cm. This composition has a electrocaloric efficiency or electrocaloric strength ($\Delta T/\Delta E$) of 0.03 K.cm/kV which is relatively high compared with the literature. The EC temperature change values of x =0.04 and 0.05 samples were very close to each other and found as 0.28 and 0.27 K ,respectively. The increase in BLT amount lowers the ΔT value down to 0.10 K for x=0.08 sample. As the amount of BLT increases, the first order phase transition character of BT is distorted and the sharpness of the change in polarization as a function of temperature decreases. Thus, the decrease in the $\partial P/\partial T$ causes the decrease in ΔT value. As can be seen in Figure

3.27(b) the entropy change follows the same trend with electrocaloric temperature change.

After phase transition temperatures T_{FE-AFE} and T_{AFE-PE} are determined by the dielectric measurements that are confirmed by other electrical measurements, the phase diagram is obtained and given in Figure 3.28. As mentioned in dielectric measurements part, there are several methods for determining the temperature of depolarization. The two can be used for this thesis are the point of the steepest decrease of remanent polarization and the first anomaly in the dielectric constant versus temperature graphs. The blue dots represent the phase transition temperature from FE to AFE phase (T_{FE-AFE}) determined by the steepest decrease of P_r and the red circle shows the same temperature determined using dielectric constant versus temperature graphs. The green triangle shows the AFE-PE transition temperatures (T_{AFE-PE}) of the samples determined from ε_r^{-1}-T.

As seen in Figure 3.28, there is a small difference between two different methods. As the BLT content (x) increases, the ferroelectric-antiferroelectric phase transition temperature (T_{FE-AFE}) decreases while the antiferroelectric-paraelectric phase transition temperature (T_{AFE-PE}) almost same for all compositions. The obtained phase diagram is similar to the unpoled $(1-x)(Bi_{1/2}Na_{1/2})TiO_3$-$xBaTiO_3$ material.[48]

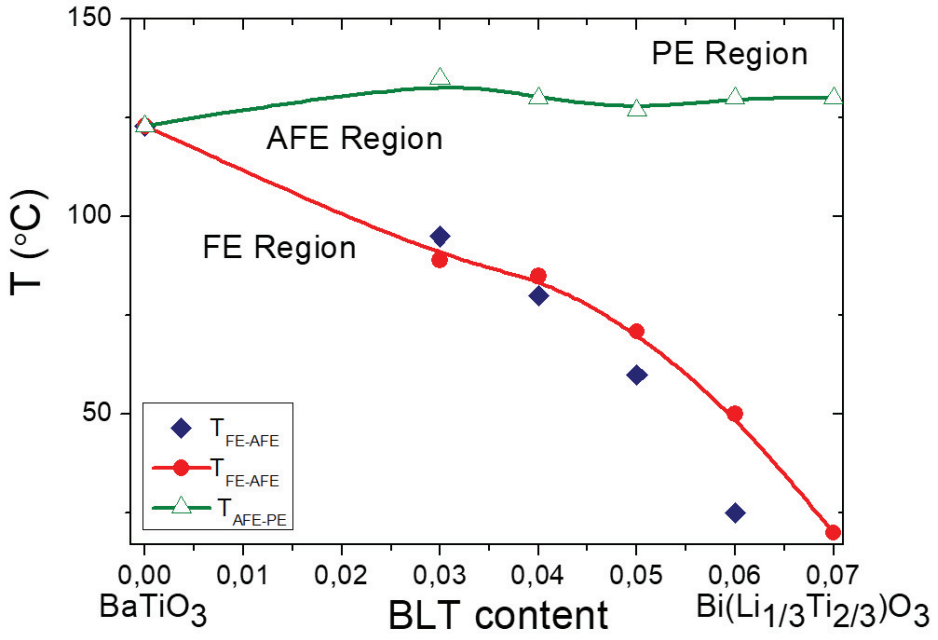

Figure 3.28. Phase diagram of the $(1-x)BaTiO_3-xBi(Li_{1/3}Ti_{2/3})O_3$ ceramics.

In summary, comparing the results of synthesis route-I and route-II shows the importance of processing-structure-property relationship. Sintering temperatures of the ceramics were kept low in both synthesis routes in order to prevent the evaporation of Bi^{3+} and Li^{+}. In the synthesis route-I, the formation of the core-shell structure was facilitated by inhomogeneous particle size distribution and all compositions exhibit a peak in ΔT curve the temperature of which does not change with respect to the composition. This peak corresponds to the core contribution. However, no shell contribution was observed except for x=0.07. The same behavior confirmed by dielectric measurements. Since the core-shell structure was thought to suppress the MBP effect, sytnhesis route-II was followed in order to get rid of the core-shell structure. Milling process is used more effectively in route-II and high density materials are obtained thanks to the lower particle size obtained after calcination. In route-II, the electrical properties of the ceramics completely changed and AFE property was observed in all samples. In comparision with the other BT-BLT study in the literature,[106] different dielectric behavior is observed.

CHAPTER 4

CONCLUSIONS

This thesis includes studies on one of the alternative cooling technologies named as "electrocaloric effect (ECE)".

The electrocaloric effect of the promising Bismuth-based system, $(1-x)BaTiO_3-xBi(Li_{1/3}Ti_{2/3})O_3$ was investigated with different synthesis conditions.

4.1. Synthesis Route-I

In the first part of this thesis study, the ECE of ceramics synthesized with synthesis conditions similar to the literature was studied. In the literature how core-shell microstructure affects the electrocaloric behavior has not been studied. For this reason, the effect of the core-shell structure on ECE was studied.

ΔT graphs of all compositions exhibit a peak around the Curie temperature of $BaTiO_3$ that does not change with composition even if the symmetry changes are observed in XRD measurements. This peak is attributed to the core. Same behavior was also observed in the dielectric constant of all compositions. In contrast, a contribution of shell structure could not be observed. Depending on the synthesis conditions, it is thought that the core-shell structure and the size of the core and shell may change with the amount of BLT diffusing into the core structure. Therefore, the shell contribution differs from the literature.

Maximum electrocaloric temperature change was obtained as 0.532 K at 22 kV/cm electric field in x=0.03 sample. The ΔT values decreased with increasing BLT(x). As the amount of dopant increases, B-site disorder increase and the polarization changes less abruptly at the Curie temperature therefore ΔT value decreases.

4.2. Synthesis Route-II

The aim of the second part was to get rid of the core-shell structure and to obtain highly dense ceramics by changing the synthesis conditions of ceramic materials.

Therefore, particle sizes were reduced by using the ball mill more effectively and highly dense ceramics were obtained with density values greater than 93% of the theoretical density.

Two anomalies can be defined in dielectric constant-temperature graph, which are named as depolarization temperature (T_d) and Curie temperature (T_c). T_d is the depolarization temperature which corresponds to the transition from a ferroelectric phase to the antiferroelectric phase. The samples show peaks in the EC responses around the phase transition temperatures from the ferroelectric phase to the antiferroelectric phase (T_{FE-AFE}). T_{FE-AFE} transition temperature (T_d) decreases down to the room temperature as the BLT content increases. Thus, ΔT_{max} peak shifts towards the room temperature upon increasing the BLT content. No electrocaloric temperature change was obtained corresponding to the second phase transition (T_{AFE-PE}). It is thought that the absence of the electrocaloric temperature change peak at the temperature around T_{AFE-PE} is due to low symmetry difference between nonpolar or cubic-like AFE and cubic PE phases.

ΔT was calculated by using Maxwell relations and P-T curves obtained from hysteresis loop measurements. x=0.03 ceramic sample showed a maximum ECE ΔT_{max}=0.66 K under 22 kV/cm. This composition has an electrocaloric efficiency or electrocaloric strength ($\Delta T/\Delta E$) of 0.03 K.cm/kV which is relatively high compared with the literature. The EC temperature change values of x =0.04 and 0.05 samples were very close to each other and found as 0.28 and 0.27 K ,respectively. The increase in BLT amount lowers the ΔT value down to 0.10 K for x=0.08 sample.

In conclusion, in this thesis, it was discovered that BLT substitution induces AFE behavior in $(1-x)BaTiO_3-xBi(Li_{1/3}Ti_{2/3})O_3$ ceramics. FE-AFE phase transition observed in samples causes a relatively large ECE. Obtained ECE values are comparable with other prominent Pb-free systems. $(1-x)BaTiO_3-xBi(Li_{1/3}Ti_{2/3})O_3$ therefore can be considered as a promising system for EC cooling.

REFERENCES

(1) Neudeck, P. G.; Trunek, A. J.; Spry, D. J.; Powell, J. A.; Du, H.; Skowronski, M.; Huang, X. R.; Dudley, M. Ferroelectric Materials. *Chem. Vap. Depos.* **2006**, *12* (8–9), 531–540.

(2) Callister, W.; Rethwisch, D. Materials Science: An Introduction., 9th ed. **2013**, 990.

(3) Setter, N. What Is a Ferroelectric-a Materials Designer Perspective. *Ferroelectrics* **2016**, *500* (1), 164–182.

(4) Damjanovic, D. Hysteresis in Piezoelectric and Ferroelectric Materials. **2006**, pp 337-462.

(5) Wang, C.-M.; Lau, K.; Wang, Q. Dynamic Hysteresis and Scaling Behaviours of Lead-Free $0.94Bi_{0.5}Na_{0.5}TiO_3$–$0.06BaTiO_3$ Bulk Ceramics. *RSC Adv.* **2016**, *6* (36), 30148–30153.

(6) Luisman, L.; Feteira, A.; Reichmann, K. Weak-Relaxor Behaviour in Bi/Yb-Doped $KNbO_3$ Ceramics. *Appl. Phys. Lett.* **2011**, *99* (19), 1–4.

(7) Milton, F. P.; Londono, F. A.; Botero, E. R.; Eiras, J. A.; Garcia, D. Thermal Behavior of Electrically Induced Birefringence of La-Doped PMN-PT Ceramics. *Integr. Ferroelectr.* **2015**, *166* (1), 180–185.

(8) Delgado, M. Phase Transitions in Relaxor Ferroelectrics. **2005**, pp 1–11.

(9) Handbook of Condensed Matter and Materials Data. Martiessen, W.; Warlimont, H. Ed.; section 4.5 *Ferroelectrics and Antiferroelectrics*, pp 903-915.

(10) Rabe, K. M. Antiferroelectricity in Oxides: A Reexamination. *Funct. Met. Oxides New Sci. Nov. Appl.* **2013**, 221–244.

(11) Hao, X.; Zhai, J.; Kong, L. B.; Xu, Z. A Comprehensive Review on the Progress of Lead Zirconate-Based Antiferroelectric Materials. *Prog. Mater. Sci.* **2014**, *63*, 1–57.

(12) Goupil, F. Le. Electrocaloric Effect in Ferroelectric Relaxors : The Road to Solid-State Cooling. **2013**.

(13) Valant, M. Progress in Materials Science Electrocaloric Materials for Future Solid-State Refrigeration Technologies. *Prog. Mater. Sci.* **2012**, *57* (6), 980–1009.

(14) Kutnjak, Z.; Rozic, B.; Pirc, R. Effect, Electrocaloric Effect: Theory, Measurements and Applications Electrocaloric Effect in Brief: General

Introduction. **2015**, pp 1-19.

(15) Kitanovski, A.; Tu, J.; Poredo, A. Electrocaloric Refrigeration : Thermodynamics,State of the Art and Future Perspectives. *Int. J. Refr.* **2013**, *(40),* 174-188.

(16) Ma, R.; Zhang, Z.; Tong, K.; Huber, D.; Kornbluh, R.; Ju, Y. S.; Pei, Q. Highly Efficient Electrocaloric Cooling with Electrostatic Actuation. *Science.* **2017**, *357* (6356), 1130–1134.

(17) Mischenko, A. S.; Zhang, Q.; Scott, J. F.; Whatmore, R. W.; Mathur, N. D. Giant Electrocaloric Effect in PZT. *Science.* **2006**, *104* (1), 9–13.

(18) Valant, M.; Dunne, L. J.; Axelsson, A. K.; Alford, N. M. N.; Manos, G.; Peräntie, J.; Hagberg, J.; Jantunen, H.; Dabkowski, A. Electrocaloric Effect in a Ferroelectric $Pb(Zn_{1/3}Nb_{2/3})O_3$-$PbTiO_3$ Single Crystal. *Phys. Rev. B - Condens. Matter Mater. Phys.* **2010**, *81* (21), 18–22.

(19) Zhang, R.; Wang, Y.; Zhang, W. Preparation and Characterization of (1-x)$Pb(Mg_{1/3}Nb_{2/3})O_3$-x$PbTiO_3$ Electrocaloric Ceramics. *Cryst. Res. Technol.* **1998**, 33 (5), 827-832.

(20) Luo, L.; Chen, H.; Zhu, Y.; Li, W.; Luo, H.; Zhang, Y. Pyroelectric and Electrocaloric Effect of 〈111〉-Oriented 0.9PMN-0.1PT Single Crystal. *J. Alloys Compd.* **2011**, *509* (32), 8149–8152.

(21) Saranya, D.; Chaudhuri, A. R.; Parui, J.; Krupanidhi, S. B. Electrocaloric Effect of PMN-PT Thin Films near Morphotropic Phase Boundary. *Bull. Mater. Sci.* **2009**, *32* (3), 259–262.

(22) Chukka, R.; Cheah, J. W.; Chen, Z.; Yang, P.; Shannigrahi, S.; Wang, J.; Chen, L. Enhanced Cooling Capacities of Ferroelectric Materials at Morphotropic Phase Boundaries. *Appl. Phys. Lett.* **2011**, *98* (24), 193–196.

(23) Wang, X. Composition Dependence of Electrocaloric Effect in $(1-x)Pb(Mg_{1/3}Nb_{2/3})O_3-xPbTiO_3$ Single Crystals. *Commun. Theor. Phys.* **2015**, *64*, 113-118

(24) Guyomar, D.; Sebald, G.; Guiffard, B.; Seveyrat, L. Ferroelectric Electrocaloric Conversion in $0.75(PbMg_{1/3}Nb_{2/3}O_3)$-$0.25(PbTiO_3)$ Ceramics. *J. Phys. D. Appl. Phys.* **2006**, *39* (20), 4491–4496.

(25) Sebald, G.; Seveyrat, L.; Guyomar, D.; Lebrun, L.; Guiffard, B.; Pruvost, S. Electrocaloric and Pyroelectric Properties of $0.75Pb(Mg_{1/3}Nb_{2/3})O_3$-$0.25PbTiO_3$ Single Crystals. *J. Appl. Phys.* **2006**, *100* (12).

(26) Liu, S.; Li, Y. Research on the Electrocaloric Effect of PMN/PT Solid Solution for Ferroelectrics MEMS Microcooler. *Mater. Sci. Eng. B Solid-State Mater. Adv. Technol.* **2004**, *113* (1), 46–49.

(27) Hagberg, J.; Uusimäki, A.; Jantunen, H. Electrocaloric Characteristics in

Reactive Sintered 0.87Pb($Mg_{1/3}Nb_{2/3}$)O_3-0.13$PbTiO_3$. *Appl. Phys. Lett.* **2008**, *92* (13), 2006–2009.

(28) Kabelka, H.; Fuith, A.; Birks, E.; Sternberg, A. Phase Transitions of $Pb_{0.99}Nb_{0.02}$ ($Zr_{0.75}Sn_{0.20}Ti_{0.05}$)$O_3$ Ceramics. *Ferroelectrics* **2001**, *258* (1), 61–70.

(29) Shebanovs, L.; Borman, K.; Lawless, W. N.; Kalvane, A. Electrocaloric Effect in Some Perovskite Ferroelectric Ceramics and Multilayer Capacitors. *Ferroelectrics* **2002**, *273*, 137–142.

(30) Jaffe, B.; W., C.; H., J. Piezoeletric Ceramics. **1971**, *3*, pp 94.

(31) Kaddoussi, H.; Gagou, Y.; Lahmar, A.; Allouche, B.; Dellis, J. L.; Courty, M.; Khemakhem, H.; El Marssi, M. Ferroelectric Phase Changes and Electrocaloric Effects in Ba($Zr_{0.1}Ti_{0.9}$)$_{1-x}Sn_xO_3$ ceramics Solid Solution. *J. Mater. Sci.* **2016**, *51* (7), 3454–3462.

(32) Luo, Z.; Zhang, D.; Liu, Y.; Zhou, D.; Yao, Y.; Liu, C.; Dkhil, B.; Ren, X.; Lou, X. Enhanced Electrocaloric Effect in Lead-Free $BaTi_{1-x}Sn_xO_3$ Ceramics near Room Temperature. *Appl. Phys. Lett.* **2014**, *105* (10), 102904.

(33) Upadhyay, S. K.; Fatima, I.; Reddy, V. R. Study of Electro-Caloric Effect in Ca and Sn Co-Doped $BaTiO_3$ Ceramics. *Mater. Res. Express* **2017**, *4* (4), 0–8.

(34) Wang, X.; Wu, J.; Dkhil, B.; Zhao, C.; Li, T.; Li, W.; Lou, X. Large Electrocaloric Strength and Broad Electrocaloric Temperature Span in Lead-Free $Ba_{0.85}Ca_{0.15}Ti_{1-x}Hf_xO_3$ceramics. *RSC Adv.* **2017**, *7* (10), 5813–5820.

(35) Asbani, B.; Dellis, J. L.; Lahmar, A.; Courty, M.; Amjoud, M.; Gagou, Y.; Djellab, K.; Mezzane, D.; Kutnjak, Z.; El Marssi, M. Lead-Free $Ba_{0.8}Ca_{0.2}(Zr_xTi_{1-x})O_3$ ceramics with Large Electrocaloric Effect. *Appl. Phys. Lett.* **2015**, *106* (4), 1–5.

(36) Li, J.; Zhang, D.; Qin, S.; Li, T.; Wu, M.; Wang, D.; Bai, Y.; Lou, X. Large Room-Temperature Electrocaloric Effect in Lead-Free $BaHf_xTi_{1-x}O_3$ceramics under Low Electric Field. *Acta Mater.* **2016**, *115*, 58–67.

(37) Qi, S.; Zhang, G.; Duan, L.; Zeng, T.; Cao, J. A Series of Annual Review Articles. *Eur. Heart J.* **2014**, *35* (5), 257.

(38) Luo, L.; Jiang, X.; Zhang, Y.; Li, K. Electrocaloric Effect and Pyroelectric Energy Harvesting of (0.94−x)$Na_{0.5}Bi_{0.5}TiO_3$-0.06$BaTiO_3$-x$SrTiO_3$ceramics. *J. Eur. Ceram. Soc.* **2017**, *37* (8), 2803–2812.

(39) Nieto, V. L.; Savioli, G. B.; Bidner, M. S. On the Inverse Problem of the Estimation of Multiphase Flow Functions. **2004**, *36*, 1–8.

(40) Koruza, J.; Rožič, B.; Cordoyiannis, G.; Malič, B.; Kutnjak, Z. Large Electrocaloric Effect in Lead-Free $K_{0.5}Na_{0.5}NbO_3$-$SrTiO_3$ Ceramics. *Appl. Phys. Lett.* **2015**, *106* (20).

(41) Jiang, X.; Luo, L.; Wang, B.; Li, W.; Chen, H. Electrocaloric Effect Based on the Depolarization Transition in (1-x)$Bi_{0.5}Na_{0.5}TiO_3$-x$KNbO_3$ lead-Free Ceramics. *Ceram. Int.* **2014**, *40* (2), 2627–2634.

(42) Cao, W. P.; Li, W. L.; Xu, D.; Hou, Y. F.; Wang, W.; Fei, W. D. Enhanced Electrocaloric Effect in Lead-Free NBT-Based Ceramics. *Ceram. Int.* **2014**, *40*, 9273–9278.

(43) Wang, X.; Wu, J.; Dkhil, B.; Xu, B.; Wang, X.; Dong, G.; Yang, G.; Lou, X. Enhanced Electrocaloric Effect near Polymorphic Phase Boundary in Lead-Free Potassium Sodium Niobate Ceramics. *Appl. Phys. Lett.* **2017**, *110* (6), 1–6.

(44) Kumar, R.; Singh, S. Giant Electrocaloric and Energy Storage Performance of $[(K_{0.5}Na_{0.5})NbO_3]_{(1-x)}$-$[LiSbO_3]_x$ nanocrystalline Ceramics. *Sci. Rep.* **2018**, *8* (1), 1–9.

(45) Shrout, T. R. Relaxor Based Ferroelectric Single Crystals for Electro-Mechanical Actuators. *Mat. Res. Innovat.* **1997**, *3*, 20–25.

(46) Taylor, P.; Choi, S. W.; Shrout, R. T. R.; Jang, S. J.; Bhalla, A. S. Ferroelectrics Dielectric and Pyroelectric Properties in the $Pb(Mg_{1/3}Nb_{2/3})O_3$-$PbTiO_3$ System. **2012**, 37–41.

(47) Gao, J. Recent Progress on $BaTiO_3$-Based Piezoelectric Ceramics for Actuator Applications. *Actuators.* **2017**, *6*, 24.

(48) Tan, X.; Ma, C.; Webber, K. The Antiferroelectric-Ferroelectric Phase Transition in Lead Containing and Lead-Free Perovskite Ceramics, *J. Am. Ceram. Soc.* **2011,** *94 (12),* 4091-4107.

(49) Li, L.; Zhu, M.; Wei, Q.; Zheng, M.; Hou, Y.; Hao, J. Ferroelectric P4mm to Relaxor P4bm Transition and Temperature-Insensitive Large Strains in $Bi(Mg_{0.5}Ti_{0.5})O_3$-Modified Tetragonal 0.875$Bi_{0.5}Na_{0.5}TiO_3$-0.125$BaTiO_3$ lead-Free Ferroelectric Ceramics. *J. Eur. Ceram. Soc.* **2018**, *38* (4), 1381–1388.

(50) Zhou, C.; Yuan, C.; Chen, G. Ferroelectric-Quasiferroelectric-Ergodic Relaxor Transition and Ceramics. *J. Am. Ceram. Soc.* **2018**, *64*, 1554–1565.

(51) Chen, D.; Ayrikyan, A.; Webber, K. G.; Kamlah, M. Time-Dependent Electromechanical Response of 0.93$(Na_{1/2}Bi_{1/2})TiO_3$-0.07$BaTiO_3$ Lead- Free Piezoceramic under Constant Electric Field. **2017**, *93*, 0–7.

(52) Tuttle, B. A.; Payne, D. A. The Effects of Microstructure on the Electrocaloric Properties of $Pb(Zr,Sn,Ti)O_3$ Ceramics. *Ferroelectrics.* **1981**, *37*, 603-606.

(53) Zheng, X.; Zheng, G.; Lin, Z. Xiu-Cheng Zheng & Guang-Ping Zheng & Zheng Lin & Zhi-Yuan Jiang. **2012**, 20–26.

(54) Chukka, R.; Cheah, J. W.; Chen, Z.; Yang, P.; Shannigrahi, S.; Wang, J.; Chen, L.; Chukka, R.; Cheah, J. W.; Chen, Z.; et al. Enhanced Cooling Capacities of

Ferroelectric Materials at Morphotropic Phase Boundaries. **2016**, *242902* (2011), 1–4.

(55) Dai, Y.-J.; Zhang, X.-W.; Chen, K.-P. Morphotropic Phase Boundary and Electrical Properties of $K_{1-x}Na_xNbO_3$ Lead-Free Ceramics. *Appl. Phys. Lett.* **2009**, *94* (4), 42905.

(56) Ogihara, H.; Randall, C. A.; Trolier-McKinstry, S. Weakly Coupled Relaxor Behavior of $BaTiO_3$-$BiScO_3$ Ceramics. *J. Am. Ceram. Soc.* **2009**, *92* (1), 110–118.

(57) Xiong, B.; Hao, H.; Zhang, S.; Liu, H.; Cao, M. Structure, Dielectric Properties and Temperature Stability of $BaTiO_3$-$Bi(Mg_{1/2}Ti_{1/2})O_3$ perovskite Solid Solutions. *J. Am. Ceram. Soc.* **2011**, *94* (10), 3412–3417.

(58) Kim, C.; Park, K.; Yoon, Y.; Sinn, D.; Kim, Y.; Hur, K. Effects of Milling Condition on the Formation of Core–Shell Structure in $BaTiO_3$ Grains. **2008**, *28*, 2589–2596.

(59) Liu, X.; Cheng, S.; Randall, C. A. The Core-Shell Structure in Ultrafine X7R Dielectric Ceramics. **1998**, *32*, 312–315.

(60) Stetefeld, J.; McKenna, S. A.; Patel, T. R. Dynamic Light Scattering: A Practical Guide and Applications in Biomedical Sciences. *Biophys. Rev.* **2016**, *8* (4), 409–427.

(61) Li, Y.; Barron, A. R. Dynamic Light Scattering. *Sci. Technol.* **2004**, *49* , 1676–1680.

(62) Smart, L. E.; Moore, E. A. Solid State Chemistry. 3rd ed. pp. 91-147.

(63) Degen, T.; Sadki, M.; Bron, E.; König, U.; Nénert, G. The HighScore Suite. **2014**, *29*, 13–18.

(64) Lewis, D. B. Scanning Electron Microscopy and X-Ray Microanalysis. **2017**, *2967*, 2–7.

(65) Analyzer, T. F. aixPlorer Software. pp 14–20.

(66) Ta, U.; Carle, V.; Scha, U.; Hoffmann, M. J. Preparation and Microstructural Analysis of High-Performance Ceramics. **2004**, *9*. pp 1057-1066.

(67) Chinn, R. E. Ceramography. pp. 45-53.

(68) Technologies, K. User's Guide Keysight E4980A/AL Precision LCR Meter. pp 187-189.

(69) Zhang, S. T.; Kounga, A. B.; Aulbach, E.; Ehrenberg, H.; Rödel, J. Giant Strain in Lead-Free Piezoceramics $Bi_{0.5}Na_{0.5}TiO_3$-$BaTiO_3$-$K_{0.5}Na_{0.5}NbO_3$ System. *Appl. Phys. Lett.* **2007**, *91* (11).

(70) Iqbal, Y.; Jamal, A.; Ullah, R.; Khan, M. N.; Ubic, R. Effect of Fluxing Additive on Sintering Temperature, Microstructure and Properties of $BaTiO_3$. *Bull. Mater. Sci. Indian Acad. Sci.* **2012**, *35* (3), 387–394.

(71) Du, H.; Liu, D.; Tang, F.; Zhu, D.; Zhou, W.; Qu, S. Microstructure, Piezoelectric, and Ferroelectric Properties of Bi_2O_3-Added $(K_{0.5}Na_{0.5})NbO_3$ Lead-Free Ceramics. *J. Am. Ceram. Soc.* **2007**, *90* (9), 2824–2829.

(72) Naceur, H.; Megriche, A.; El Maaoui, M. Effect of Sintering Temperature on Microstructure and Electrical Properties of $Sr_{1-x}(Na_{0.5}Bi_{0.5})_xBi_2Nb_2O_9$ Solid Solutions. *J. Adv. Ceram.* **2014**, *3* (1), 17–30.

(73) Liu, H.; Li, Q.; Ma, J.; Chu, X. Effects of Bi^{3+} content and Grain Size on Electrical Properties of $SrBi_2Ta_2O_9$ ceramic. *Mater. Lett.* **2012**, *76*, 21–24.

(74) Jin, L.; Li, F.; Zhang, S. Decoding the Fingerprint of Ferroelectric Loops: Comprehension of the Material Properties and Structures. *J. Am. Ceram. Soc.* **2014**, *97* (1), 1–27.

(75) Sanlialp, M.; Shvartsman, V. V.; Acosta, M.; Lupascu, D. C. Electrocaloric Effect in $Ba(Zr,Ti)O_3$–$(Ba,Ca)TiO_3$ Ceramics Measured Directly. *J. Am. Ceram. Soc.* **2016**, *99* (12), 4022–4030.

(76) Li, T.; Liu, X.; Shi, S.; Yin, Y.; Li, H.; Wang, Q.; Zhang, Y.; Bian, J.; Rajput, S. S.; Long, C.; et al. Large Electrocaloric Efficiency over a Broad Temperature Span in Lead-Free $BaTiO_3$-Based Ceramics near Room Temperature. *Appl. Phys. Lett.* **2017**, *111* (20).

(77) Liu, Y.; Scott, J. F.; Dkhil, B. Direct and Indirect Measurements on Electrocaloric Effect: Recent Developments and Perspectives. *Appl. Phys. Rev.* **2016**, *3* (3).

(78) Kaddoussi, H.; Lahmar, A.; Khemakham, H. A. Room temperature electro-caloric effect in lead-free $Ba(Zr_{0.1}Ti_{0.9})_{1-x}Sn_xO_3$ (x=0, x=0.075) ceramics. *Sol. State Commun.* **2015**, *201*, 64-67.

(79) Morimoto, K.; Sawai, S.; Hisano, K.; Yamamoto, T. Simultaneous Measurement of Specific Heat, Thermal Conductivity, and Thermal Diffusivity of Modified Barium Titanate Ceramics. *Thermochim. Acta* **2006**, *442* (1–2), 14–17.

(80) Liu, X. Q.; Chen, T. T.; Fu, M. Sen; Wu, Y. J.; Chen, X. M. Electrocaloric Effects in Spark Plasma Sintered $Ba_{0.7}Sr_{0.3}TiO_3$-Based Ceramics: Effects of Domain Sizes and Phase Constitution. *Ceram. Int.* **2014**, *40*, 11269–11276.

(81) Randall, C. A.; Wang, S. F.; Laubscher, D.; Dougherty, J. P.; Huebner, W. Structure Property Relationships in Core-Shell $BaTiO_3$—LiF Ceramics. *J. Mater. Res.* **1993**, *8* (4), 871–879.

(82) Beuerlein, M. A.; Kumar, N.; Usher, T.-M.; Brown-Shaklee, H. J.; Raengthon, N.; Reaney, I. M.; Cann, D. P.; Jones, J. L.; Brennecka, G. L. Current

Understanding of Structure-Processing-Property Relationships in $BaTiO_3$ - Bi(*M*)O_3 Dielectrics. *J. Am. Ceram. Soc.* **2016**, *99* (9), 2849–2870.

(83) Ramesh, G.; Ramachandra Rao, M. S.; Sivasubramanian, V.; Subramanian, V. Electrocaloric Effect in (1-x)PIN-xPT Relaxor Ferroelectrics. *J. Alloys Compd.* **2016**, *663*, 444–448.

(84) Cullity, B. D.; Cohen, M. Elements of Diffraction. 2nd ed. **1978**, pp 81-92 .

(85) Anton, E. M.; Jo, W.; Damjanovic, D.; Rdel, J. Determination of Depolarization Temperature of $(Bi_{1/2}Na_{1/2})TiO_3$-Based Lead-Free Piezoceramics. *J. Appl. Phys.* **2011**, *110* (9).

(86) Wang, C. J.; Wu, Y. A.; Jacobs, R. M. J.; Warner, J. H.; Williams, G. R.; O'Hare, D. Reverse Micelle Synthesis of Co-Al LDHs: Control of Particle Size and Magnetic Properties. *Chem. Mater.* **2011**, *23* (2), 171–180.

(87) Hiruma, Y.; Yoshii, K.; Nagata, H.; Takenaka, T. Phase Transition Temperature and Electrical Properties of $(Bi_{1/2}Na_{1/2})TiO_3$-$(Bi_{1/2}A_{1/2})TiO_3$ (A=Li and K) Lead-Free Ferroelectric Ceramics. *J. Appl. Phys.* **2008**, *103* (8).

(88) Bai, W.; Shen, B.; Zhai, J.; Liu, F.; Li, P.; Liu, B.; Zhang, Y. Phase Evolution and Correlation between Tolerance Factor and Electromechanical Properties in BNT-Based Ternary Perovskite Compounds with Calculated End-Member $Bi(Me_{0.5}Ti_{0.5})O_3$ (Me = Zn, Mg, Ni, Co). *Dalt. Trans.* **2016**, *45* (36), 14141–14153.

(89) Guo, Y.; Gu, M.; Luo, H.; Liu, Y.; Withers, R. L. Composition-Induced Antiferroelectric Phase and Giant Strain in Lead-Free $(Na_y,Bi_z)Ti_{1-x}O_{3(1-x)}$-$xBaTiO_3$ Ceramics. *Phys. Rev. B - Condens. Matter Mater. Phys.* **2011**, *83* (5), 1–7.

(90) Gao, F.; Dong, X.; Mao, C.; Liu, W.; Zhang, H.; Yang, L.; Cao, F.; Wang, G. Energy-Storage Properties of $0.89Bi_{0.5}Na_{0.5}TiO_3$-$0.06BaTiO_3$-$0.05K_{0.5}Na_{0.5}NbO_3$ Lead-Free Anti-Ferroelectric Ceramics. *J. Am. Ceram. Soc.* **2011**, *94* (12), 4382–4386.

(91) Zhao, W.; Zuo, R.; Zheng, D.; Li, L. Dielectric Relaxor Evolution and Frequency-Insensitive Giant Strains in $(Bi_{0.5}Na_{0.5})TiO_3$-Modified $Bi(Mg_{0.5}Ti_{0.5})O_3$-$PbTiO_3$ ferroelectric Ceramics. *J. Am. Ceram. Soc.* **2014**, *97* (6), 1855–1860.

(92) Ni, F.; Luo, L.; Li, W.; Chen, H. A-Site Vacancy-Induced Giant Strain and the Electrical Properties in Non-Stoichiometric Ceramics $Bi_{0.5+x}(Na_{1-y}K_y)_{0.5-3x}TiO_3$. *J. Phys. D. Appl. Phys.* **2012**, *45* (41).

(93) Pu, Y.; Yao, M.; Zhang, L.; Jing, P. High Energy Storage Density of $0.55Bi_{0.5}Na_{0.5}TiO_3$-$0.45Ba_{0.85}Ca_{0.15}Ti_{0.9}$−$xZr_{0.1}Sn_xO_3$ ceramics. *J. Alloys Compd.* **2016**, *687*, 689–695.

(94) Aguilar, B.; Navarro, O.; Carvajal, E.; Avignon, M. Effect of Mo / W Disorder on the Curie Temperature of $Sr_2FeMo_xW_{1-x}O_6$ Double Perovskite. *Rev. Mex. Fis.* **2007**, *53* (7), 146–149.

(95) Charles Kittel. Introduction to Solid State Physics. 8th ed. **2010**, pp 1-46.

(96) Gao, L.; Guo, H.; Zhang, S.; Randall, C. A. Stabilized Antiferroelectricity in $xBiScO_3$-(1-x)$NaNbO_3$ lead-Free Ceramics with Established Double Hysteresis Loops. *Appl. Phys. Lett.* **2018**, *112* (9).

(97) Hiruma, Y.; Yoshii, K.; Nagata, H.; Takenaka, T. Phase Transition Temperature and Electrical Properties of $(Bi_{1/2}Na_{1/2})TiO_3$-$(Bi_{1/2}A_{1/2})TiO_3$ (A=Li and K) Lead-Free Ferroelectric Ceramics. *J. Appl. Phys.* **2008**, *103* (8).

(98) Goian, V.; Kamba, S.; Greicius, S.; Nuzhnyy, D.; Karimi, S.; Reaney, I. M. Terahertz and Infrared Studies of Antiferroelectric Phase Transition in Multiferroic $Bi_{0.85}Nd_{0.15}FeO_3$. *J. Appl. Phys.* **2011**, *110* (7), 0–7.

(99) Karimi, S.; Reaney, I. M.; Levin, I.; Sterianou, I. Nd-Doped $BiFeO_3$ ceramics with Antipolar Order. *Appl. Phys. Lett.* **2009**, *94* (11), 1–4.

(100) Gao, L.; Guo, H.; Zhang, S.; Randall, C. A. A Perovskite Lead-Free Antiferroelectric $xCaHfO_3$-(1-x)$NaNbO_3$ with Induced Double Hysteresis Loops at Room Temperature. *J. Appl. Phys.* **2016**, *120* (20).

(101) Zhang, S. T.; Kounga, A. B.; Aulbach, E.; Granzow, T.; Jo, W.; Kleebe, H. J.; Rödel, J. Lead-Free Piezoceramics with Giant Strain in the System $Bi_{0.5}Na_{0.5}TiO_3$-$BaTiO_3$-$K_{0.5}Na_{0.5}NbO_3$. I. Structure and Room Temperature Properties. *J. Appl. Phys.* **2008**, *103* (3), 3–10.

(102) Jo, W.; Granzow, T.; Aulbach, E.; Rödel, J.; Damjanovic, D. Origin of the Large Strain Response in $(K_{0.5}Na_{0.5})NbO_3$-Modified $(Bi_{0.5}Na_{0.5})TiO_3$-$BaTiO_3$ lead-Free Piezoceramics. *J. Appl. Phys.* **2009**, *105* (9).

(103) Manotham, S.; Butnoi, P.; Jaita, P.; Kumar, N.; Chokethawai, K.; Rujijanagul, G.; Cann, D. P. Large Electric Field-Induced Strain and Large Improvement in Energy Density of Bismuth Sodium Potassium Titanate-Based Piezoelectric Ceramics. *J. Alloys Compd.* **2018**, *739*, 457–467.

(104) Liu, X. Q.; Chen, T. T.; Wu, Y. J.; Chen, X. M. Enhanced Electrocaloric Effects in Spark Plasma-Sintered $Ba_{0.65}Sr_{0.35}TiO_3$-Based Ceramics at Room Temperature. *J. Am. Ceram. Soc.* **2013**, *96* (4), 1021–1023.

(105) Bai, Y.; Zheng, G. P.; Shi, S. Q. Abnormal Electrocaloric Effect of $Na_{0.5}Bi_{0.5}TiO_3$-$BaTiO_3$ lead-Free Ferroelectric Ceramics above Room Temperature. *Mater. Res. Bull.* **2011**, *46* (11), 1866–1869.

(106) Zhou, C.; Feteira A. Observation of Multiple Dielectric Relaxations in $BaTiO_3$-$Bi(Li_{1/3}Ti_{2/3})O_3$ ceramics. *Appl. Phys. A* **2017**, *712 (123)*.